

Université  
de Toulouse

# THÈSE

En vue de l'obtention du

## DOCTORAT DE L'UNIVERSITÉ DE TOULOUSE

**Délivré par :**

Institut National Polytechnique de Toulouse (Toulouse INP)

**Discipline ou spécialité :**

Signal, Image, Acoustique et Optimisation

---

**Présentée et soutenue par :**

M. SIMONE URBANO

le jeudi 18 avril 2019

**Titre :**

Detection and Diagnostic of Freeplay Induced Limit Cycle Oscillation in the  
Flight Control System of a Civil Aircraft

---

**Ecole doctorale :**

Mathématiques, Informatique, Télécommunications de Toulouse (MITT)

**Unité de recherche :**

Institut de Recherche en Informatique de Toulouse (I.R.I.T.)

**Directeur(s) de Thèse :**

M. JEAN-YVES TOURNERET

M. ERIC CHAUMETTE

**Rapporteurs :**

Mme NADINE MARTIN, CNRS SAINT MARTIN D'HERES

M. PHILIPPE FORSTER, UNIVERSITE PARIS 10

**Membre(s) du jury :**

M. JEAN-PHILIPPE OVARLEZ, ONERA - CENTRE DE PALAISEAU, Président

M. ERIC CHAUMETTE, ISAE-SUPAERO, Membre

M. JEAN-YVES TOURNERET, INP TOULOUSE, Membre

M. MARCO LOPS, UNIV. DEGLI STUDI DI NAPOLI FEDERICO II, Membre

Mme CORINNE MAILHES, INP TOULOUSE, Membre

M. PHILIPPE GOUPIL, AIRBUS FRANCE, Membre



*Alla mia famiglia*

“Non est ad astra mollis e terris via”

— Lucius Annaeus Seneca, *Hercules furens*.

# Acknowledgements

Numerous people have contributed directly and/or indirectly to this study and it is not possible to make an exhaustive list here, but I will try to recall some of the main contributors. First of all, I would like to thank my Airbus adviser Philippe Goupil and my academic advisers Eric Chaumette and Jean-Yves Tournet for their continuous support, motivation and strong involvement in this research project. It is never an easy task to look for a compromise between industrial needs and a valuable academic contribution, but an attempt has been made and thanks to my my advisers I have grown a lot during the last few years. I am deeply indebted to all of you. I would like to extend my sincere thanks to the rest of my thesis committee for their precious comments and suggestions that have been taken into account to improve the overall quality of the manuscript. This PhD thesis would not have been possible without the welcome of Eric Albert, chief of the EYCIF team, and all my close colleagues from Airbus. In particular, I would like to thank all the colleagues that have contributed directly to this project. It was a multidisciplinary project and colleagues/experts from different domains have given their contribution: flight controls, flight tests, data analysis, modeling and simulation, loads and aeroelasticity, actuators, customer support, ... Interns and subcontractors have also supported this project. I am really grateful to all of you, none of this would have been possible without your help. I would also like to extend my gratitude to all the colleagues/friends at the Airbus site with whom I spent a lot of pleasant time and that were always a source of good mood: Valentin, Luna, Francesco R., Quentin, Xavi, Guillaume, ... Thanks should also go to the Airbus PhD community for their enthusiasm and support during my PhD. This PhD thesis would not have been possible without the welcome of Corinne Mailhes, director of TéSA, and all the PhD students/colleagues from TéSA laboratory. A special thanks goes to Romain & Charles-Ugo, Selma, Barbara, Quentin, Lorenzo, Julien, Sylvain, Adrien, Antoine, Raoul, Philippe, Serge, Bernard, Patrice, Jacques, Isabelle, Fabio, Karine, ... I would like to sincerely thank all of you for the time spent together during these three unforgettable years. I also wish to thank the "Italian gang" with whom I started and shared the french adventure: Francesco S., Marco, Geraldina, Emanuele, Chiara, Valerio, Francesca, Aurora, Stefano, ... I could go on, the list is a long one. Finally, I would also like to thank my girlfriend Agathe, for supporting me spiritually throughout writing this thesis and I must say "*Grazie*" to the ones that are far away, but that are always in my mind. In particular, I am extremely grateful to my friends/brothers of "il Quartiere" and to my family: Marilena, Antonio, Sonia, Angelo, Assunta, Franco, ... You were always by my side all along and I will never forget it. The luck of a man is always related to three things: freedom, love and trust and there are no doubts that my family made me a lucky man.

“I blame all of you. Writing this book has been an exercise in sustained suffering. The casual reader may, perhaps, exempt herself from excessive guilt, but for those of you who have played the larger role in prolonging my agonies with your encouragement and support, well...you know who you are, and you owe me.”

— Brendan Pietsch, *Dispensational Modernism*.

# Abstract / Résumé

## Abstract

This research study is the result of a 3 years CIFRE PhD thesis between the Airbus design office (Aircraft Control domain) and TésA laboratory in Toulouse. The main goal is to propose, develop and validate a software solution for the detection and diagnosis of a specific type of elevator and rudder vibration, called limit cycle oscillation (LCO), based on existing signals available in flight control computers on board in-series aircraft. LCO is a generic mathematical term defining an initial condition-independent periodic mode occurring in non-conservative nonlinear systems. This study focuses on the LCO phenomenon induced by mechanical freeplays in the control surface of a civil aircraft. The LCO consequences are local structural load augmentation, flight handling qualities deterioration, actuator operational life reduction, cockpit and cabin comfort deterioration and maintenance cost augmentation. The state-of-the-art for freeplay induced LCO detection and diagnosis is based on the pilot sensitivity to vibration and to periodic freeplay check on the control surfaces.

This study is thought to propose a data-driven solution to help LCO and freeplay diagnosis. The goal is to improve even more aircraft availability and reduce the maintenance costs by providing to the airlines a condition monitoring signal for LCO and freeplays. For this reason, two algorithmic solutions for vibration and freeplay diagnosis are investigated in this PhD thesis. A real time detector for LCO diagnosis is first proposed based on the theory of the generalized likelihood ratio test (GLRT). Some variants and simplifications are also proposed to be compliant with the industrial constraints. In a second part of this work, a mechanical freeplay detector is introduced based on the theory of Wiener model identification. Parametric (maximum likelihood estimator) and nonparametric (kernel regression) approaches are investigated, as well as some variants to well-known non-parametric methods. In particular, the problem of hysteresis cycle estimation (as the output nonlinearity of a Wiener model) is tackled. Moreover, the constrained and unconstrained problems are studied.

A theoretical, numerical (simulator) and experimental (flight data and laboratory) analysis is carried out to investigate the performance of the proposed detectors and to identify limitations and industrial feasibility. The obtained numerical and experimental results confirm that the proposed GLR test (and its variants/simplifications) is a very appealing method for LCO diagnostic in terms of performance, robustness and computational cost. On the other hand, the proposed freeplay diagnostic algorithm is able to detect relatively large freeplay levels, but it does not provide consistent results for relatively small freeplay levels. Moreover, specific input types are needed to guarantee repetitive and consistent results. Further studies should be carried out in order to compare the GLRT results with a Bayesian approach and to investigate more deeply the possibilities and limitations of the proposed parametric method for Wiener model identification.

---

## Résumé

Cette étude est le résultat d'une thèse CIFRE de trois ans entre le bureau d'étude d'Airbus (domaine du contrôle de l'avion) et le laboratoire TESA à Toulouse. L'objectif principal est de proposer, développer et valider une solution logicielle pour la détection et le diagnostic d'un type spécifique de vibrations des gouvernes de profondeur et direction, appelée oscillation en cycle limite (limit cycle oscillation ou LCO en anglais), basée sur les signaux existants dans les avions civils. LCO est un terme mathématique générique définissant un mode périodique indépendant de conditions initiales et se produisant dans des systèmes non linéaires non conservatifs. Dans cette étude, nous nous intéressons au phénomène de LCO induit par les jeux mécaniques dans les gouvernes d'un avion civil. Les conséquences du LCO sont l'augmentation locale de la charge structurelle, la dégradation des qualités de vol, la réduction de la durée de vie de l'actionneur, la dégradation du confort du poste de pilotage et de la cabine, ainsi que l'augmentation des coûts de maintenance. L'état de l'art en matière de détection et de diagnostic du LCO induit par le jeu mécanique est basé sur la sensibilité du pilote aux vibrations et sur le contrôle périodique du jeu sur les gouvernes. Cette étude propose une solution basée sur les données (issues de la boucle d'asservissement des actionneurs qui agissent sur les gouvernes) pour aider au diagnostic du LCO et à l'isolement du jeu mécanique. L'objectif est d'améliorer encore plus la disponibilité des avions et de réduire les coûts de maintenance en fournissant aux compagnies aériennes un signal de contrôle pour le LCO et les jeux mécaniques. Pour cette raison, deux solutions algorithmiques pour le diagnostic des vibrations et des jeux ont été proposées. Un détecteur en temps réel pour la détection du LCO est tout d'abord proposé basé sur la théorie du rapport de vraisemblance généralisé (generalized likelihood ratio test ou GLRT en anglais). Certaines variantes et simplifications sont également proposées pour satisfaire les contraintes industrielles. Un détecteur de jeu mécanique est introduit basé sur l'identification d'un modèle de Wiener. Des approches paramétrique (estimateur de maximum de vraisemblance) et non paramétrique (régression par noyau) sont explorées, ainsi que certaines variantes des méthodes non paramétriques. En particulier, le problème de l'estimation d'un cycle d'hystérésis (choisi comme la non-linéarité de sortie d'un modèle de Wiener) est abordé. Ainsi, les problèmes avec et sans contraintes sont étudiés. Une analyse théorique, numérique (sur simulateur) et expérimentale (données de vol et laboratoire) est réalisée pour étudier les performances des détecteurs proposés et pour identifier les limitations et la faisabilité industrielle. Les résultats numériques et expérimentaux obtenus confirment que le GLRT proposé (et ses variantes / simplifications) est une méthode très efficace pour le diagnostic du LCO en termes de performance, robustesse et coût calculatoire. D'autre part, l'algorithme de diagnostic des jeux mécaniques est capable de détecter des niveaux de jeu relativement importants, mais il ne fournit pas de résultats cohérents pour des niveaux de jeu relativement faibles. En outre, des types d'entrée spécifiques sont nécessaires pour garantir des résultats répétitifs et cohérents. Des études complémentaires pourraient être menées afin de comparer les résultats de GLRT avec une approche Bayésienne et pour approfondir les possibilités et les limites de la méthode paramétrique proposée pour l'identification du modèle de Wiener.

# Contents

<b>1. Introduction</b>	<b>1</b>
1.1. Context	1
1.2. Goals	2
1.3. Contribution	2
1.4. Manuscript organization	2
1.5. Publications	3
<b>2. Free play induced Limit Cycle Oscillation (LCO)</b>	<b>5</b>
2.1. Introduction	5
2.2. Electric Flight Control System	5
2.3. Limit Cycle Oscillation (LCO)	13
2.4. State-of-the-art	21
2.5. LCO and freeplay condition monitoring	25
2.6. Challenges	27
2.7. Conclusions	28
<b>3. LCO detection via GLR tests</b>	<b>29</b>
3.1. Introduction	29
3.2. Binary Hypothesis testing	29
3.3. LCO detection	31
3.4. Matched filter and GLRT special cases	32
3.5. Deterministic signal detection in interference	37
3.6. Approximate GLRT	40
3.7. Detection performance	42
3.8. Sinusoidal signal detection in deterministic interference	44
3.8.1. Maximum Likelihood Estimators and Test Statistic	45
3.8.2. Theoretical performance	47
3.8.3. Synthetic data	48
3.9. Conclusions and perspectives	50
<b>4. Freeplay estimation via Wiener model identification</b>	<b>53</b>
4.1. Introduction	53
4.2. Introduction to Kernel Regression	54
4.2.1. Kernel density estimation	54
4.2.2. Kernel regression	54
4.2.3. Bandwidth selection	55
4.3. Non-parametric Wiener system identification	57
4.3.1. Nadaraya-Watson kernel estimator	57
4.3.2. Wiener model identification for hysteresis non linearity	64
4.3.3. Constrained Kernel Regression	69
4.4. Parametric estimation	75
4.4.1. Deterministic Cramér-Rao bounds	77
4.4.2. A lower bound on the global estimation error	78
4.4.3. Maximum Likelihood estimator	79
4.5. Conclusions and Perspectives	83
<b>5. Industrial Validation</b>	<b>85</b>
5.1. Introduction	85
5.2. LCO diagnostic	87
5.2.1. Example of LCO detection	88
5.2.2. Simulation Results	89
5.2.3. Experimental results	94

5.3. Freeplay diagnostic . . . . .	96
5.3.1. Example of freeplay detection . . . . .	97
5.3.2. Simulation results . . . . .	98
5.3.3. Experimental results . . . . .	100
<b>6. Conclusions</b>	<b>103</b>
<b>A. Annexes</b>	<b>107</b>
A.1. Asymptotic approximation for the sufficient statistic . . . . .	107
A.2. Characteristic functions and PDF approximation . . . . .	108
A.3. Projection matrices . . . . .	109
A.4. GLRT by Alternating Projection (AP) . . . . .	110
A.5. Goertzel algorithm . . . . .	113
<b>Bibliography</b>	<b>114</b>

# List of Figures

1.1. Main sources of vibration on A320 Family aircraft [SAS17]. . . . .	1
2.1. Example of control surface section with actuator. . . . .	6
2.2. Airbus Electrical Flight Control System (EFCS). . . . .	7
2.3. Airbus control surface servo loop. . . . .	7
2.4. Historical evolution of the Flight Control System. . . . .	8
2.5. A380 EFCS architecture. . . . .	8
2.6. Hydraulic actuator, Electro-Hydraulic Actuator and Electrical Back-up Hydraulic Actuator. . . . .	9
2.7. Electrification of the FCS on Airbus aircraft. . . . .	10
2.8. Active/Stand-by reconfiguration and example of PRIM/SEC computers. . . . .	11
2.9. Flight control law reconfiguration and flight domain protections [Gou11]. . . . .	12
2.10. Airbus COM/MON architecture. . . . .	12
2.11. Typical section of airfoil with unbalanced control surfaces. . . . .	13
2.12. Example of C/S rotation mode and first bending mode [PB14]. . . . .	14
2.13. Equivalent C/S rotational stiffness : new/aged aircraft [Loz08]. . . . .	15
2.14. Sub-critical and super-critical LCO [Dow15]. . . . .	15
2.15. Initial condition response of a wing section with control surface (see (2.1)). A stable convergent response can be observed. . . . .	16
2.16. Initial condition response of a wing section with control surface and freeplay. The same mathematical model (2.1) of Figure 2.15 is considered, but a symmetric dead zone on the rotational stiffness is considered to simulate the mechanical freeplay. An LCO-type behavior can be observed due to the freeplay. . . . .	16
2.17. Initial condition response of a wing section with control surface and freeplay. The same mathematical model (2.1) and the same free play level of Figure 2.16 is considered; but here the center of gravity of the control surface is five time closer to the hinge line $x_g = x_g/5$ . A stable convergent response can be observed. . . . .	17
2.18. Frequency and damping (as a function of the wind speed) for a wing section with control surface (3 degrees of freedom : flap, twist, rotation) [Wri+03]. . . . .	17
2.19. Frequency and damping (as a function of the wind speed) for a wing section with control surface and actuator [Wri+03]. . . . .	18
2.20. Initial condition response at 39 m/s for the model of Figure 2.19. A stable convergent response can be observed. . . . .	18
2.21. Initial condition response at 39 m/s for the model of Figure 2.19 where a symmetric dead zone has been considered on the actuator torque to simulate the freeplay. An LCO-type behavior can be observed. . . . .	19
2.22. Initial condition response at 39 m/s for the model of Figure 2.20 where an higher actuator stiffness has been considered (area of pressure stabilization piston is 3 times bigger). A stable convergent response can be observed. . . . .	19
2.23. LCO trigger zone, comparison between C/S available load and minimum load to preclude the LCO. . . . .	20
2.24. Example of balanced control surfaces (ATR72 and Messerschmitt Bf110). . . . .	21
2.25. “Vibration Reporting Sheet” (Airbus) and “Flight Deck Vibration Event Log” (Boeing). . . . .	23
2.26. Effect of the residual play on long term. . . . .	23
2.27. Freeplay check operation. . . . .	24
2.28. CAM device on the A380 upper rudder. . . . .	24
2.29. Example of freeplay estimation via load/displacement plot [Lub08]. . . . .	26
2.30. Predictive maintenance. . . . .	27
3.1. Regions of operations of a nonlinear estimation problem [VB07]. . . . .	31
3.2. Model of the detection problem. . . . .	32
3.3. Matched filter for the case of a known signal $y^0 = \lambda x(n - p)$ . . . . .	33
3.4. GLRT for an unknown amplitude A. . . . .	34
3.5. GLRT for A, $\phi$ unknown: the quadrature matched filter. . . . .	34
3.6. GLRT for A, $\phi$ unknown: Periodogram. . . . .	35
3.7. GLRT for A, $\phi$ , f unknown: peaks of the periodogram. . . . .	35

3.8. Detector for $\lambda$ and $p$ unknown: estimation of $\lambda$ and $p$ + matched filter (between $s$ and the residuals $y - y^0$ ) . . . . .	36
3.9. Example of detector for $\lambda$ , $p$ , $A$ and $\phi$ unknown: estimation of $\lambda$ and $p$ + periodogram of the residuals $y - y^0$ . . . . .	37
3.10. Comparison of the empirical distributions of the GLRT ( $T_{GLRT}$ ) and the approximate GLRT ( $T_a$ ) under the hypotheses $\mathcal{H}_0$ and $\mathcal{H}_1$ for the test case described in Section 3.8. . . . .	42
3.11. Empirical ( $N_{MC} = 10^4$ realizations, $\Delta p = 1e^{-5}s$ , $\Delta f = 1e^{-4}Hz$ ) and theoretical $P_{FA}$ as a function of the threshold $\gamma$ . $SNR_1 = SNR_2 = 20dB$ . . . . .	49
3.12. Empirical ( $N_{MC} = 10^5$ realizations, $\Delta p = 1e^{-5}s$ , $\Delta f = 1e^{-3}Hz$ ) and theoretical ROC curves. $SNR_1 = SNR_2 = 13dB$ . . . . .	49
4.1. Comparison of the histogram and kernel density estimate on the same data [Wik19a]. . . . .	54
4.2. Wiener Model. . . . .	57
4.3. Partition of the training set T. . . . .	58
4.4. Example of input/output data of a Wiener model. $SNR = 20dB$ . . . . .	60
4.5. Histograms of the synthetic data of Fig. 4.4. . . . .	60
4.6. Estimated Linear and Nonlinear subsystems from the synthetic data of Fig. 4.4. $h = h_S/4$ . . . . .	61
4.7. Different realizations of the estimator for the set in Fig. 4.4. $h = h_S/4$ . 50 identified models are superimposed in the figure (red) compared to the true system (blue). . . . .	61
4.8. Normalized Mean Square Error (NMSE) as a function of the bandwidth parameter $h$ for the set in Fig. 4.4. . . . .	62
4.9. Normalized Mean Square Error (NMSE) as a function of the filter order $p$ for the set in Fig. 4.4. $h = h_S$ . Actual order $p_{true} = 3$ . . . . .	63
4.10. Normalized Mean Square Error (NMSE) as a function of the number of samples N for the set in Fig. 4.4. $h = h_S/4$ . . . . .	63
4.11. Normalized Mean Square Error (NMSE) as a function of the Signal to Noise Ratio (SNR) for the set in Fig. 4.4. $h = h_S/4$ . . . . .	64
4.12. Hysteresis effect. . . . .	65
4.13. Example of Input/Output data that can be related via a Wiener model with hysteresis non linearity. $SNR = 40dB$ . . . . .	66
4.14. Histograms of the synthetic data of Fig. 4.13. . . . .	66
4.15. Estimated Linear and Nonlinear subsystems from the synthetic data of Fig. 4.13. $h = h_S/4$ . . . . .	67
4.16. Histograms of the actual and estimated outputs. . . . .	67
4.17. Different realizations of the estimator for the set in Fig. 4.13. $h = h_S/4$ . 50 identified models are superimposed in the figure (red) that can be compared to the true system (blue). . . . .	68
4.18. Normalized Mean Square Error (NMSE) as a function of the number of samples N for the set in Fig. 4.13. $h = h_S/4$ . . . . .	69
4.19. Normalized Mean Square Error (NMSE) as a function of the Signal to Noise Ratio (SNR) for the set in Fig. 4.13. $h = h_S/4$ . . . . .	69
4.20. Estimated linear and nonlinear subsystems from the synthetic data of Fig. 4.4 considering a constrained kernel estimator. PM1C (yellow) is the constrained version. . . . .	71
4.21. Example of constrained kernel estimator considering bounds on the first derivative of the nonlinear characteristic. PM1C (yellow) is the constrained version. . . . .	73
4.22. Example of constrained kernel estimator considering bounds on the shape and the first derivative of the nonlinear characteristic. PM1C (yellow) is the constrained version. . . . .	74
4.23. Example of constrained kernel estimator considering bounds on the first derivative of the nonlinear characteristic (Hysteresis type). PMH1C (red) is the constrained version. . . . .	75
4.24. Input signal $x$ (left) and non linearity $g(\cdot)$ (right) . . . . .	81
4.25. MSEs of the MLE (4.61) and of Pawlak's estimator (4.45) for $\lambda$ versus SNR, and the corresponding $\mathbf{CRB}(\lambda)$ (4.53). . . . .	81
4.26. MSE of the MLEs of $(\alpha, \beta)$ (4.60-4.61) versus SNR, and the corresponding $\mathbf{CRB}(\alpha, \beta)$ (4.53). . . . .	82
4.27. $MISE(\hat{g}(\cdot))$ (4.56) of the MLE (4.60-4.61) and of Pawlak's estimator (4.45) versus SNR, compared with the lower bound (4.57). . . . .	82
4.28. Estimated nonlinearity $\hat{g}(\cdot)$ obtained with the MLEs (4.60-4.61, in black) and Pawlak's estimators (4.45, in red) of $(\lambda, \alpha, \beta)$ , compared to the ground truth $g(\cdot)$ (in blue) at $SNR = 52dB$ . . . . .	83

5.1. Example of condition monitoring signal. . . . .	86
5.2. Application of the GLRT for the detection of an undesired oscillation affecting a control surface of a civil aircraft. Please note that for confidentiality reasons the oscillation amplitude is not shown. . . . .	88
5.3. Typical vertical flight path. . . . .	89
5.4. Example of identification for the vibration target level $A_2$ . . . . .	91
5.5. Aircraft descent under different operating conditions: altitude (up) and control surface hinge moment (down). The hinge moment values are hidden for confidentiality reasons. . . . .	92
5.6. Example of amplitude estimation (up) and duration estimation (down) for the simulated scenario in Fig. 5.5 and the target amplitude $A_2$ . For 3 levels of turbulence ( $T_1 = \text{low}, T_2 = \text{medium}, T_3 = \text{strong}$ ). . . . .	92
5.7. Mean amplitude estimation error (up) and mean duration estimation error (down) for the case in Figure 5.5 as a function of the target amplitude for a low level of turbulence. A $2\sigma$ error bar is also considered for each mean error. . . . .	93
5.8. Mean amplitude estimation error (up) and mean duration estimation error (down) for the case in Fig. 5.5 as a function of the turbulence level for the target amplitude $A_2$ . A $2\sigma$ error bar is also considered for each mean error. . . . .	93
5.9. GLR test for the detection of undesired oscillations affecting a C/S of an Airbus aircraft. The test statistic (in comparison to the threshold) is shown. Please note that for confidentiality reasons some data are not shown. . . . .	94
5.10. Schematic of the actuator test bench. . . . .	95
5.11. True and estimated oscillation amplitudes for different flight phases and freeplay levels. Two different observation windows are considered. The amplitudes are normalized for confidentiality reasons. . . . .	96
5.12. Application to 4 test sets representing 4 flights with increasing known levels of freeplay. The predictive index corresponds to the area of the estimated hysteresis. . . . .	97
5.13. Application to 4 test sets representing 4 flights with no freeplay. The predictive index corresponds to the area of the estimated hysteresis. . . . .	98
5.14. Airbus Simulink/Matlab model used to represent the actuator response and its interaction with the flight control computers and the control surface. . . . .	99
5.15. Area versus norm of the estimated nonlinearity for the simulated data [Car18]. . . . .	99
5.16. Area versus norm of the estimated nonlinearity for the real actuator test bench. Fixed tuning. . . . .	100
5.17. Area versus norm of the estimated nonlinearity for the real actuator test bench. Variable tuning. . . . .	101
6.1. NASA technology readiness levels (TRL). . . . .	105
A.1. Simulink implementation of Goertzel algorithm ( $ X(\omega) ^2$ ) for a given frequency. . . . .	114



# List of Tables

4.1. NMSE for 50 runs on the set in Fig. 4.4. . . . .	62
4.2. NMSE for 50 runs on the set in Fig. 4.13 . . . . .	68
5.1. LCO troubleshooting on a C/S as in Figure 2.8 (active/passive scheme). . . . .	86
5.2. Considered Operating Conditions. . . . .	90
6.1. Summary of Validation datasets. . . . .	104
6.2. Results summary. . . . .	105



# 1

## Introduction

### Contents

---

1.1. Context . . . . .	1
1.2. Goals . . . . .	2
1.3. Contribution . . . . .	2
1.4. Manuscript organization . . . . .	2
1.5. Publications . . . . .	3

---

### 1.1. Context

The main sources of airframe vibration on the Airbus A320 Family aircraft are shown in Fig. 1.1



Figure 1.1.: Main sources of vibration on A320 Family aircraft [SAS17].

One can observe that vertical and horizontal tail plane control surfaces (Elevator and Rudder) represent the major cause of airframe vibrations (72%). These vibrations may have multiple consequences on the aircraft life cycle from the design to operations. Indeed, spurious oscillations of the control surfaces (C/S) impact both the structural airframe design and the flight control system design. Undetected oscillations may lead to several problems including local structural load augmentation, flight handling qualities deterioration, actuator operational life reduction, cockpit and cabin comfort deterioration as well as maintenance cost augmentation. For

these reasons, the ability to detect and isolate unwanted oscillations beyond a given amplitude is an important feature for a **fault-tolerant, economically efficient and comfortable** aircraft architecture.

## 1.2. Goals

The main goal of this research study is to propose, develop and validate a software solution for the detection and diagnosis of a specific type of elevator and rudder vibration based on existing signals available in flight control computers on board in-series aircraft. In particular, the problem of freeplay induced Limit Cycle Oscillation (LCO) is tackled based on the signals already available in the actuator control loops that move the control surfaces. In the next chapter the context and challenges of the technical problem of LCO detection and diagnosis are clarified.

## 1.3. Contribution

This research study is the result of a 3 years **CIFRE** PhD thesis (from 21/03/16 to 20/03/2019) between the Airbus design office (Aircraft Control domain) and T SA laboratory in Toulouse. The main contributions of this study are related to the proposal of two algorithmic solutions for vibration detection and diagnosis and to the theoretical and numerical validation of their performance. In particular, a real time detector for LCO detection is proposed in Chapter 3 based on the theory of the Generalized Likelihood Ratio Test (GLRT) [Urb+18b]. A mechanical freeplay detector is introduced in Chapter 4 based on the theory of Wiener model identification [Urb+19]. A theoretical and empirical analysis of the performance of these two detectors is presented to justify their choice. It is important to observe that the industrial constraints associated with the technical problem of LCO detection and diagnosis are functions of the considered aircraft, control surface, airline, available signals, etc. In order to propose a valuable solution respecting as many constraints as possible, a family of detectors has been proposed based on the chosen general theory [Urb+18a; Urb+17b]. Chapters 3 and 4 detail the theoretical contribution of this research study, while Chapter 5 presents the numerical and experimental results.

## 1.4. Manuscript organization

The manuscript is organized as follows: Chapter 2 presents the context and the state of the art about LCO detection and diagnosis in the Flight Control System. The LCO problem is analyzed and illustrated with some examples and the state-of-the-practice is detailed. The technical solutions proposed in this study are put into context and justified. Chapter 3 investigates a real-time LCO detector based on the GLRT theory. The problem is modeled as a binary hypothesis testing problem and several detectors are proposed depending on the known and unknown parameters. A very general formulation is proposed and validated along with some variants and

simplifications. An important contribution of this chapter is to derive the asymptotic performance of the GLRT for LCO detection. Chapter 4 studies a freeplay detector based on non linear Wiener model identification. A well-known method for **nonparametric** Wiener model identification is adapted to our technical problem and some variants are proposed (hysteresis non linearity and multiple constraints). The proposed solution can also be interpreted as a parametric estimator and thus it is compared to the maximum likelihood estimator. The variance of the estimators is finally compared to some theoretical performance bounds. Chapter 5 presents the practical implementation and validation of the proposed solutions. The test results on simulated and experimental data are presented. Chapter 6 summarizes the results, emphasizes the author contribution and presents the conclusions and perspectives about this study.

## 1.5. Publications

### International conferences

- [Urb+17a] Simone Urbano et al. “A Data-Driven Approach For Actuator Servo Loop Failure Detection”. In: *Proc. 20th IFAC World Congress, IFAC-PapersOnLine*. Vol. 50. 1. Toulouse, France: Elsevier, 2017, pp. 13544–13549 (cit. on p. 25).
- [Urb+18a] Simone Urbano et al. “Aircraft Vibration Detection and Diagnosis for Predictive Maintenance using a GLR Test”. In: *Proc. IFAC Symp. on fault Detection, Supervision and Safety for Technical Processes (IFAC Safeprocess)*. Warsaw, Poland, Aug. 2018 (cit. on pp. 2, 87).
- [Urb+18b] Simone Urbano et al. “On the High-SNR Receiver Operating Characteristic of the GLRT for the Conditional Signal Model”. In: *Proc. IEEE Int. Conf. Acoust., Speech, and Signal Processing (ICASSP)*. Calgary, Canada, Apr. 2018 (cit. on pp. 2, 29).
- [Urb+19] Simone Urbano et al. “On nonparametric identification of Wiener system with deterministic inputs”. In: *Proc. IEEE Int. Conf. Acoust., Speech, and Signal Processing (ICASSP)*. Brighton, UK, May 2019 (cit. on pp. 2, 74).

### Patents

- [Urb+17b] Simone Urbano et al. *Procédé et dispositif de détection et de diagnostic de vibrations d’un aéronef liées à un phénomène d’usure de pièces mécaniques dans une gouverne*. Application No 1761214, submitted to the French Patent Office (INPI). 2017 (cit. on p. 2).



# 2

## Free play induced Limit Cycle Oscillation (LCO)

### Contents

---

<b>2.1. Introduction</b> . . . . .	<b>5</b>
<b>2.2. Electric Flight Control System</b> . . . . .	<b>5</b>
<b>2.3. Limit Cycle Oscillation (LCO)</b> . . . . .	<b>13</b>
<b>2.4. State-of-the-art</b> . . . . .	<b>21</b>
<b>2.5. LCO and freeplay condition monitoring</b> . . . . .	<b>25</b>
<b>2.6. Challenges</b> . . . . .	<b>27</b>
<b>2.7. Conclusions</b> . . . . .	<b>28</b>

---

### 2.1. Introduction

This chapter presents the industrial context and the state-of-the-art. The main goal is to introduce the reader to the problem of freeplay induced limit cycle oscillation in the flight control system of a civil aircraft. Indeed, as already mentioned in Chapter 1, this research study is intended to propose, develop and validate a software solution for the detection and diagnosis of LCO based on existing signals in the flight control system. Thus, in order to propose a reasonable solution, it is important to study more in details the LCO phenomenon and the flight control system. Section 2.2 presents the electrical flight control system with a particular attention to the fault tolerance requirements. In Section 2.3 the LCO problem is analyzed and illustrated with some examples. Section 2.4 introduces the state-of-the-practice to face the LCO problem. The technical solutions proposed in this study are put into context and justified. Section 2.6 discusses the main challenges for developing a condition monitoring algorithm in the EFCS. Conclusions about this Chapter are finally reported in Section 2.7.

### 2.2. Electric Flight Control System

The flight control system (FCS) consists of all the elements between the pilot inputs and the movable surfaces, including these two elements. This system is used to control the aircraft attitude and trajectory. The first

Electrical Flight Control System (EFCS) for a civil aircraft was designed by Aerospatiale and installed on the Concorde. It was an analog system with full-authority on all the control surfaces with a mechanical back-up system on the three axis. The first generation of digital EFCS appeared on Airbus aircraft with the A320 program and today, the EFCS is a standard for passenger airliners. The EFCS has many advantages compared to a mechanical system: less weight, less workload for the crew, more comfort for the passengers, more accurate control of the flight envelope.

The Flight Control System is composed of two main functional sets

- the primary controls: to manage speed, attitude, altitude and trajectory
- the secondary controls: to manage the lift of the aircraft

The primary controls are then composed of the following components

- the pilot inputs (sidestick, rudder pedals, ...)
- the transmission system (mechanical or electrical)
- the control surfaces and their actuators (Figure 2.1)
- the sensors (for the control feedback)

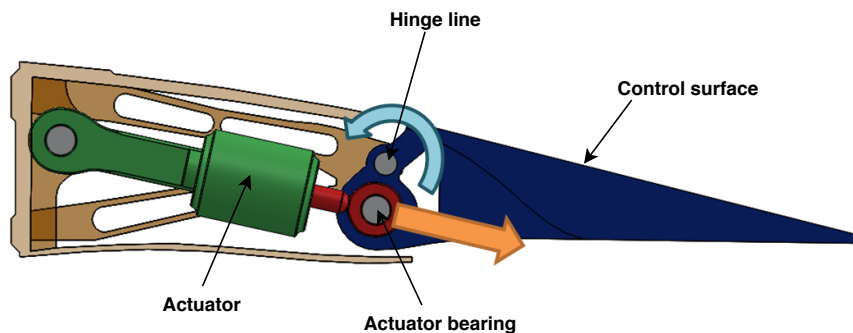


Figure 2.1.: Example of control surface section with actuator.

For the purpose of this study we will consider only the case of the Airbus EFCS and especially its primary control set (see Figures 2.2 and 2.3)

- pilot control system: sidestick and pedals
- electrical transmission system: on-board computers and electrical wires
- control surfaces: elevator, rudder and ailerons

- sensors: LVDT (Linear Variable Differential Transducer) and RVDT (Rotary Variable Differential Transducer) to measure respectively the linear displacement of the actuator rod and the control surface deflection.

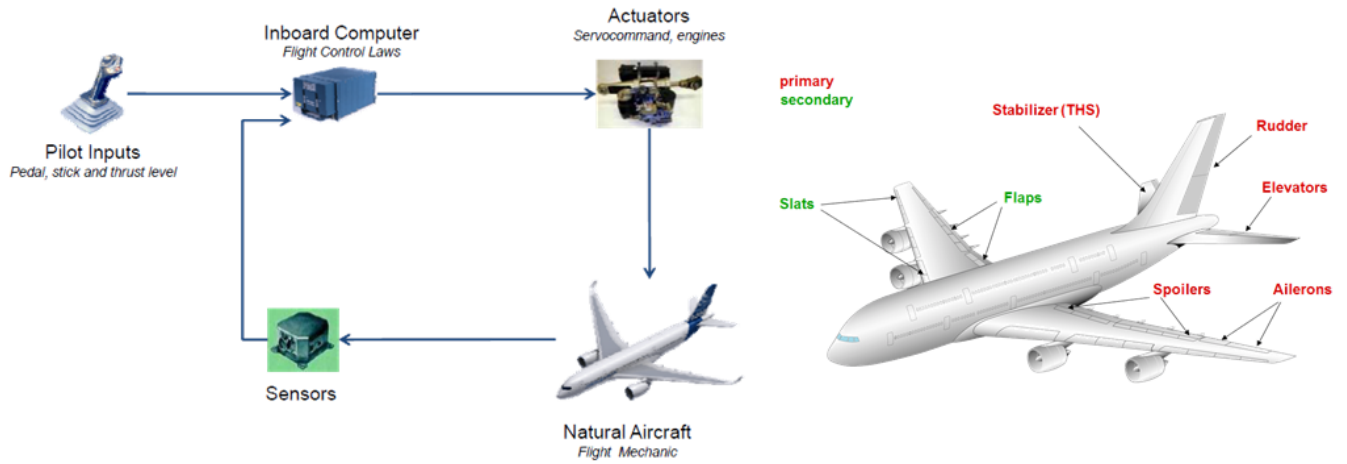


Figure 2.2.: Airbus Electrical Flight Control System (EFCS).

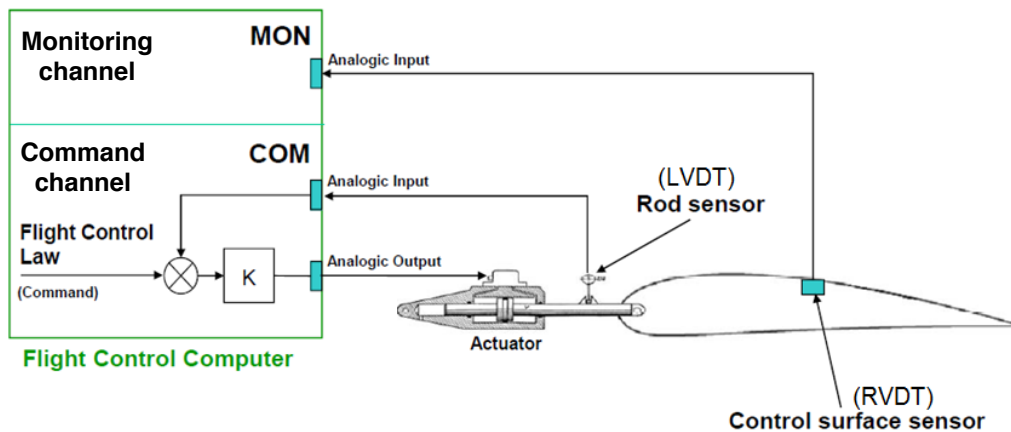


Figure 2.3.: Airbus control surface servo loop.

The EFCS has become a standard in civil aviation. However, this evolution took multiple aircraft generations. Figure 2.4 displays the historical evolution of the FCS.

**EVOLUTION OF FLIGHT CONTROL SYSTEM**

Generation	Name of aircraft	Control System of Aircraft
First Generation Aircraft	De Havilland Comet -1(1949)	Hydro mechanical
	Boeing 707 (1954)	
Second Generation Aircraft	Boeing 727 (1963) Boeing737(1967) Boeing 747(1969) Lockheed L1011(1970) McDonnell Douglas(1967) DC9 (1965) DC10 (1970) Airbus A300(1972)	Hydro mechanical
Current Generation Aircraft	A319(1995) AirbusA320(1987) AirbusA330(1992) AirbusA340(1991) AirbusA380(2005) Boeing777(1994) Boeing787(2009)	Fly-By-Wire

Figure 2.4.: Historical evolution of the Flight Control System.

To give an example of EFCS architecture, in Figure 2.5, we can see the full architecture of the A380 EFCS: the control surfaces, their location, their actuators, the redundancies, the hydraulic circuits, the on-board computers and the reconfiguration strategy<sup>1</sup>.

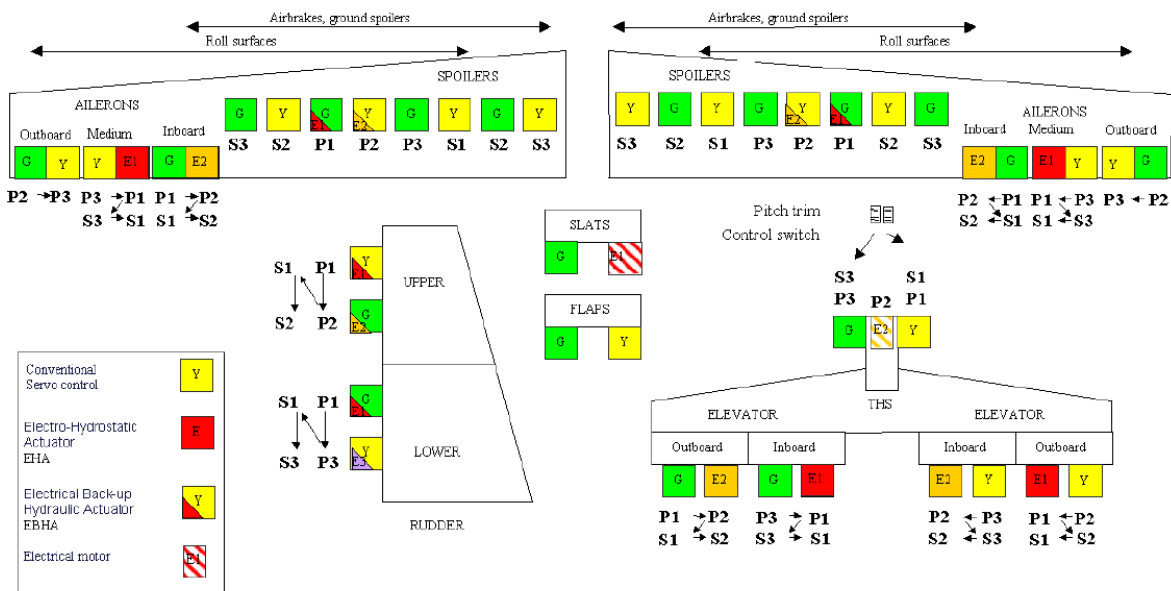


Figure 2.5.: A380 EFCS architecture.

<sup>1</sup>The system reconfiguration concerns for example a control surface with two actuators. The first one is in active mode and is controlled by a computer  $P_1$ . The second one follows the movement of the active actuator and is associated with a computer  $P_2$ . In case of failure there is a switch between the actuators.

Concerning one of the main components of the EFCS, the actuators, we can distinguish (see Figure 2.5) three main types currently in use (see Figure 2.6):

- HA (Hydraulic Actuator)
- EHA (Electro-Hydraulic Actuator)
- EBHA (Electrical Back-up Hydraulic Actuator)

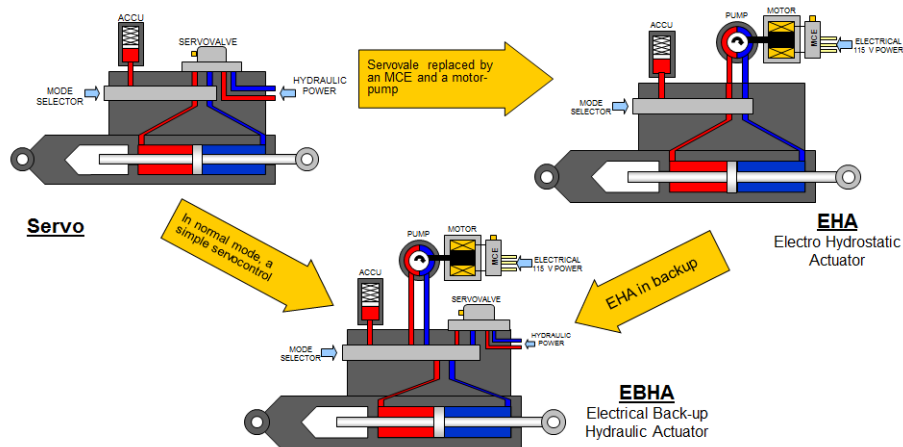


Figure 2.6.: Hydraulic actuator, Electro-Hydraulic Actuator and Electrical Back-up Hydraulic Actuator.

Hydraulic actuators (HA) have a relatively simple functioning. The command, converted to current, is sent to the actuator servo-valve which converts this current into an hydraulic fluid movement between the two chambers, which are separated by a piston, causing, by means of a pressure difference, the displacement of the rod. This type of actuator, using the hydraulic force, has the advantage of generating high torques, good control of the shaft speed and a long service life. However, these systems are massive, especially if we consider the required connection to a complex hydraulic circuit. Following a more electrical approach for the aircraft, one expect to move from the Fly By Wire (FBW) technology to the Power By Wire (PWB) technology and thus use new actuators such as EHA or EBHA. The EHA combines an electrical actuator with an hydraulic actuator. The principle is similar to the HA except that the servo valve is replaced by a pump coupled to an electric motor. The engine operates the pump which allows the flow of liquid in the chambers. This device includes an integrated hydraulic circuit, pressurized by an internal electric pump. As a function of the commands from the control system, the motor will supply more or less electricity in the pump generating a variable flow in the chambers used to control the surfaces. Such a system allows the actuator systems to be isolated from the hydraulic circuit of the aircraft, resulting in a gain of mass and dissimilarity. Indeed, even in case of an hydraulic circuit failure, the EHA or EBHA continue to operate, so the pilot is still able to manage the aircraft. The EBHA, developed

to bring more redundancy and dissimilarity, represent an hybrid solution: in normal operation it acts like an HA, while in case of a failure like an EHA. In the future, following the aircraft electrification trend, the direct use of Electro Mechanical Actuators (EMA) is considered. As the EFCS evolution, the actuator technology evolution took multiple aircraft generation (see for example Figure 2.7).

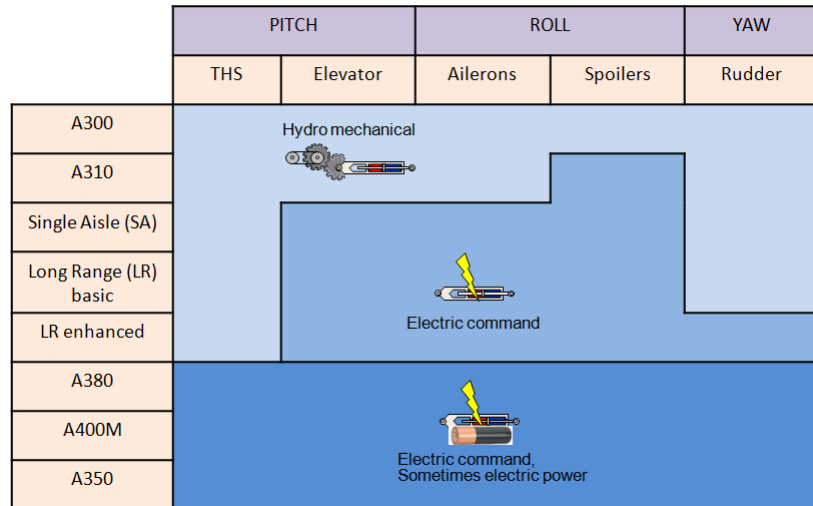


Figure 2.7.: Electrification of the FCS on Airbus aircraft.

## Fault tolerance and diagnosis in the EFCS

Fault tolerance and fault diagnosis are key points in the EFCS design. Indeed, the EFCS design is based on very stringent requirements in terms of safety and availability. Moreover, the evolution of the EFCS is related with a growing complexity of equipments and systems, an increased interaction with flight physics and finally a greater number of failure cases to be considered. Thus, the relevance of Fault Detection and Isolation (FDI) techniques is increasing with time. The state-of-practice for aircraft manufacturer for fault tolerance and diagnosis is based on some specific “golden rules” [Gou11]

- Safety System Assessment (SSA). It is essential to evaluate all the possible combinations of failures and the probability of occurrence of a certain event.
- Stringent development process. See for example [int96] for aircraft system development, [EI92] for software development and [EI00] for hardware development.
- High level of hardware redundancy. For example the use of multiple control computers, different power sources, multiple sensors.
- Real-time monitoring. Multiple algorithms run in real time to check all sent and received information in the on-board computers, but also sensors, actuators, probes, etc.

- Reconfiguration strategies: system reconfiguration and flight control law reconfiguration. The system reconfiguration concerns for example a control surface with two actuators. The first one is in active mode and is controlled by computer  $P_1$ . The second one is in passive mode (it follows the movement of the active actuator) and is associated with a second computer  $P_2$ , in stand-by mode. In case of failure there is a switch between the actuators (and the related computers) to guarantee the control of the control surface (See for example Figure 2.8). The flight control law reconfiguration is related to the definition of multiple levels of control laws (Normal law, alternate laws, direct law) as a function of the EFCS integrity and redundancy level in order to protect the aircraft from critical events [TLS04]. The reconfiguration strategy and the flight domain protection are shown in Figure 2.9.
- Dissimilarity. For example there are always at least two types of computers: a PRIMary (PRIM) and a SECondary (SEC) computer. They have different hardware, software and development teams. Different actuators technologies are also considered, for example HA and EHA as in Figure 2.8.
- Installation segregation. For example the flight control computers are physically segregated as hydraulic and electrical routes.
- Flight Control Computer architecture. For example the control (COM) and monitoring (MON) functions are dissimilar in the flight control computers (Figure 2.10).

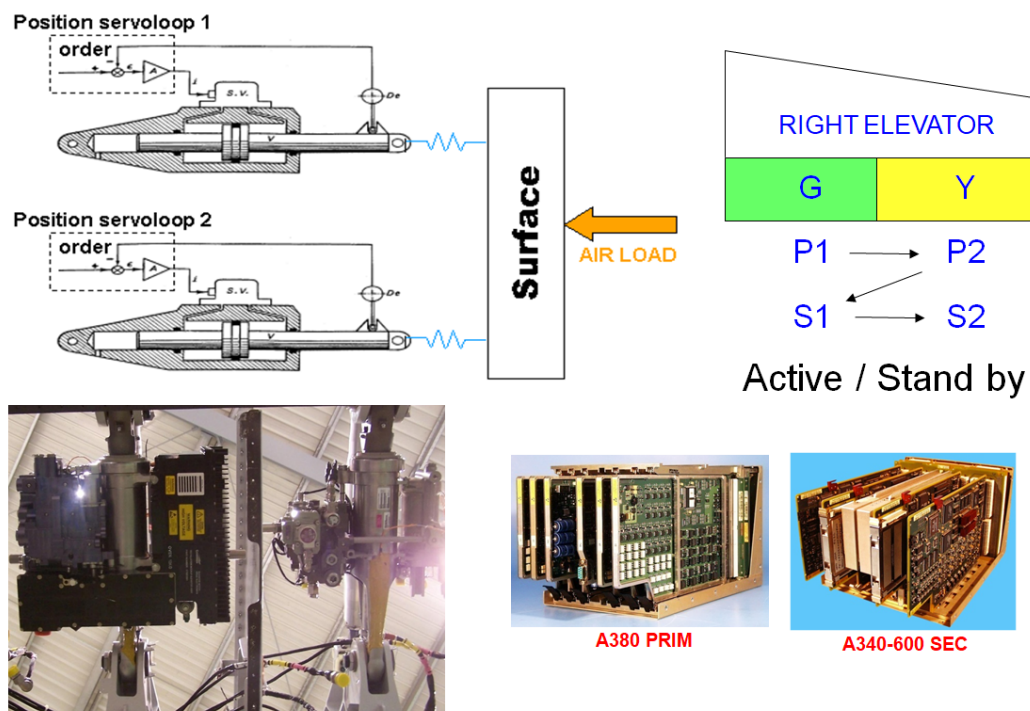


Figure 2.8.: Active/Stand-by reconfiguration and example of PRIM/SEC computers.

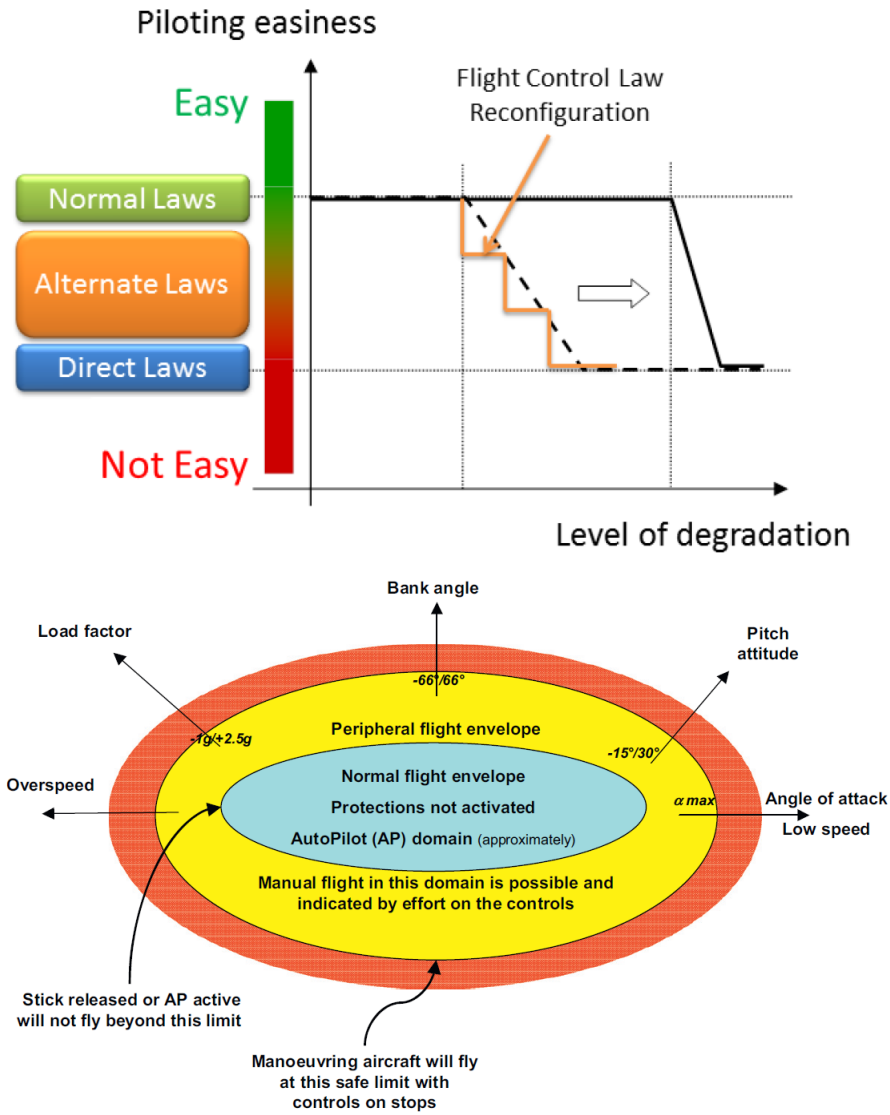


Figure 2.9.: Flight control law reconfiguration and flight domain protections [Gou11].

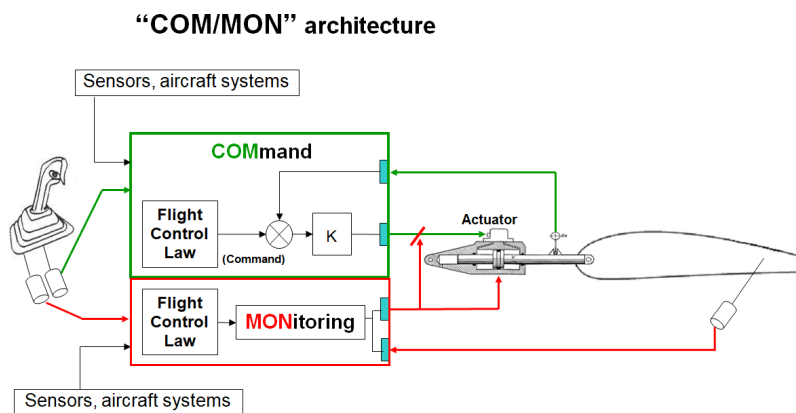


Figure 2.10.: Airbus COM/MON architecture.

## 2.3. Limit Cycle Oscillation (LCO)

In linear dynamics only two system behaviors are possible: stability and instability. In nonlinear dynamics additional behaviors can be encountered as limit cycles and chaos. Limit Cycle Oscillation (LCO) is a generic mathematical term defining an initial condition-independent periodic mode occurring in dissipative (non-conservative) nonlinear systems. The LCO appears as an instability phenomenon associated with a negative damping term in the system dynamic, which causes small perturbations to grow exponentially in amplitude until nonlinearities become important and limit the amplitude. The LCO amplitude and waveform strongly depend on the nonlinear characteristic of the system (only a discrete set of limit cycle amplitudes and frequencies may exist in a given system). Considering the complexity of the aircraft system, different LCOs exist as a consequence of different non-linear phenomena in the system dynamic. In the present study only the LCO of a generic control surface (C/S) of the aircraft is considered. In this case, the main sources of self-oscillations are

- Aerodynamic non linearity (shock-wave motion)
- Structural freeplay (for example in the control surface hinge line)
- Actuator freeplay (for example in the actuator roller bearings)
- Reduced actuator stiffness due to full/partial actuator failure
- Servo loop perturbations (for example processing delays)

In the present study we are mainly interested in studying the **freeplay induced LCO of a C/S** with the purpose of developing a dedicated detection and isolation algorithm. In order to understand the physical problem and the LCO sensitivity to different parameters, it is interesting to consider the simplified system in Figure 2.11, which represents the typical section of an aerodynamic surface with unbalanced control surface.

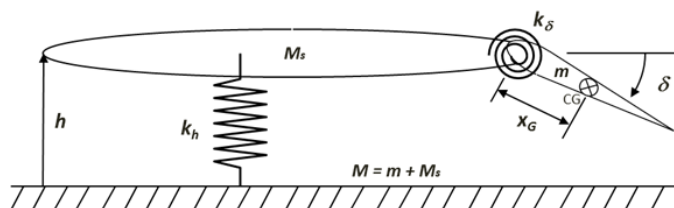


Figure 2.11.: Typical section of airfoil with unbalanced control surfaces.

It is a 2 degrees of freedom (DOF) system where the airfoil bending is called  $h$  and the control surface rotation is called  $\delta$ . We are considering a 2DOF system instead of a 3DOF (including the airfoil torsion), because the particular LCO we want to investigate is mainly related to the inertial coupling between the first bending mode of the aerodynamic surface and the rotational mode of the control surface (see Figure 2.12).

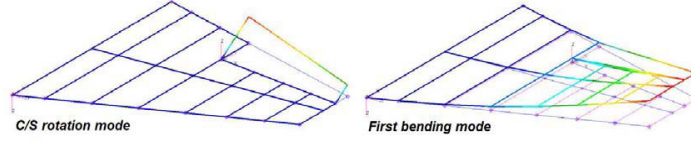


Figure 2.12.: Example of C/S rotation mode and first bending mode [PB14].

The system equation that describes a linear aeroelastic wing model is usually written as an harmonic oscillator of the form

$$\mathbf{M}\ddot{\mathbf{X}} + (\rho V \mathbf{B} + \mathbf{D})\dot{\mathbf{X}} + (\rho V^2 \mathbf{C} + \mathbf{K})\mathbf{X} = \mathbf{0}$$

where  $\mathbf{X}$  is the coordinates components vector,  $\rho$  the air density,  $V$  the air speed and the matrices  $\mathbf{M}$ ,  $\mathbf{B}$ ,  $\mathbf{D}$ ,  $\mathbf{C}$ ,  $\mathbf{K}$  represent the inertia, aerodynamic damping, structural damping, aerodynamic stiffness and structural stiffness respectively. The structural damping  $\mathbf{D}$  is often ignored as experience has shown that the aerodynamic damping  $\mathbf{B}$  dominate and that such an assumption generally produces conservative estimates of the flutter speed. So the previous equation reduces to

$$\mathbf{M}\ddot{\mathbf{X}} + (\rho V \mathbf{B})\dot{\mathbf{X}} + (\rho V^2 \mathbf{C} + \mathbf{K})\mathbf{X} = \mathbf{0}$$

For the simplified 2DOF system in Figure 2.11, it can be easily shown that the previous equation corresponds to

$$\begin{bmatrix} M_T & -mx_g \\ -mx_g & I + mx_g^2 \end{bmatrix} \begin{bmatrix} \ddot{h} \\ \ddot{\delta} \end{bmatrix} + \left( \rho V \begin{bmatrix} \frac{S}{2} C_{z\alpha} & 0 \\ 0 & 0 \end{bmatrix} \right) \begin{bmatrix} \dot{h} \\ \dot{\delta} \end{bmatrix} + \left( \rho V^2 \begin{bmatrix} 0 & -\frac{S}{2} C_{z\delta} \\ 0 & -\frac{S}{2} b C_{m\delta} \end{bmatrix} + \begin{bmatrix} k_h & 0 \\ 0 & k_\delta \end{bmatrix} \right) \begin{bmatrix} h \\ \delta \end{bmatrix} = \begin{bmatrix} 0 \\ 0 \end{bmatrix} \quad (2.1)$$

where  $M_T$  is the total mass of the section,  $I$  the C/S rotational inertia,  $m$  the C/S mass,  $x_g$  the distance between the hinge line and the C/S CG,  $k_h$  and  $k_\delta$  are the pitch and rotational stiffness,  $S$  the airfoil reference surface and  $C_{z\alpha}$ ,  $C_{z\delta}$ ,  $C_{m\delta}$  the aerodynamic stability derivatives of the aerodynamic force and moment produced by the airfoil. From the previous equation we can see that the bending and rotational mode are coupled via the term  $mx_g$  in the inertia matrix ( $x_g \neq 0$  for an unbalanced control surface). Moreover, we can see that the third term can assume also negative values as the air speed increase. Given that this term represents the system global stiffness, that implies negative damping values. In this case, damping may destabilize the system by feeding energy instead of removing it. For a linear system a negative damping will result in a divergent system behavior (Flutter). However, as in reality there are always some nonlinearities, then other behaviors can be encountered as limit cycles and chaos (small perturbations grow exponentially in amplitude until the nonlinearities effects become important and limit the amplitude). Nonlinearities introduce new behaviors between the stability

and instability domain of the system. For example, for an unbalanced control surface, a freeplay in the C/S hinge line or in the actuator bearing can be modeled as a nonlinear behavior of the rotational stiffness  $k_\delta$ . This nonlinearity introduces a particular type of LCO that is usually called freeplays induced LCO. This LCO can be seen as a periodic switch between a stable state (tightened control surface) and an unstable state (free control surface). Indeed, the C/S can vibrate inside its freeplay. It should be mentioned that the name “freeplays induced” is somehow misleading because it is not the freeplay that start the LCO and for an unloaded control surface, the flow velocity at which LCO begins is independent of the degree of freeplay [Dow15]. However, the amplitude of the LCO and the amount of loading required to preclude LCO is strongly dependent on the degree of freeplay (the angle of attack required to totally eliminate freeplay is usually about five times the degree of freeplay [Dow15]). In other terms, old aircraft (higher freeplay level) triggers LCOs of higher amplitude than a brand new one, because of the reduced equivalent stiffness (see Figure 2.13). Given that the LCO amplifies the freeplay, the LCO amplitude will increase each time the phenomenon is triggered. If the nonlinearity (freeplay) has the desired effect of limiting the oscillation amplitude for air speeds larger than the linear flutter velocity  $U_F$  (super-critical LCO), it might have also the undesired effect of inducing oscillation for lower air speeds than  $U_F$  (sub-critical LCO) [Lub08]. See also Figure 2.14.

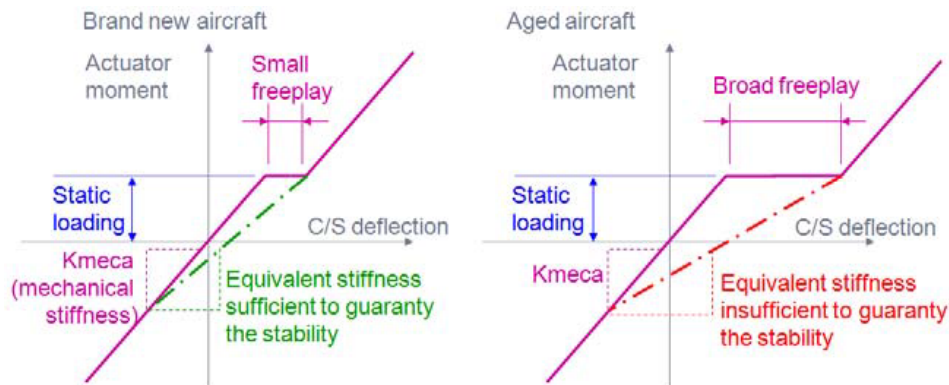


Figure 2.13.: Equivalent C/S rotational stiffness : new/aged aircraft [Loz08].

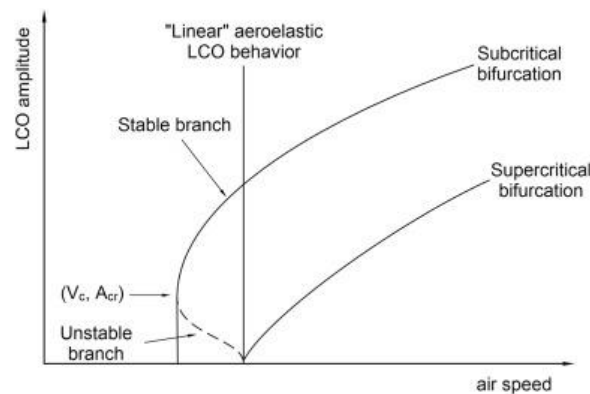


Figure 2.14.: Sub-critical and super-critical LCO [Dow15].

In order to better understand the physical phenomenon, it is interesting to observe the results of some simulations. In Figure 2.15, 2.16, 2.17 we can observe the initial condition response of a mathematical model representing a wing section with control surface (flap and control surface rotation as the one in Figure 2.11). In Figure 2.15 we have the reference initial condition response of the system. In Figure 2.16 it is interesting to see how the introduction of a small dead zone on the rotational stiffness (representing the freeplay) can lead to LCO. Moreover, Figure 2.17 confirms that reducing the coupling term  $mx_g$  the LCO can be avoided for the considered freeplay level.

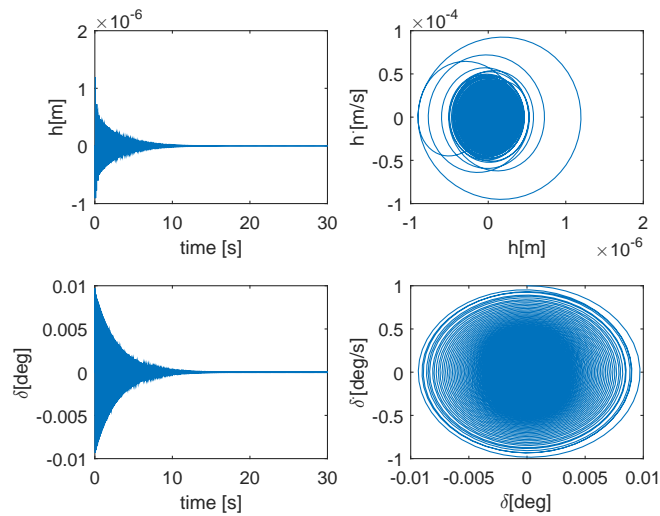


Figure 2.15.: Initial condition response of a wing section with control surface (see (2.1)). A stable convergent response can be observed.

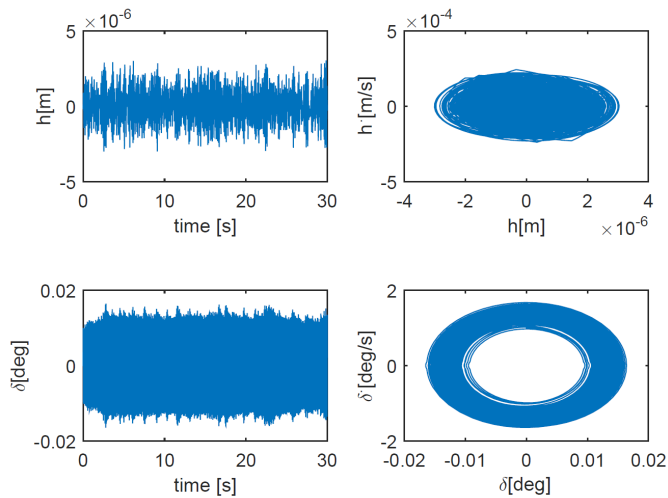


Figure 2.16.: Initial condition response of a wing section with control surface and freeplay. The same mathematical model (2.1) of Figure 2.15 is considered, but a symmetric dead zone on the rotational stiffness is considered to simulate the mechanical freeplay. An LCO-type behavior can be observed due to the freeplay.

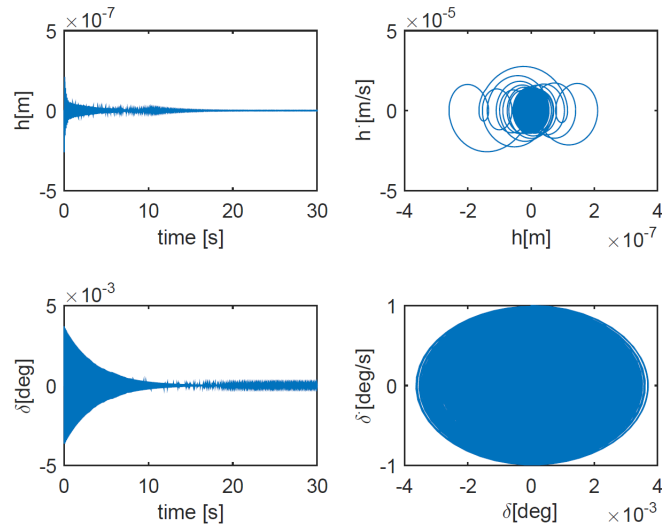


Figure 2.17.: Initial condition response of a wing section with control surface and freeplay. The same mathematical model (2.1) and the same free play level of Figure 2.16 is considered; but here the center of gravity of the control surface is five times closer to the hinge line  $x_g = x_g/5$ . A stable convergent response can be observed.

In Figure 2.18, 2.19 we can compare frequencies and damping of the wing section models described in [Wri+03]. In Figure 2.18 a 3 degrees of freedom wing section model is considered (flap, torsion, rotation), while in Figure 2.19 a wing section with actuator is considered (both the models are detailed in [Wri+03]).

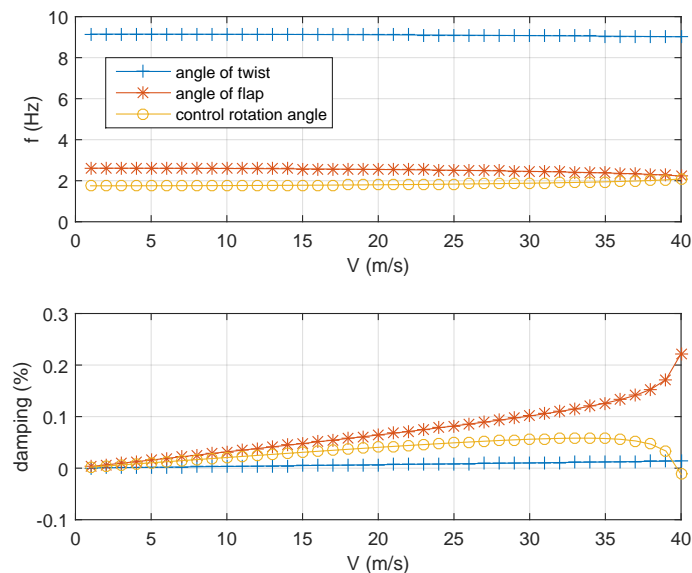


Figure 2.18.: Frequency and damping (as a function of the wind speed) for a wing section with control surface (3 degrees of freedom : flap, twist, rotation) [Wri+03].

It is interesting to observe how the introduction of the actuator model has a strong impact on the system damping. In Figure 2.20, 2.21, 2.22 we can observe different initial condition responses for the model with actuator in Figure 2.19. Comparing Figures 2.20 and 2.21 it can be seen how the introduction of a symmetric

dead zone on the actuator torque (representing the freeplay) leads to an LCO-type behavior. Furthermore, comparing Figures 2.21 and 2.22 it can be observed that increasing the actuator stiffness we can avoid LCO.

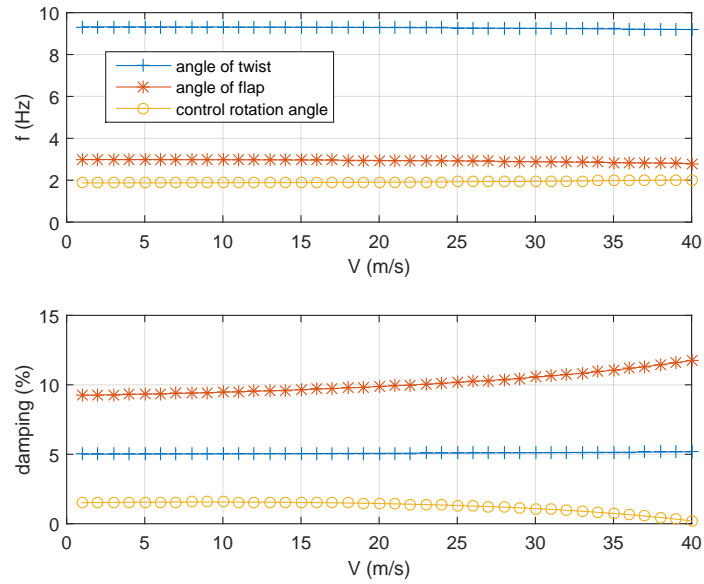


Figure 2.19.: Frequency and damping (as a function of the wind speed) for a wing section with control surface and actuator [Wri+03].

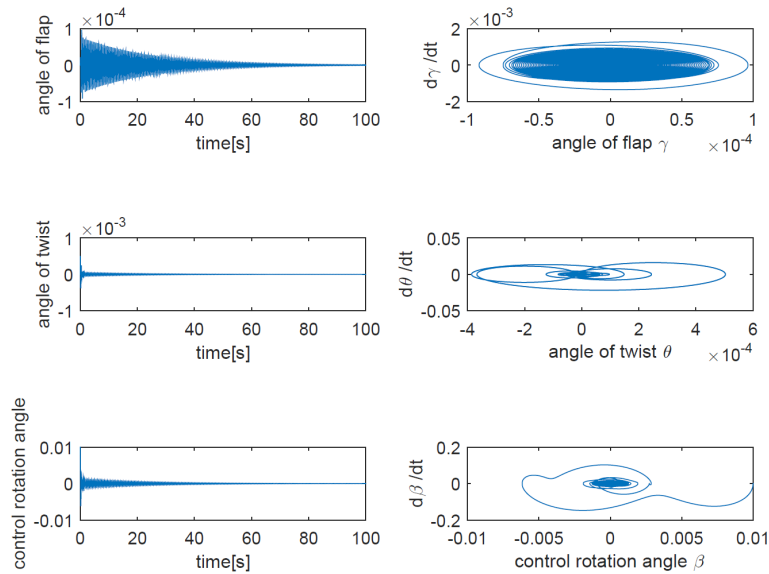


Figure 2.20.: Initial condition response at 39 m/s for the model of Figure 2.19. A stable convergent response can be observed.

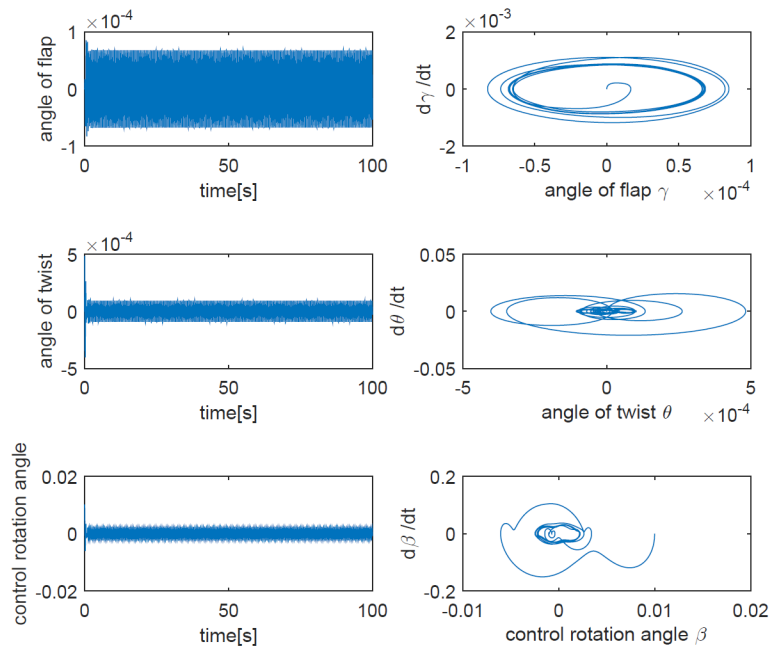


Figure 2.21.: Initial condition response at  $39\text{ m/s}$  for the model of Figure 2.19 where a symmetric dead zone has been considered on the actuator torque to simulate the freeplay. An LCO-type behavior can be observed.

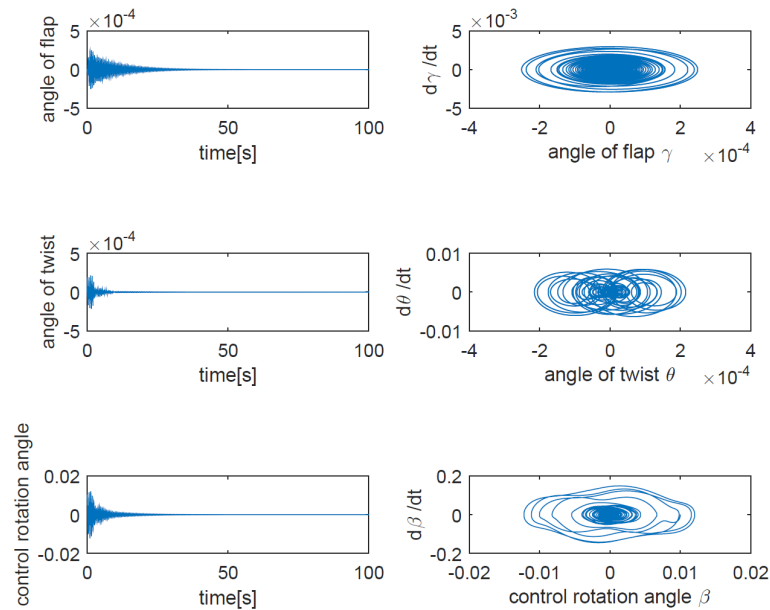


Figure 2.22.: Initial condition response at  $39\text{ m/s}$  for the model of Figure 2.20 where an higher actuator stiffness has been considered (area of pressure stabilization piston is 3 times bigger). A stable convergent response can be observed.

Observing the LCO phenomenon at aircraft level, it can be seen that for the LCO to start, multiple conditions have to be met

- Inertial coupling (unbalanced C/S)

- Particular flight conditions (Speed, altitude, attitude, configuration)
- C/S locally free to rotate with insufficient static loading

A simple way to evaluate if LCO can trigger is to compare the C/S available loading versus the minimum load to preclude the LCO. If during a particular flight phase the C/S available loading is lower than the minimum load precluding LCO, then LCO can trigger (see Figure 2.23).

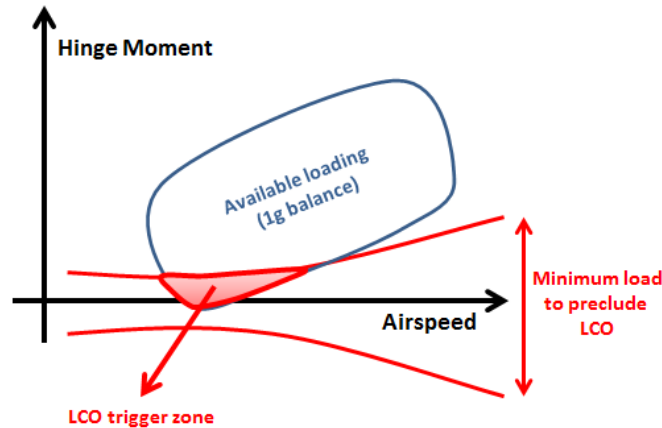


Figure 2.23.: LCO trigger zone, comparison between C/S available load and minimum load to preclude the LCO.

Experience has shown that the most critical maneuvers for LCO triggering on the elevators are the  $N_z$  maneuvers (and the airbrakes are an aggravating factor). In particular, the level capturing maneuver at the end of the climb, the initial descent (with airbrakes partially out) and deceleration phases can be considered as the flight phases where LCO is more likely to trigger on elevators. The problem is quite different for the rudder. Considering that the static load is generally close to zero, all the flight phases can lead to LCO. On the other hand, ailerons are generally more aerodynamically loaded in all the flight envelope and then they are less prone to vibrations.

For further details on the LCO phenomenon the reader can refer to [Dow15] or to the extensive literature on the topic concerning theory, modeling and experimental analysis, for example [Dim99] [Kho14][TD11] [TVD02][GK08][Con+97] [Vas+14] [Sut12][Nob13] [GMM08] [PB14]. Concerning the interaction between wear process and limit cycle oscillations, the reader can find an interesting description in [SKA02], where wear models and predictive equations are presented and where it is shown that the sliding wear damage has a predominant effect compared to the impact wear damage. Moreover, it is observed that, if a vibration occurs, the rate of development of the freeplay can increase exponentially.

Finally, from a signal analyst point of view, it is interesting to note that

- the LCO behavior can be seen as a pure sinusoidal signal at a given frequency (depending

on the system dynamic) that can be measured on the flap, twist and control surface rotation of the wing section (see Figures 2.16 and 2.21).

- the LCO amplitude strongly depends on the freeplay level, but the freeplay alone is not a sufficient condition for LCO to trigger as multiple conditions have to be met (see Figures 2.23, 2.17 and 2.22).

## 2.4. State-of-the-art

The first events of control surface flutter occurred during the 1st World War and the most widely adopted solution was to consider control surface mass balancing [VK23] ( $x_g$  small or  $\leq 0$ ). Indeed, the LCO problem is critical for unbalanced control surfaces. The static balancing of the control surface that is generally considered for light aircraft in general aviation and sometimes in commercial aviation (see Figure 2.24) has the advantage of reducing the LCO probability in the flight domain (see also Figure 2.17). However the weight penalty is generally high and it is difficult to guarantee the balance during all the operational life of the aircraft. Indeed, repairs and maintenance operations, but also particular atmospheric conditions (icing) can lead to a balance modification.



Figure 2.24.: Example of balanced control surfaces (ATR72 and Messerschmitt Bf110).

In 80-90s, the hydraulic actuators, that were introduced to reduce the command effort, became reliable enough to ensure the aeroelastic stability by their own stiffness (see Figure 2.22) or damping. For this reason, the C/S mass balancing was given up because of its drag and weight penalty. Unfortunately, the actuator stiffness/damping solution also presents a weak point: with the cumulative wear (aircraft aging), some supporting elements of the control surface develop mechanical freeplay and so, as explained in the previous section, the C/S can vibrate inside its freeplay. For this reason, the actuator stiffness/damping solution has to be coupled with other countermeasures

- Crew sensitivity. The pilot/crew can fill in a so-called “Vibration Reporting Sheet” (Airbus) or a “Flight

Deck Vibration Event Log” (Boeing) to describe the phenomena felt during the flight (see Figure 2.25). This process is thought to ease the vibration root cause isolation. However, a lot of dispersion can be observed on the pilot responses and on the use of this feedback by the airlines.

- Periodic freeplay check (Figure 2.27). Regular check (on ground) of the freeplay level for every actuator are scheduled in order to verify if it is compliant with the maximum levels fixed for each C/S. The check is complex and time consuming and the residual freeplay on other components of the C/S (for example the hinge line) can lead to vibrations even after an actuator bearing replacement (see Figure 2.26). Specific devices can be used to automate the freeplay check (see for example Embraer patent [VAO17]), but generally an expert technician is needed.
- Artificial C/S static loading. To give an example, on the A380 upper rudder there is a device called CAM [Mor07] creating a static torque in order to reduce the potential freeplay effect and avoid LCO in flight. The presence of this device can be guessed looking at the A380 upper rudder on ground (deflected when the actuators are not active). See Figure 2.28.
- Low play articulation technologies. For example roller bearing instead of autolube bearings.
- Active control. There is a wide literature about active control of vibrations like the LCO. However, there are not a lot of documented real applications in civil aviation. An example is the Boeing outboard aileron modal suppression (OAMS) system. The OAMS is designed to dampen out a structural sustained vibration at 2.3Hz of the B747-8 wings, engine pylons and fuselage [Liv17]. The FAA has added OAMS to the master minimum equipment list, prohibiting the aircraft from being dispatched with the system inoperative. The OAMS system is built out of the 747-8’s roll-axis fly-by-wire flight control system to reduce the amplitude of the sustained oscillation. More recently, on the Boeing 787-10 a flaps-up vertical modal suppression system (F0VMS) has been considered as damping-augmentation system for a low damped aeroelastic mode at 3Hz. In [Liv17] the state-of-the-art and the technology maturation needs for aeroelastic active control is addressed. Other interesting references are [CDF00][Bia14][Cas15][MDM17].
- **Condition monitoring algorithms. The methods investigated in this study and detailed in Chapters 3 and 4 are part of this category (Section 2.5 clarifies this choice).** A well-known example in this category is Boeing patent [PK11]. The idea is to analyze the maximum of the frequency spectrum of the control surface system seen as a hybrid system: free pendulum in the freeplay zone and constrained pendulum out of the freeplay zone. The lower the frequency of the maximum of the frequency spectrum, the bigger the freeplay level (free pendulum frequency is lower than constrained pendulum frequency). Other technical solutions are described in [Sch+18][Bal+09] for Electro-Mechanical Actuators. Concerning LCO prediction the reader can also refer to [EP13][Ven+16] [Sed+00]. For a general

survey of time-series methods for fault detection and identification in vibrating structures the reader may also refer to [FS06].

**A320 VIBRATION REPORTING SHEET**

**IMPORTANT:**  
THE VIBRATION REPORTING SHEET MUST BE FILLED IN PROPERLY BY THE FLIGHT CREW (ALL FIELDS MARKED \*) ARE MANDATORY). OTHERWISE, TROUBLE SHOOTING WILL BE DIFFICULT OR NOT POSSIBLE.

NOTE: FOR MAINTENANCE PERSONNEL, REFER TO TSM TASK 05-50-00-10-901 FOR FAULT ISOLATION PROCEDURE.

IN EACH BOX, PLEASE TICK THE CORRESPONDING DIVISION.

GROSS WEIGHT:  ALT:  SPEED:

ENG VIBRATION PARAMETERS: #1:  #2:

FLIGHT PHASE:  CLIMB  CRUISE  DESCENT  APPROACH

AIR TURBULENCE: YES  NO  LG: UP  DOWN

\* SLAT/FLAP POSITION: 0  1  2  3  FULL

\* FLIGHT CONTROL OSCILLATION IS VISIBLE ON ECAM: YES  NO

-> IF YES, ON: RUDDER  ALERON  ELEVATOR

\* FLIGHT CREW TRIED TO STOP VIBRATION BY FLIGHT CONTROL INPUT: YES  NO

-> IF YES, VIBRATION CAN BE STOPPED BY FLIGHT CONTROL INPUT ON:

① ROLL  YAW  ② PITCH  AIRBRAKE

③ INPUT SHOULD BE DONE USING SIDE STICK WITH AP OFF

④ INPUT SHOULD BE DONE USING RUDDER TRIM WITH AP OFF

\* VIBRATION CAN BE STOPPED BY FOLLOWING PARAMETER CHANGE:

THRUST  ALTITUDE

\* AFFECTED AREA:

COCKPIT  FWD CABIN  MID CABIN  AFT CABIN

SPECIFIC LOCATION:

\* AUDIBLE NOISE  RUMBLING NOISE

\* VIBRATION INTENSITY: LIGHT  MODERATE  STRONG

\* VIBRATION FELT IN: LATERAL  VERTICAL  UNKNOWN

GENERAL CREW COMMENTS (I.E. FREQUENCY, ORIGIN, NOISE, SPEED CHANGE EFFECT, VIBRATION STOPS AT END OF CLIMB, VIBRATION STARTS AT BEGINNING OF THE DESCENT, AP STATUS, ... ANY OTHERS COMMENTS):

-----

**1 VIBRATION LOG**

**Flight Deck Vibration Event Log**

To assist in the resolution of any vibration observed in the flight deck or in the cabin, please complete the following:

Date:  Airplane:  Model:  Takeoff gross weight:

Flight condition at approximate onset (please check applicable box):

T/O roll  Climb  Cruise  Hold  Descent  Landing

Altitude:  Airspeed:  Mach:  Autopilot:  On  Off

Eng. #1, 2, 3, 4  %N1  %N2  Eng. vib:  #1  #2  #3  #4

What event, if any, initiated the vibration?

What event, if any, caused the vibration to stop?

Was the vibration continuous or intermittent?  Continuous  Intermittent

How did the vibration start and stop?  Started/stopped suddenly  Started/stopped slowly

What was the magnitude of the vibration?

Barely perceptible  Clearly noticeable  Annoying  Uncomfortable

What were the characteristics of the vibration (please check one)?

Low frequency: Motion could be felt by the whole body. Motion of sun visors or window heater cable might have been noticeable.

Direction:  Mostly lateral  Mostly vertical  Vertical and lateral

Higher frequency: Vibration could be felt tactfully with the hands or feet.

Where was the vibration noticeable, and where was it the strongest?

Noticeable:  Flight deck  Passenger cabin  Aft galley

Strongest:  Flight deck  Passenger cabin  Aft galley

Describe in detail the location(s) where the vibration was felt or not felt (use body station, seat row, component name, etc.):

If a noise was associated with the vibration, describe the characteristic of the noise (e.g., drone, buzz, whine, whistle):

Additional description of vibration and noise or other observations:

Figure 2.25.: “Vibration Reporting Sheet” (Airbus) and “Flight Deck Vibration Event Log” (Boeing).

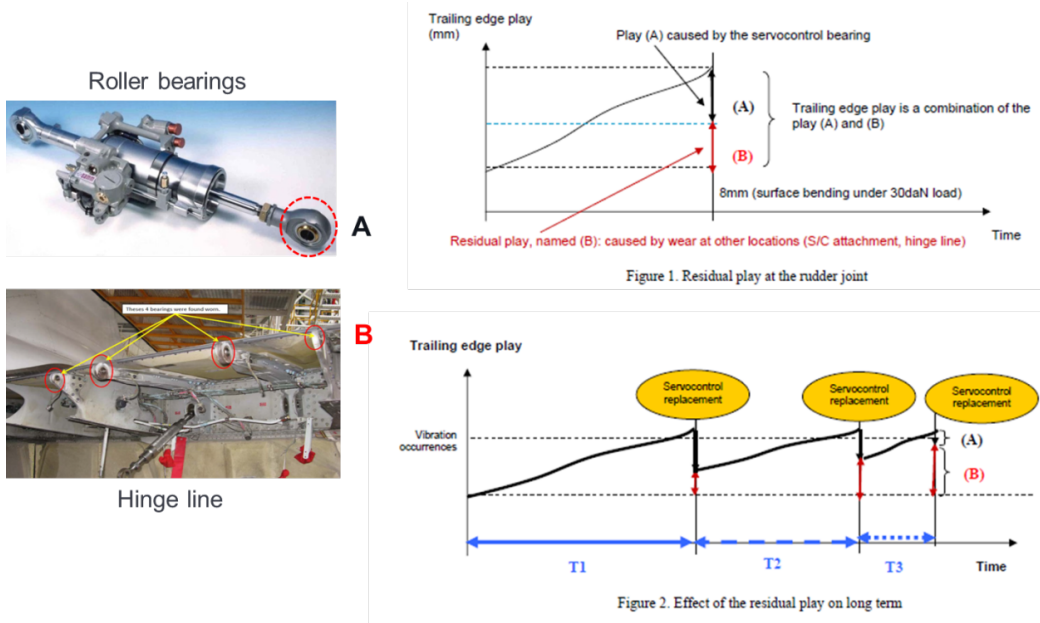


Figure 2.26.: Effect of the residual play on long term.

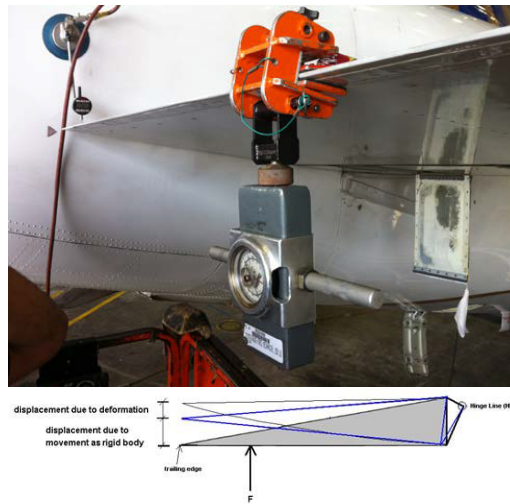


Figure 2.27.: Freeplay check operation.



Figure 2.28.: CAM device on the A380 upper rudder.

The need for a careful handling of freeplays and LCO vibrations is emphasized also by the authorities. The Federal Aviation Administration (FAA) policy for the design, certification, and continued airworthiness of unbalanced or partially balanced control surfaces is expressed in the Memorandum ANM-05-115-019 [Adm07]. The freeplay levels recommended by the FAA to preclude LCO are still the values established in 1993 in the military report MIL-A-8870C [Air93]. The FAA can also consider special amendments for specific aircraft models (see for example [FAA02][FAA15]). Concerning LCO it is mentioned that “recurring LCO must not be allowed within the airplane normal operating envelope (at speeds less than or equal to VC/MC). However, LCO is not itself aeroelastically unstable, and accelerated wear may not be an issue for short exposure periods”.

## 2.5. LCO and freeplay condition monitoring

In the Airbus architecture, the servo loop that moves the control surface (see Fig. 2.3) is already monitored by several fault detection algorithms [Gou10][Zol+13]. Indeed, there are numerous studies related to a different C/S oscillation problem, the Oscillatory Failure Case (OFC). OFC is mainly related to internal faults of the FCS as faulty behaviour of an electronic component or a mechanical failure (while the LCO is related to non linear aeroelasticity) and OFC has a relatively wide frequency band (compared to LCO). OFC is generally tackled using analytical redundancy approaches [Gou10], but other studies [Zol+13][Sim11] [GUT16][Urb+17a] have also considered data-driven approaches (fault modelling strategy based on Kalman filtering or using a specific observer, selective filtering, correlation methods, synchronous detection, distance methods). Inspired by the literature on OFC detection and observing that: (i) **LCO detection still depends almost entirely on crew sensitivity to vibrations** (ii) LCO prevention is based on complex and tricky maintenance operations (to verify the freeplay level); we have decided to investigate the possibility of developing simple software solutions for LCO detection and freeplay estimation (condition monitoring countermeasure) based on existing measurement and compliant with real-time implementation constraints in the Airbus architecture.

In Chapter 3 and Chapter 4 two specific methods will be presented for LCO detection and freeplay estimation: the Generalized Likelihood Ratio Test for LCO detection (Chapter 3) and the Wiener model identification for freeplay estimation (Chapter 4). This choice is based on the following observations (that will be recalled and deepened in the next chapters)

- The LCO detection problem can be modeled as a binary hypothesis testing problem. Indeed, the LCO appears like an additive oscillation on the control surface position measure. Thus, we can model the detection problem as

$$\begin{cases} H_0 : & y(n) = \mathbf{P}[x(n)] + w(n), & w(n) \sim \mathcal{N}(0, \sigma^2) \\ H_1 : & y(n) = \mathbf{P}[x(n)] + s(n) + w(n), & s(n) = A \cos(2\pi fn + \phi) \end{cases} \quad (2.2)$$

where  $n = 0, 1, \dots, N - 1$ ,  $\mathbf{x}$  represents the signal from the flight control computers sent to the actuator,  $\mathbf{P}$  the actuator dynamic,  $\mathbf{y}$  the control surface rotation measure,  $\mathbf{w}$  a white Gaussian noise of known variance<sup>2</sup> and  $\mathbf{s}$  **the anomaly that we want to detect: the LCO**. For this problem, if no a priori information about the probability of each hypothesis is available, the likelihood ratio test (LRT) in the Neyman-Pearson sense maximizes the probability of detection for a given probability of false alarm [Kay98]. Finally, in case of unknown parameters in the observation model, a very common approach is to consider the GLRT, which replaces the unknown parameters by their estimates under both hypotheses.

<sup>2</sup>the noise variance can be derived from flight data

- In the literature the most common approaches for freeplay estimation are based on load/displacements plots (Figure 2.29) and spectral analysis [PK11][KDP06].

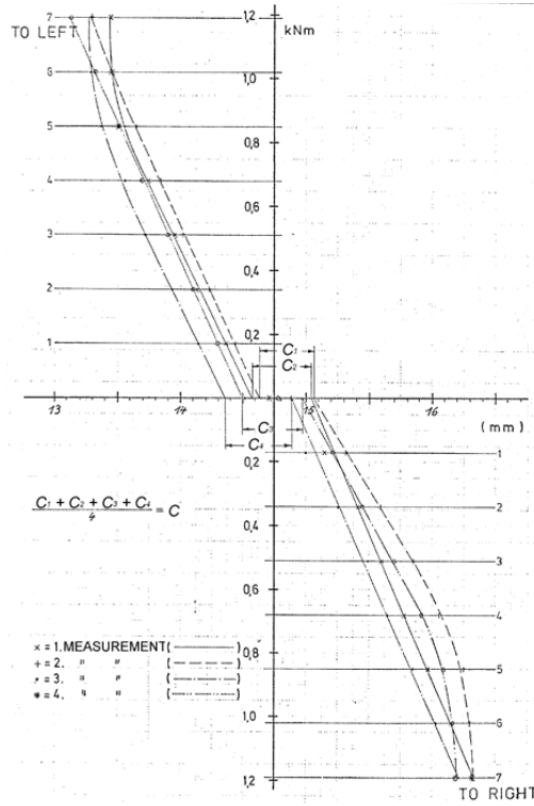


Figure 2.29.: Example of freeplay estimation via load/displacement plot [Lub08].

However, this type of methods requires specific additional sensors and specific constraints on the test configuration (sampling, input type). In the same way, a model based approach would require a long validation process and it is generally hard to generalize to different aircraft and control surfaces. For these reasons, we have decided to investigate the theory of nonlinear block-structured model identification (in particular Wiener models) for the purpose of freeplay estimation. Indeed, we are interested in a method that does not require additional sensors, has less constraints on sampling frequency and input type (compared to spectral methods) and that can be easily generalized to different control surfaces. A nonlinear Wiener model can be defined as

$$y_n = g(\omega_n) + z_n, \quad \omega_n = \sum_{p=0}^P \lambda_p x_{n-p}, \quad 1 \leq n \leq N \quad (2.3)$$

where  $\mathbf{y}$  represents the control surface rotation measure,  $x_n$  the signal from the flight control computers or the rod position measure,  $z_n$  white Gaussian noise,  $\lambda_p$  the coefficients of the impulse response of the linear subsystem and  $g()$  **the output nonlinear function representing the freeplay effect**. Thus,

the free play monitoring can be accomplished through the estimation of  $g()$ . In Chapter 4 we will see that it is very interesting to consider a nonparametric model for the static nonlinearity in order to extend the applicability of the Wiener model.

## 2.6. Challenges

Receiving and hosting a growing amount of data, thanks to the evolution of the acquisition, communication and storing chain and the development of new specific on-board systems like the ACMS (Aircraft Condition Monitoring System), new services can be proposed to the airlines, as for example predictive maintenance solutions (see Figure 2.30). Furthermore, the growing amount of data enables also the pertinent use of data-driven techniques that have an higher level of genericity and do not require any physical model development and validation process.

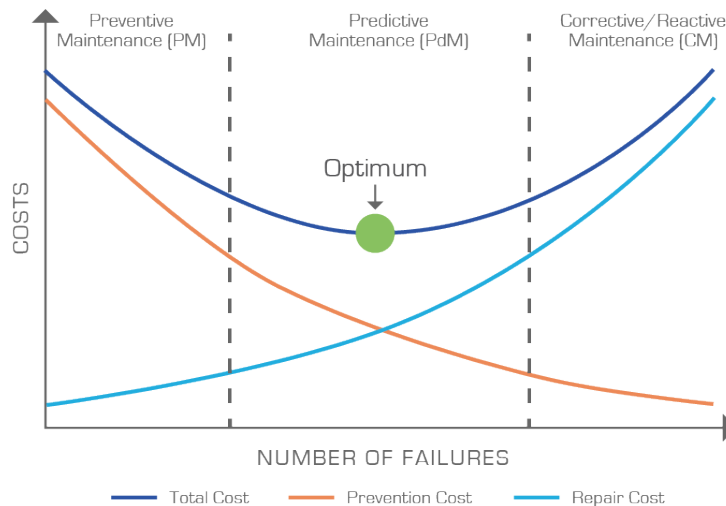


Figure 2.30.: Predictive maintenance.

The present study is thought to bring a contribution in the specific domain of data-driven solutions for condition monitoring. Indeed, the methodologies presented in Chapter 3 and 4 can be adapted to several similar applications. However, considering the study case of LCO detection and diagnosis in the Airbus architecture, some additional constraints have to be taken into account and this can lead to substantial modifications of the final solution (see for example Chapter 5). The main challenges in the development of a feasible solution for LCO detection and diagnosis in the EFCS are

- **Genericity.** The heterogeneity of the EFCS among aircraft types and generations makes it difficult to define a generic method. For example the available signals and their sampling frequencies may vary considerably among aircraft generation and control surface direction. Moreover, as previously explained, the EFCS is a system in continuous evolution.

- The hardware capacity. As a function of the system where the software solution would be hosted, different solutions have to be proposed. Solutions hosted on a server on-ground (no/few RAM and CPU limitations) or running on-board in real time have to be completely different.
- The lack of information. To give an example, generally we do not have accelerometers or load data on the tail plane or on the control surfaces of commercial aircraft. Moreover, the EFCS has not been originally thought for LCO detection. As a consequence, the sampling frequency may not be adapted for the purpose.
- Robustness. Commercial aircraft as the A320 have a really high level of reliability and availability. In order to improve the state of the art it is essential to guarantee at least the same level of reliability and availability (being able at the same time to detect the anomaly).

## 2.7. Conclusions

This chapter presented the EFCS, the LCO phenomenon, the state-of-the-art and the challenges related to LCO detection and diagnosis. From this short introduction to the problem of freeplay induced limit cycle oscillation detection in the flight control system, the reader should remember the following points

- the LCO is an aeroelastic vibration that concerns unbalanced C/S of the aircraft.
- an augmented mechanical freeplay in the actuator bearings or hinge line of the C/S is an aggravating factor for LCO. The LCO amplitude strongly depends on the freeplay level, but the freeplay alone is not a sufficient condition for LCO to trigger.
- the LCO consequences are local structural load augmentation, flight handling qualities deterioration, actuator operational life reduction, cockpit and cabin comfort deterioration, maintenance cost augmentation.
- the state-of-the-art for LCO detection and prevention is mainly based on the pilot sensitivity to vibrations and to regular freeplay check on ground.
- this study is thought to propose a data-driven condition monitoring solution to help LCO diagnosis and freeplay isolation. The goal is to improve even more aircraft availability and reduce the maintenance costs. Indeed, a condition monitoring signal would enable the airlines to ease the troubleshooting and to simplify the maintenance tasks.
- the LCO can be seen as a pure sinusoidal signal at a given frequency (depending on the system dynamic) that can be measured on the flap, twist and control surface rotation of the wing section.
- the development of a data-driven condition monitoring algorithm in the EFCS has to face multiple challenges: robustness, lack of information, hardware capacity, hardware heterogeneity and evolution.

# 3

## LCO detection via GLR tests

### Contents

---

<b>3.1. Introduction</b> . . . . .	<b>29</b>
<b>3.2. Binary Hypothesis testing</b> . . . . .	<b>29</b>
<b>3.3. LCO detection</b> . . . . .	<b>31</b>
<b>3.4. Matched filter and GLRT special cases</b> . . . . .	<b>32</b>
<b>3.5. Deterministic signal detection in interference</b> . . . . .	<b>37</b>
<b>3.6. Approximate GLRT</b> . . . . .	<b>40</b>
<b>3.7. Detection performance</b> . . . . .	<b>42</b>
<b>3.8. Sinusoidal signal detection in deterministic interference</b> . . . . .	<b>44</b>
3.8.1. Maximum Likelihood Estimators and Test Statistic . . . . .	45
3.8.2. Theoretical performance . . . . .	47
3.8.3. Synthetic data . . . . .	48
<b>3.9. Conclusions and perspectives</b> . . . . .	<b>50</b>

---

### 3.1. Introduction

The purpose of this Chapter is to study a suitable test statistic for *Limit Cycle Oscillation (LCO)* detection. The definition of the detector is achieved using an incremental approach: (i) the problem is modeled as a binary hypothesis testing problem (as already mentioned in Section 2.5); (ii) several simple detectors are proposed where one or more parameters are known; (iii) a very general formulation is proposed and validated. (iv) some variants and simplifications of the general formulation are proposed. A particular attention is dedicated to the derivation of the asymptotic performance in the general case with the purpose of simplifying the tuning process. The main theoretical contributions of this chapter have been published in [Urb+18b].

### 3.2. Binary Hypothesis testing

In a binary hypothesis testing problem, if no a priori information about the probability of each hypothesis is available, the likelihood ratio test (LRT) in the Neyman-Pearson sense maximizes the probability of detection for a given probability of false alarm [Kay98]. Unfortunately, optimal statistical tests such as the LRT cannot always be implemented since there are often some unknown parameters in the observation model, leading to the

so-called composite hypothesis testing problem (CHTP) [Van68] (also referred to as joint detection estimation problem [GCL10]). A very common approach in this situation is to replace the unknown parameters in the LRT by their maximum likelihood estimators (MLEs), following the ideas of the generalized likelihood ratio test (GLRT) [Van68]. It is known that the GLRT does not generally preserve the optimal properties of the LRT. However, the GLRT approach has several advantages for common linear models: 1) the test is often easy to derive, 2) the distribution of the GLRT statistics can often be determined analytically [Kay98], 3) the GLRT is known to be the uniformly most powerful (UMP) test for some classes of problems in the asymptotic region [SF94], 4) the distribution of the GLRT can be determined analytically for a class of linear observation models with a known observation matrix and it is known to perform as well as the optimal LRT in this particular case [Kay98]. It is important to mention that there exist different MLEs, depending on the considered observation model. In particular, if the vector of observations is formed from a linear superposition of several signal sources to Gaussian noisy data, one has to make the difference between the conditional model (CM), which assumes the sources amplitude to be deterministic, and the unconditional model (UM), which assumes the sources amplitude to be Gaussian. These two different models will generally lead to different detection performance, as explained in [SN90b]. There is a wide literature about the GLRT [Kay98; Van68; Sch91; Lev08], its condition of optimality [SF94; ZMZ92], its distribution in some specific cases especially in the large sample regime [Kay98][MJ15][Wil38], its behavior for the CM and UM [SN90b; SN90a].

It is important to keep in mind that in nonlinear estimation problems three distinct regions of operation can be observed (Figure 3.1), namely the a priori region, the threshold region and the asymptotic region [VB07][Ath05][RB74][Ric05][Ren+06]. The a priori region is the performance region where the observations provide little information and the Mean Square Error (MSE) of the MLE is close to that obtained from the prior knowledge about the problem (low number of independent observations and/or low Signal-to-Noise-Ratio (SNR)). The threshold region is a transition region where the MSE of the MLE deteriorates rapidly with respect to the Cramér-Rao bound (CRB). The asymptotic region is the performance region where the MSE of the MLE is small, generally close to the CRB, where the consistency of the MLE can be invoked. The asymptotic region of the MLE generally corresponds to multiple cases: large sample size and/or high-SNR.

In Section 3.5 a GLRT detector is investigated (for a very general form of the conditional signal model) and a special case of this formulation is applied to LCO detection. However, before presenting the general formulation, it is interesting to introduce in Section 3.4 some very simple and well known detectors that can be used for LCO detection (that are based on the simple model presented in the next Section 3.3).

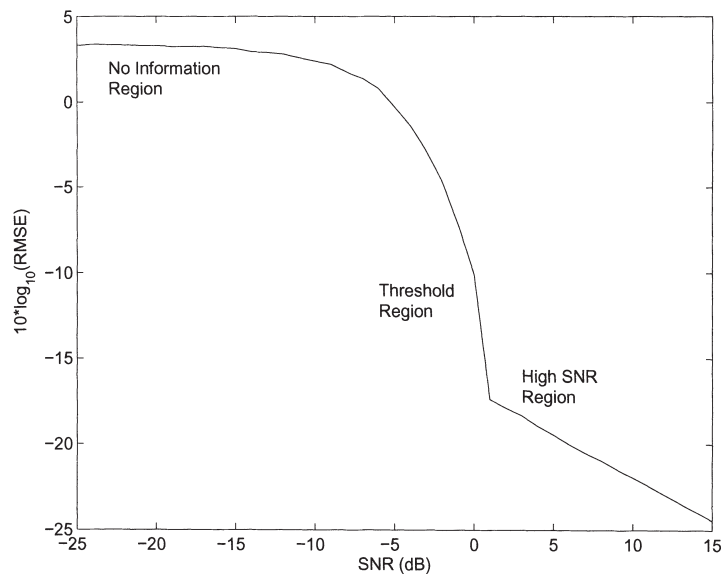


Figure 3.1.: Regions of operations of a nonlinear estimation problem [VB07].

### 3.3. LCO detection

In order to define a suitable model to derive the detector it is important to note that

- The LCO appears as a pure sinusoidal signal at a given frequency (depending on the system dynamic) that can be measured on the flap, twist and control surface rotation of the wing section.
- In the Airbus EFCS architecture we have two signals representing the movement of the control surface: the actuator rod position (measured via a LVDT sensor) and the control surface rotation (measured via a RVDT sensor). Between these signals, the more pertinent for LCO detection is the RVDT.
- The LCO is generally characterized by frequencies higher than the pilot and the control law bandwidth. However, this has to be verified case by case. Indeed, if a periodic signal appears at very low frequency on the control surface, the control law may react to compensate the oscillation.
- The amplitude of the LCO is generally much smaller than the control surface maximum rotation amplitude.
- The limitation of the computational burden of the detector is a priority in order to be compliant with an on-board real-time application.

Considering that the LCO is an additive oscillation on the control surface position measure, we can model the detection problem as in Figure 3.2 where  $\mathbf{x}$  represents the signal from the flight control computers sent to the actuator,  $\mathbf{P}$  the actuator dynamic,  $\mathbf{y}$  the control surface rotation measure,  $\mathbf{w}$  a white Gaussian noise of known variance<sup>1</sup> and  $\mathbf{s}$  the anomaly that we want to detect: the LCO. We assume that  $\mathbf{s}$  does not depend on the input

<sup>1</sup>the noise variance can be derived from flight data

signal  $\mathbf{x}$ .

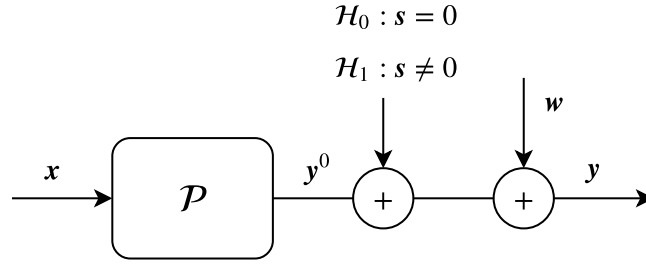


Figure 3.2.: Model of the detection problem.

If there is no signal from the control law ( $\mathbf{x} = \mathbf{0}$ ), the detection problem can be modeled using a binary hypothesis test of the type

$$\mathbf{x} = \mathbf{0} \rightarrow \begin{cases} H_0 : & y(n) = w(n), & w(n) \sim \mathcal{N}(0, \sigma^2) \\ H_1 : & y(n) = s(n) + w(n), & s(n) = A \cos(2\pi f n + \phi) \end{cases} \quad (3.1)$$

where  $n = 0, 1, \dots, N - 1$ . The model in (3.1) is the well known problem of periodic signal detection in Gaussian noise. However, if  $\mathbf{x} \neq \mathbf{0}$ , the detection problem is quite different, because we have to detect a periodic signal contaminated by another signal and Gaussian noise. In this case, the binary hypothesis test can be written

$$\mathbf{x} \neq \mathbf{0} \rightarrow \begin{cases} H_0 : & y(n) = \lambda x(n - p) + w(n) = y^0(n) + w(n), & w(n) \sim \mathcal{N}(0, \sigma^2) \\ H_1 : & y(n) = \lambda x(n - p) + s(n) + w(n) = y^0(n) + s(n) + w(n), & s(n) = A \cos(2\pi f n + \phi) \end{cases} \quad (3.2)$$

where the system  $\mathbf{P}$  in Figure 3.2 has been modeled as a first order system that introduces only a time delay  $p$  and an attenuation/expansion  $\lambda$  on the input signal  $\mathbf{x}$ . On the other hand, the anomaly is modeled as a simple sinusoidal signal with amplitude  $A$ , phase  $\phi$  and frequency  $f$ . Concerning the system model it can be observed that a very rough approximation of  $\mathbf{P}$  is considered in order to limit the number of unknown parameters (computational burden).

### 3.4. Matched filter and GLRT special cases

Starting from the previously presented model 3.2 and as a function of our a priori knowledge on the signal  $\mathbf{y}^0$  and  $\mathbf{s}$ , several very simple detectors can be defined. These detectors are very interesting for their performance, simplicity and low computational cost. For these reasons, they are relevant for the practical application we are considering. These well known results are derived from [Kay98]. For the general formulation of the GLRT and

the scientific contribution of this chapter, the reader may skip this section and go directly to Section 3.5.

### $\mathbf{y}^0$ known and $\mathbf{s}$ known

If the signal  $\mathbf{y}^0$  is known, we can always define a signal  $\mathbf{y}' = \mathbf{y} - \mathbf{y}^0$  and then solve directly the simple problem (3.1). In this section we will use indistinctly  $\mathbf{y}'$  and  $\mathbf{y}$ .

Starting from the two hypotheses  $H_0$  and  $H_1$  in (3.1), if the signal  $\mathbf{s}$  is completely known, the likelihood ratio test (LRT)

$$L(\mathbf{y}) = \frac{p(\mathbf{y}|H_1)}{p(\mathbf{y}|H_0)} \underset{\mathcal{H}_1}{\overset{\mathcal{H}_0}{\gtrless}} \gamma \quad (3.3)$$

leads directly to the following sufficient statistic [Kay98]

$$T(\mathbf{y}) = \sum_{n=0}^{N-1} y(n)s(n) \underset{\mathcal{H}_1}{\overset{\mathcal{H}_0}{\gtrless}} \sigma^2 \ln(\gamma) + \frac{1}{2} \sum_{n=0}^{N-1} s^2(n) = \gamma' \quad (3.4)$$

It is the well-known **matched filter** (see Figure 3.3).

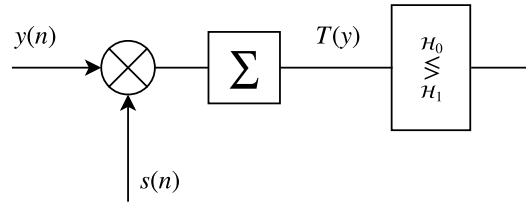


Figure 3.3.: Matched filter for the case of a known signal  $y^0 = \lambda x(n - p)$ .

This detector is characterized by the following false alarm probability  $P_{FA}$  and detection probability  $P_D$

$$P_{FA} = Pr[T > \gamma' | H_0] = Q(\gamma' / \sqrt{\sigma^2 \epsilon}) \quad (3.5)$$

$$P_D = Pr[T > \gamma' | H_1] = Q((\gamma' - \epsilon) / \sqrt{\sigma^2 \epsilon}) \quad (3.6)$$

where  $Q$  is the  $Q$ -function defined as

$$Q(x) = \int_x^{\infty} \frac{1}{\sqrt{2\pi}} e^{-\frac{1}{2}t^2} dt \quad (3.7)$$

and  $\epsilon$  is the mean of the test statistic under the hypothesis  $\mathcal{H}_1$ , i.e.,

$$\epsilon = E(T|H_1) = E\left(\sum_{n=0}^{N-1} (s(n) + w(n))s(n)\right) = \sum_{n=0}^{N-1} s^2(n) \quad (3.8)$$

## $y^0$ known and $s$ partially known

### A unknown

In this case the sufficient statistic becomes [Kay98]:

$$T(\mathbf{y}) = \left( \sum_{n=0}^{N-1} y(n) \cos(2\pi f n + \phi) \right)^2 \underset{\mathcal{H}_1}{\overset{\mathcal{H}_0}{\gtrless}} 2\sigma^2 \ln(\gamma) \sum_{n=0}^{N-1} s^2(n) = \gamma' \quad (3.9)$$

The performance of the detector in Figure 3.4 is

$$P_{FA} = Q_{\chi_1^2}(\gamma') \quad (3.10)$$

$$P_D = Q_{\chi_1^2(\epsilon/\sigma^2)}(\gamma') \quad (3.11)$$

with the assumption  $\epsilon/\sigma^2 \approx NA^2/2\sigma^2$  and where  $Q$  is the complementary cumulative distribution function of a chi-squared random variable [Kay98].

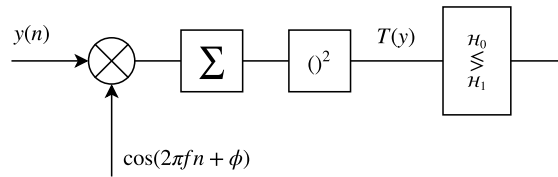


Figure 3.4.: GLRT for an unknown amplitude  $A$ .

### A, $\phi$ unknown

In this case the GLRT is a quadrature matched filter on  $\mathbf{y}$  (see Figure 3.5), which is equivalent to computing the periodogram  $I(f)$  at the known frequency  $f$  (see Figure 3.6). In other terms we decide  $H_1$  if

$$I(f) > \sigma^2 \ln(\gamma) = \gamma' \quad (3.12)$$

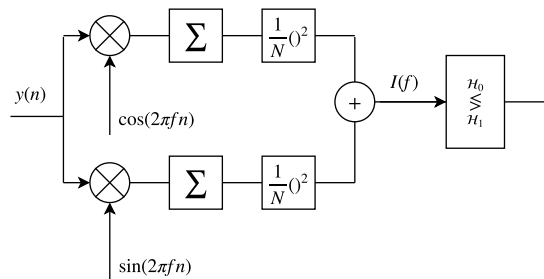
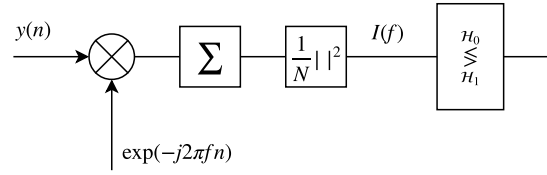


Figure 3.5.: GLRT for  $A, \phi$  unknown: the quadrature matched filter.

Figure 3.6.: GLRT for  $A$ ,  $\phi$  unknown: Periodogram.

This detector is characterized by the following detection performances

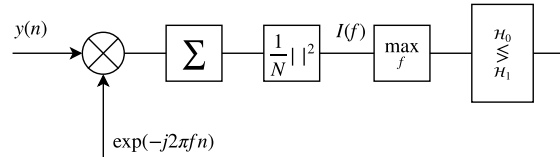
$$P_{FA} = e^{-\frac{\gamma'}{\sigma^2}} \quad (3.13)$$

$$P_D = Q_{\chi^2_2\left(\frac{NA^2}{2\sigma^2}\right)}\left(2\ln\left(\frac{1}{P_{FA}}\right)\right) \quad (3.14)$$

### $A$ , $\phi$ , $f$ unknown

In this case, the GLRT searches for the peaks in the periodogram of  $\mathbf{y}$ , peaks that correspond to the MLE of the frequency  $\hat{f}$  (see Figure 3.7). In other terms we decide  $H_1$  if

$$\max_f I(f) > \sigma^2 \ln(\gamma) = \gamma' \quad (3.15)$$

Figure 3.7.: GLRT for  $A$ ,  $\phi$ ,  $f$  unknown: peaks of the periodogram.

In analogy with the previous one, this detector is characterized by the following detection performances [Kay98]

$$P_{FA} \approx L e^{-\frac{\gamma'}{\sigma^2}} \quad (3.16)$$

$$P_D = Q_{\chi^2_2\left(\frac{NA^2}{2\sigma^2}\right)}\left(2\ln\left(\frac{N/2 - 1}{P_{FA}}\right)\right) \quad (3.17)$$

where  $L$  is the number of tested frequency bins.

### $\mathbf{y}^0$ unknown and $\mathbf{s}$ known

If there are some unknown parameters among  $\lambda$ ,  $p$  and  $\mathbf{s}$ , as already done for case (3.1), a GLR test can be used.

### $\lambda$ , $p$ unknown and $\mathbf{s}$ known

The test can be written as

$$\frac{p(\mathbf{y}, \hat{\theta}_1 | H_1)}{p(\mathbf{y}, \hat{\theta}_0 | H_0)} = \frac{e^{-\frac{1}{2\sigma^2} \sum_{n=0}^{N-1} (y(n) - \lambda_1 x(n - \hat{p}_1) - s(n))^2}}{e^{-\frac{1}{2\sigma^2} \sum_{n=0}^{N-1} (y(n) - \hat{\lambda}_0 x(n - \hat{p}_0))^2}} > \gamma \quad (3.18)$$

where

$$\hat{\theta}_1 = (\hat{\lambda}_1, \hat{p}_1) = \arg \max_{\theta} (p(\mathbf{y}, \theta | H_1))$$

$$\hat{\theta}_0 = (\hat{\lambda}_0, \hat{p}_0) = \arg \max_{\theta} (p(\mathbf{y}, \theta | H_0))$$

it can be shown that  $\hat{\theta}_0$  and  $\hat{\theta}_1$  can be computed as

$$\hat{\lambda}_0 = \frac{\sum_{n=0}^{N-1} y(n) x(n - \hat{p}_0)}{\sum_{n=0}^{N-1} x(n - \hat{p}_0)^2}, \quad \hat{p}_0 = \arg \max_{p_0} \left\{ \frac{\left( \sum_{n=0}^{N-1} y(n) x(n - p_0) \right)^2}{\sum_{n=0}^{N-1} x(n - p_0)^2} \right\}$$

$$\hat{\lambda}_1 = \frac{\sum_{n=0}^{N-1} (y(n) - s(n)) x(n - \hat{p}_1)}{\sum_{n=0}^{N-1} x(n - \hat{p}_1)^2}, \quad \hat{p}_1 = \arg \max_{p_1} \left\{ \frac{\left( \sum_{n=0}^{N-1} (y(n) - s(n)) x(n - p_1) \right)^2}{\sum_{n=0}^{N-1} x(n - p_1)^2} \right\}$$

It is interesting to observe that if  $y(n) \gg s(n)$ , we can consider that  $y(n) - s(n) \approx y(n)$  and thus  $\hat{p}_1 = \hat{p}_0 = \hat{p}$  and  $\hat{\lambda}_1 = \hat{\lambda}_0 = \hat{\lambda}$ . In this case, the estimation of  $\lambda$  and  $p$  and the detection of  $\mathbf{s}$  can be decoupled. The LCO detector in (3.18) is simply the combination of an estimator of  $\lambda$  and  $p$  and a matched filter on the residuals between  $y$  and  $y^0$  (see Figure 3.8).

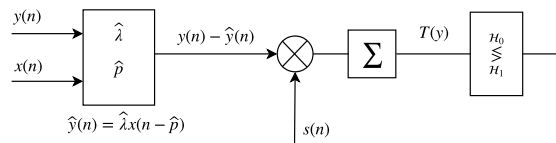


Figure 3.8.: Detector for  $\lambda$  and  $p$  unknown: estimation of  $\lambda$  and  $p$  + matched filter (between  $s$  and the residuals  $y - y^0$ )

### $y^0$ unknown and $\mathbf{s}$ partially unknown

If  $(\lambda, p)$  and some parameters of  $\mathbf{s}$  are unknown, the detection problem is more difficult. This is the case of interest for real applications. Different approaches have been considered for its resolution.

## Decoupled approach

If we consider that the estimation of  $\lambda$  and  $p$  and the detection of  $\mathbf{s}$  can be decoupled, an approach similar to CLEAN algorithm [TS88] can be used to tackle the problem<sup>2</sup>. In figure 3.9 we can see an example of detector for  $\lambda$ ,  $p$ ,  $A$  and  $\phi$  unknown.

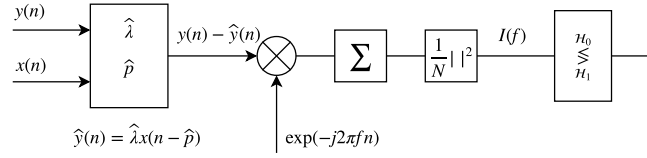


Figure 3.9.: Example of detector for  $\lambda$ ,  $p$ ,  $A$  and  $\phi$  unknown: estimation of  $\lambda$  and  $p$  + periodogram of the residuals  $y - y^0$

## Joint Detection and Estimation

If we consider that the estimation of  $\lambda$  and  $p$  and the detection of  $\mathbf{s}$  cannot be decoupled, a joint estimation and detection problem has to be solved. In the next section we will see more in details how one can approach this problem.

### 3.5. Deterministic signal detection in interference

Detecting a deterministic signal corrupted by an additive deterministic interference and additive noise of known power can be written as the following binary hypothesis test

$$\begin{cases} H_0 : \mathbf{y} = \mathbf{i} + \mathbf{w} \\ H_1 : \mathbf{y} = \mathbf{i} + \mathbf{s} + \mathbf{w} \end{cases} \quad (3.19)$$

where  $\mathbf{w}$  is a white Gaussian noise (whose variance  $\sigma^2$  is known),  $\mathbf{s}$  is the deterministic signal that we want to detect and  $\mathbf{i}$  is the interference. Considering the conditional observation model for (3.19), we obtain

$$\begin{cases} \mathcal{H}_0 : \mathbf{y} = \mathbf{H}_0(\boldsymbol{\alpha}_0)\boldsymbol{\beta}_0 + \mathbf{w} \\ \mathcal{H}_1 : \mathbf{y} = \underbrace{[\mathbf{H}_0(\boldsymbol{\alpha}_0) \quad \mathbf{H}_s(\boldsymbol{\alpha}_s)]}_{\mathbf{H}_1(\boldsymbol{\alpha}_1)} \underbrace{\begin{bmatrix} \boldsymbol{\beta}_0 \\ \boldsymbol{\beta}_s \end{bmatrix}}_{\boldsymbol{\beta}_1} + \mathbf{w} \end{cases} \quad (3.20)$$

<sup>2</sup>CLEAN algorithm assumes that there are weak signal sources in the presence of strong signal sources that are well estimated (hence sufficiently “orthogonal”). In this case, we can subtract the well estimated sources from the mixture in order to better estimate the weak sources. This avoids doing a multi-source MLE. In our case, we should assume that  $\|\mathbf{s}\|^2 \ll \lambda^2 \|\mathbf{x}\|^2$ .

where  $\mathbf{y} \in \mathbb{R}^N$  is the vector of observations,  $\mathbf{w} = [w(1), \dots, w(N)]^T \sim \mathcal{N}(0, \sigma^2 \mathbf{I}_N)$  is a noise vector of Gaussian distribution with known variance  $\sigma^2$  and  $\mathbf{H}_0(\boldsymbol{\alpha}_0) \in \mathbb{R}^{N \times m_0}$ ,  $\mathbf{H}_1(\boldsymbol{\alpha}_1) \in \mathbb{R}^{N \times m_1}$  are two nested observation matrices that depend on the unknown parameter vectors  $\boldsymbol{\alpha}_0 \in \mathbb{R}^{n_0}$  and  $\boldsymbol{\alpha}_1 \in \mathbb{R}^{n_1}$ . The interference and signal terms have been expressed as  $\mathbf{i} = \mathbf{H}_0(\boldsymbol{\alpha}_0)\boldsymbol{\beta}_0$  and  $\mathbf{s} = \mathbf{H}_s(\boldsymbol{\alpha}_s)\boldsymbol{\beta}_s$ . By definition of “conditional observation model” [SN90b], we mean that all the unknown parameter vectors  $\boldsymbol{\beta}_0 \in \mathbb{R}^{m_0}$ ,  $\boldsymbol{\alpha}_0 \in \mathbb{R}^{n_0}$ ,  $\boldsymbol{\beta}_1 \in \mathbb{R}^{m_1}$  and  $\boldsymbol{\alpha}_1 \in \mathbb{R}^{n_1}$  are deterministic. Note that the detection problem under consideration (3.20) is more general than the **classical linear model** studied in [Kay98, Theorem 7.1], where the same known observation matrix is considered for the two hypotheses and where the unknown parameter vector  $\beta_1$  is related to  $\beta_0$ . Thus, the test statistics of the detection problem (3.20) will differ from the one derived in [Kay98]. We will see how the detection problem (3.20) can be used for LCO detection in Section 3.7 and 3.8. The GLRT requires to estimate the unknown parameter vectors  $\boldsymbol{\alpha}$  and  $\boldsymbol{\beta}$  under both hypotheses (i.e., for  $i = 0, 1$ ) using the maximum likelihood principle. Considering the hypothesis of additive white Gaussian noise of known variance<sup>3</sup>  $\sigma^2$ , i.e.  $w(n) \sim \mathcal{N}(0, \sigma^2)$ , we have

$$p(\mathbf{y}; \boldsymbol{\alpha}, \boldsymbol{\beta}) = \frac{1}{(2\pi\sigma^2)^{\frac{N}{2}}} \exp\left(-\frac{1}{2\sigma^2} \|\mathbf{y} - \mathbf{H}(\boldsymbol{\alpha})\boldsymbol{\beta}\|^2\right).$$

The GLRT for the detection problem (3.20) can be written as

$$\frac{p(\mathbf{y}; \hat{\boldsymbol{\alpha}}_1, \hat{\boldsymbol{\beta}}_1 | \mathcal{H}_1)}{p(\mathbf{y}; \hat{\boldsymbol{\alpha}}_0, \hat{\boldsymbol{\beta}}_0 | \mathcal{H}_0)} = \frac{\exp\left(-\frac{1}{2\sigma^2} \|\mathbf{y} - \mathbf{H}_1(\hat{\boldsymbol{\alpha}}_1)\hat{\boldsymbol{\beta}}_1\|^2\right)}{\exp\left(-\frac{1}{2\sigma^2} \|\mathbf{y} - \mathbf{H}_0(\hat{\boldsymbol{\alpha}}_0)\hat{\boldsymbol{\beta}}_0\|^2\right)} \underset{\mathcal{H}_1}{\overset{\mathcal{H}_0}{\lesseqgtr}} \gamma' \quad (3.21)$$

where  $\gamma'$  is a constant threshold. The estimation problem, considering a general notation that is true for both hypotheses  $\mathcal{H}_0$  and  $\mathcal{H}_1$ , reduces to the minimization of the following least squares (LS) criterion [Kay93]

$$\mathbf{J}(\boldsymbol{\alpha}, \boldsymbol{\beta}) = \|\mathbf{y} - \mathbf{H}(\boldsymbol{\alpha})\boldsymbol{\beta}\|^2 = (\mathbf{y} - \mathbf{H}(\boldsymbol{\alpha})\boldsymbol{\beta})^T (\mathbf{y} - \mathbf{H}(\boldsymbol{\alpha})\boldsymbol{\beta}).$$

Introducing the orthogonal projection matrix  $\boldsymbol{\Pi}_{\mathbf{H}(\boldsymbol{\alpha})} = \mathbf{H}(\boldsymbol{\alpha})(\mathbf{H}(\boldsymbol{\alpha})^T \mathbf{H}(\boldsymbol{\alpha}))^{-1} \mathbf{H}(\boldsymbol{\alpha})^T$ , that projects a vector onto the columns of  $\mathbf{H}(\boldsymbol{\alpha})$ , and  $\boldsymbol{\Pi}_{\mathbf{H}(\boldsymbol{\alpha})}^\perp = \mathbf{I} - \boldsymbol{\Pi}_{\mathbf{H}(\boldsymbol{\alpha})}$ , that projects a vector onto the space orthogonal to the columns of  $\mathbf{H}(\boldsymbol{\alpha})$ , the LS criterion can be rewritten as

$$\begin{aligned} \mathbf{J}(\boldsymbol{\alpha}, \boldsymbol{\beta}) &= \|\mathbf{y} - \mathbf{H}(\boldsymbol{\alpha})\boldsymbol{\beta}\|^2 \\ &= \|\boldsymbol{\Pi}_{\mathbf{H}(\boldsymbol{\alpha})}(\mathbf{y} - \mathbf{H}(\boldsymbol{\alpha})\boldsymbol{\beta})\|^2 + \|\boldsymbol{\Pi}_{\mathbf{H}(\boldsymbol{\alpha})}^\perp(\mathbf{y} - \mathbf{H}(\boldsymbol{\alpha})\boldsymbol{\beta})\|^2 \\ &= \left\| \mathbf{H}(\boldsymbol{\alpha})[(\mathbf{H}^T(\boldsymbol{\alpha})\mathbf{H}(\boldsymbol{\alpha}))^{-1} \mathbf{H}^T(\boldsymbol{\alpha})\mathbf{y} - \boldsymbol{\beta}] \right\|^2 + \left\| \boldsymbol{\Pi}_{\mathbf{H}(\boldsymbol{\alpha})}^\perp \mathbf{y} \right\|^2. \end{aligned}$$

<sup>3</sup>This study has been motivated by a real aeronautical application where the noise variance can be determined using signals that are not affected by any anomaly.

The value of  $\boldsymbol{\beta}$  that minimizes  $\mathbf{J}(\boldsymbol{\alpha}, \boldsymbol{\beta})$  for a given value of  $\boldsymbol{\alpha}$  is thus classically obtained as

$$\boldsymbol{\beta} = (\mathbf{H}^T(\boldsymbol{\alpha})\mathbf{H}(\boldsymbol{\alpha}))^{-1}\mathbf{H}^T(\boldsymbol{\alpha})\mathbf{y} \quad (3.22)$$

that corresponds to the classical unconstrained LS estimator of  $\boldsymbol{\beta}$  for a known vector  $\boldsymbol{\alpha}$ . The MLE of  $\boldsymbol{\alpha}$  is then obtained as the solution of the following optimization problem

$$\hat{\boldsymbol{\alpha}} = \underset{\boldsymbol{\alpha}}{\operatorname{argmin}} \left\| \boldsymbol{\Pi}_{\mathbf{H}(\boldsymbol{\alpha})}^{\perp} \mathbf{y} \right\|^2 = \underset{\boldsymbol{\alpha}}{\operatorname{argmax}} \left\| \boldsymbol{\Pi}_{\mathbf{H}(\boldsymbol{\alpha})} \mathbf{y} \right\|^2 \quad (3.23)$$

where we have used the properties of projection matrices<sup>4</sup>. Of course, there is no analytical solution for the MLE of  $\boldsymbol{\alpha}$  in the general case. However, this MLE can be obtained numerically using for example a grid search approach (in general via a multivariate optimization problem). Once the MLE of  $\boldsymbol{\alpha}$  (denoted as  $\hat{\boldsymbol{\alpha}}$ ) has been determined,  $\boldsymbol{\beta}$  can be estimated as

$$\hat{\boldsymbol{\beta}} = (\mathbf{H}^T(\hat{\boldsymbol{\alpha}})\mathbf{H}(\hat{\boldsymbol{\alpha}}))^{-1}\mathbf{H}^T(\hat{\boldsymbol{\alpha}})\mathbf{y}. \quad (3.24)$$

From the expressions of the MLEs (3.23) and (3.24), the GLRT sufficient statistic  $\mathbf{T}$  can be written as

$$T = \frac{1}{2\sigma^2} \left( \left\| \mathbf{y} - \mathbf{H}_0(\hat{\boldsymbol{\alpha}}_0)\hat{\boldsymbol{\beta}}_0 \right\|^2 - \left\| \mathbf{y} - \mathbf{H}_1(\hat{\boldsymbol{\alpha}}_1)\hat{\boldsymbol{\beta}}_1 \right\|^2 \right) \quad (3.25)$$

$$= \frac{1}{2\sigma^2} \left( \left\| \boldsymbol{\Pi}_{\mathbf{H}_0(\hat{\boldsymbol{\alpha}}_0)}^{\perp} \mathbf{y} \right\|^2 - \left\| \boldsymbol{\Pi}_{\mathbf{H}_1(\hat{\boldsymbol{\alpha}}_1)}^{\perp} \mathbf{y} \right\|^2 \right) \quad (3.26)$$

or considering that  $\boldsymbol{\Pi}_{\mathbf{H}}^{\perp}(\boldsymbol{\alpha}) = \mathbf{I} - \boldsymbol{\Pi}_{\mathbf{H}}(\boldsymbol{\alpha})$ , we obtain the following equivalent detector

$$T = \frac{1}{2\sigma^2} \left( \left\| \boldsymbol{\Pi}_{\mathbf{H}_1(\hat{\boldsymbol{\alpha}}_1)} \mathbf{y} \right\|^2 - \left\| \boldsymbol{\Pi}_{\mathbf{H}_0(\hat{\boldsymbol{\alpha}}_0)} \mathbf{y} \right\|^2 \right) \underset{\mathcal{H}_1}{\overset{\mathcal{H}_0}{\gtrless}} \gamma'' \quad (3.27)$$

or

$$T' = \frac{1}{\sigma^2} \left( \left\| \boldsymbol{\Pi}_{\mathbf{H}_1(\hat{\boldsymbol{\alpha}}_1)} \mathbf{y} \right\|^2 - \left\| \boldsymbol{\Pi}_{\mathbf{H}_0(\hat{\boldsymbol{\alpha}}_0)} \mathbf{y} \right\|^2 \right) \underset{\mathcal{H}_1}{\overset{\mathcal{H}_0}{\gtrless}} \gamma$$

where  $\gamma'' = \log(\gamma')$  and  $\gamma = 2\gamma''$ . It is important to note that the numerator of the test statistics in (3.21) is computed by assuming the hypothesis  $\mathcal{H}_1$  is true, whether the denominator is computed by assuming the hypothesis  $\mathcal{H}_0$  is true. **Even if the two hypotheses are never true simultaneously, the principle of the GLRT is to compare the ratio of the estimated densities of the observations under both hypotheses.** Unfortunately, the detection performance of the GLRT (3.27) is difficult to be studied in the

<sup>4</sup> $\boldsymbol{\Pi}$  is symmetric ( $\boldsymbol{\Pi}^T = \boldsymbol{\Pi}$ ) and idempotent ( $\boldsymbol{\Pi}^2 = \boldsymbol{\Pi}$ )

general case. For this reason, we have decided to investigate another test, that we will call “approximate GLRT”, for which the performance can be computed exactly and that, under some particular assumptions, behaves almost like the GLRT (3.21) under both hypotheses  $\mathcal{H}_0$  and  $\mathcal{H}_1$ .

### 3.6. Approximate GLRT

The GLRT can be rewritten as

$$T_{\text{GLRT}} = \frac{\sup_{\alpha_1} \exp\left(-\frac{1}{2\sigma^2} \left\| \mathbf{\Pi}_{\mathbf{H}_1(\alpha_1)}^\perp \mathbf{y} \right\|^2\right)}{\sup_{\alpha_0} \exp\left(-\frac{1}{2\sigma^2} \left\| \mathbf{\Pi}_{\mathbf{H}_0(\alpha_0)}^\perp \mathbf{y} \right\|^2\right)} \underset{\mathcal{H}_1}{\overset{\mathcal{H}_0}{\gtrless}} \gamma \quad (3.28)$$

or equivalently

$$T_{\text{GLRT}} = \frac{\exp\left(-\frac{1}{2\sigma^2} \left\| \mathbf{\Pi}_{\mathbf{H}_1(\hat{\alpha}_1)}^\perp \mathbf{y} \right\|^2\right)}{\exp\left(-\frac{1}{2\sigma^2} \left\| \mathbf{\Pi}_{\mathbf{H}_0(\hat{\alpha}_0)}^\perp \mathbf{y} \right\|^2\right)} \underset{\mathcal{H}_1}{\overset{\mathcal{H}_0}{\gtrless}} \gamma. \quad (3.29)$$

Under each hypothesis ( $\mathcal{H}_0$  or  $\mathcal{H}_1$ ), one can invoke the consistency and asymptotic efficiency of the conditional MLE for high signal to noise ratio (SNR) [Ren+06] and using a Taylor expansion around the true value of  $\alpha$ , it can be shown (see Appendix A.1) that one can consider the following approximation (considering a general notation for the two hypotheses)

$$\left\| \mathbf{\Pi}_{\mathbf{H}(\alpha + \widehat{d\alpha})}^\perp \mathbf{y} \right\|^2 \approx \left\| \mathbf{\Pi}_{\mathbf{D}}^\perp \mathbf{\Pi}_{\mathbf{H}(\alpha)}^\perp \mathbf{y} \right\|^2 + \left\| \mathbf{\Pi}_{\mathbf{D}} \mathbf{\Pi}_{\mathbf{H}(\alpha)}^\perp \mathbf{y} - \mathbf{D} \widehat{d\alpha} \right\|^2 \quad (3.30)$$

where  $\widehat{d\alpha} = \hat{\alpha} - \alpha$  and  $\mathbf{D} = \mathbf{\Pi}_{\mathbf{H}(\alpha)}^\perp \frac{\partial \mathbf{H}(\alpha) \beta}{\partial \alpha}$ . (3.30) leads to the following expression of the approximate GLRT

$$\widehat{T}_{\text{GLRT}} = \frac{\exp\left(-\frac{1}{2\sigma^2} \left\| \mathbf{\Pi}_{\mathbf{D}_1}^\perp \mathbf{\Pi}_{\mathbf{H}_1(\alpha_1)}^\perp \mathbf{y} \right\|^2 - \frac{1}{2\sigma^2} \left\| \mathbf{\Pi}_{\mathbf{D}_1} \mathbf{\Pi}_{\mathbf{H}_1(\alpha_1)}^\perp \mathbf{y} - \mathbf{D}_1 \widehat{d\alpha}_1 \right\|^2\right)}{\exp\left(-\frac{1}{2\sigma^2} \left\| \mathbf{\Pi}_{\mathbf{D}_0}^\perp \mathbf{\Pi}_{\mathbf{H}_0(\alpha_0)}^\perp \mathbf{y} \right\|^2 - \frac{1}{2\sigma^2} \left\| \mathbf{\Pi}_{\mathbf{D}_0} \mathbf{\Pi}_{\mathbf{H}_0(\alpha_0)}^\perp \mathbf{y} - \mathbf{D}_0 \widehat{d\alpha}_0 \right\|^2\right)} \underset{\mathcal{H}_1}{\overset{\mathcal{H}_0}{\gtrless}} \gamma.$$

Since by hypothesis the MLE of  $\alpha$  satisfies

$$\mathbf{\Pi}_{\mathbf{D}} \mathbf{\Pi}_{\mathbf{H}(\alpha)}^\perp \mathbf{y} = \mathbf{D} \widehat{d\alpha} \Leftrightarrow \widehat{d\alpha} = (\mathbf{D}^T \mathbf{D})^{-1} \mathbf{D}^T \mathbf{\Pi}_{\mathbf{H}(\alpha)}^\perp \mathbf{y},$$

hence

$$\widehat{T}_{\text{GLRT}} = \frac{\exp\left(-\frac{1}{2\sigma^2} \left\| \mathbf{\Pi}_{\mathcal{D}_1}^\perp \mathbf{\Pi}_{\mathcal{H}_1(\boldsymbol{\alpha}_1)}^\perp \mathbf{y} \right\|^2\right)}{\exp\left(-\frac{1}{2\sigma^2} \left\| \mathbf{\Pi}_{\mathcal{D}_0}^\perp \mathbf{\Pi}_{\mathcal{H}_0(\boldsymbol{\alpha}_0)}^\perp \mathbf{y} \right\|^2\right)} \underset{\mathcal{H}_1}{\overset{\mathcal{H}_0}{\gtrless}} \gamma \quad (3.31)$$

or equivalently

$$\widehat{T}_{\text{GLRT}} = \frac{\exp\left(-\frac{1}{2\sigma^2} \mathbf{y}^T \mathbf{L}_1^\perp \mathbf{y}\right)}{\exp\left(-\frac{1}{2\sigma^2} \mathbf{y}^T \mathbf{L}_0^\perp \mathbf{y}\right)} \underset{\mathcal{H}_1}{\overset{\mathcal{H}_0}{\gtrless}} \gamma' \quad (3.32)$$

where

$$\mathbf{L}_0^\perp = \mathbf{\Pi}_{\mathcal{H}_0(\boldsymbol{\alpha}_0)}^\perp \mathbf{\Pi}_{\mathcal{D}_0}^\perp \mathbf{\Pi}_{\mathcal{H}_0(\boldsymbol{\alpha}_0)}^\perp, \quad \mathbf{L}_1^\perp = \mathbf{\Pi}_{\mathcal{H}_1(\boldsymbol{\alpha}_1)}^\perp \mathbf{\Pi}_{\mathcal{D}_1}^\perp \mathbf{\Pi}_{\mathcal{H}_1(\boldsymbol{\alpha}_1)}^\perp.$$

The approximate detector (3.32) cannot be implemented (contrary to the GLRT (3.28)) as it depends on  $\boldsymbol{\alpha}$ .

However, its performance can be computed exactly as detailed in Section 3.7.

In real applications (LCO detection in the Airbus EFCS) we generally have some a priori information about the parameters  $\boldsymbol{\alpha}$ . Thus, we can evaluate the MLE (3.23) using a grid search approach only on a subset of values belonging to an interval  $]\boldsymbol{\alpha}_{min}, \boldsymbol{\alpha}_{max}[$  resulting from this prior information. Defining a relatively small grid around a first guess value  $\boldsymbol{\alpha}^0$  (that is a priori known based on the considered control surface) we are able to implement the GLRT defined in (3.28). Under this particular assumption, we have empirically verified that the approximate GLRT behaves almost like the GLRT under both the hypotheses  $\mathcal{H}_0$  and  $\mathcal{H}_1$ . Figure 3.10 compares the empirical distributions of the GLRT and the approximate GLRT for a specific test case (described in Section 3.8).

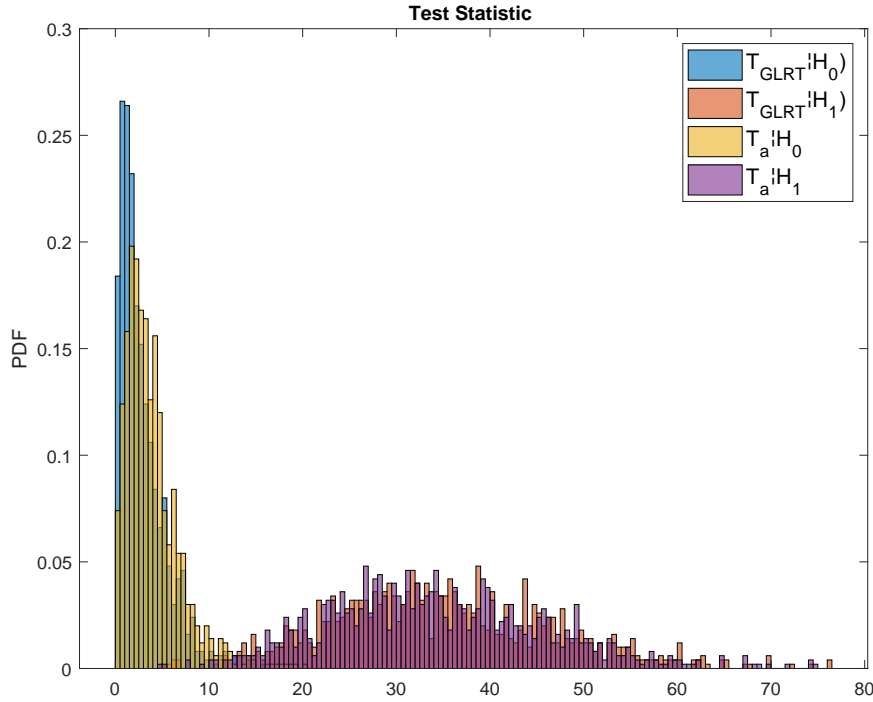


Figure 3.10.: Comparison of the empirical distributions of the GLRT ( $T_{GLRT}$ ) and the approximate GLRT ( $T_a$ ) under the hypotheses  $\mathcal{H}_0$  and  $\mathcal{H}_1$  for the test case described in Section 3.8.

We can observe that the distributions of the test statistics under both hypotheses are very similar as the corresponding histograms are superimposed. Thus, the exact asymptotic performance that can be derived for (3.32) (see Section 3.7) can be used as a reference for (3.28).

### 3.7. Detection performance

#### $\beta$ and $\alpha$ unknown

In the general case where the parameter vectors  $\alpha_0$  and  $\alpha_1$  are unknown, it is not possible to obtain a simple analytic expression of the GLRT performance for all regions of operations of the MLEs. However, a reference can be derived in the asymptotic region, where we can write the approximate GLRT sufficient statistic as

$$\begin{aligned} & \frac{1}{\sigma^2} \mathbf{y}^T \left[ \Pi_{\mathbf{H}_0(\alpha_0)}^\perp \Pi_{\mathbf{D}_0}^\perp \Pi_{\mathbf{H}_0(\alpha_0)}^\perp - \Pi_{\mathbf{H}_1(\alpha_1)}^\perp \Pi_{\mathbf{D}_1}^\perp \Pi_{\mathbf{H}_1(\alpha_1)}^\perp \right] \mathbf{y} \\ &= \frac{1}{\sigma^2} \mathbf{y}^T \mathbf{K}_a \mathbf{y} \end{aligned}$$

where  $\mathbf{K}_a = \mathbf{L}_0^\perp - \mathbf{L}_1^\perp$ . The particular relationship between the observation matrices (nested model) leads to a matrix  $\mathbf{K}_a$  which is a projection (see Appendix A.3). Moreover, since  $\mathbf{K}_a$  is symmetric,  $\mathbf{K}_a$  is the matrix of an orthogonal projection whose eigenvalues are  $\{0, 1\}$ . As a consequence, the distribution of  $T'$  is a chi-square

distribution [Mui09, Theorem 1.4.5] and the detection performance can be expressed as <sup>5</sup>

$$\begin{aligned} P_{\text{FA}} &= P(T' > \gamma | H_0) = P(\chi_r^2 > \gamma) = Q_{\chi_r^2}(\gamma) \\ P_D &= P(T' > \gamma | H_1) = P(\chi_r^2(k) > \gamma) = Q_{\chi_r^2(k)}(\gamma) \end{aligned} \quad (3.33)$$

where the degree of freedom of the chi-square distribution is

$$r_a = \text{rank}(\mathbf{K}_a) \quad (3.34)$$

and its non-centrality parameter is

$$k_a = \frac{\boldsymbol{\beta}_1^T \mathbf{H}_1^T(\boldsymbol{\alpha}_1) \mathbf{L}_0^\perp \mathbf{H}_1(\boldsymbol{\alpha}_1) \boldsymbol{\beta}_1}{\sigma^2}. \quad (3.35)$$

The functions  $Q_{\chi_r^2}$  and  $Q_{\chi_r^2(k)}$  are the complementary cumulative distribution functions of central and non central chi-square distributions, whose closed-form expressions can be found for example in [Kay98, Chap. 2].

### $\boldsymbol{\beta}$ unknown and $\boldsymbol{\alpha}$ known

If  $\boldsymbol{\alpha}$  is known, an exact expression of the GLRT performance is obtained for all regions of operations of the MLE<sup>6</sup>. Indeed, if  $\boldsymbol{\beta}$  is unknown and  $\boldsymbol{\alpha}$  is known, we can express the sufficient statistic as

$$T' = \frac{1}{\sigma^2} \left( \left\| \boldsymbol{\Pi}_{\mathbf{H}_0(\boldsymbol{\alpha}_0)}^\perp \mathbf{y} \right\|^2 - \left\| \boldsymbol{\Pi}_{\mathbf{H}_1(\boldsymbol{\alpha}_1)}^\perp \mathbf{y} \right\|^2 \right)$$

or equivalently

$$T' = \frac{1}{\sigma^2} \mathbf{y}^T \left[ \boldsymbol{\Pi}_{\mathbf{H}_0(\boldsymbol{\alpha}_0)}^\perp - \boldsymbol{\Pi}_{\mathbf{H}_1(\boldsymbol{\alpha}_1)}^\perp \right] \mathbf{y} = \frac{1}{\sigma^2} \mathbf{y}^T \mathbf{K} \mathbf{y}.$$

Since it is easy to prove that

$$\mathbf{K} = \boldsymbol{\Pi}_{\mathbf{H}_0(\boldsymbol{\alpha}_0)}^\perp - \boldsymbol{\Pi}_{\mathbf{H}_1(\boldsymbol{\alpha}_1)}^\perp = \boldsymbol{\Pi}_{\boldsymbol{\Pi}_{\mathbf{H}_0}^\perp \mathbf{H}_s}$$

<sup>5</sup>A quadratic form of the type  $\mathbf{x}^T \boldsymbol{\Pi} \mathbf{x}$ , where  $\mathbf{x} \sim \mathcal{N}(\boldsymbol{\mu}, \boldsymbol{\Sigma})$  and  $\boldsymbol{\Pi}$  is a symmetric and idempotent matrix, is  $\chi_k^2(\delta)$ , where  $k = \text{rank}(\boldsymbol{\Pi})$  and  $\delta = \boldsymbol{\mu}^T \boldsymbol{\Pi} \boldsymbol{\mu}$ .

<sup>6</sup>i.e., the a priori region, the threshold region and the asymptotic region [Ath05].

is symmetric and idempotent (see Appendix A.3), the detection performance can be computed as in (3.33) where  $r$  is the rank of  $\mathbf{K}$

$$r = \text{rank}(\mathbf{K}) = \text{rank}(\mathbf{H}_1) - \text{rank}(\mathbf{H}_0) = \text{rank}(\mathbf{H}_s) \quad (3.36)$$

and the non centrality parameter is

$$\begin{aligned} k &= \frac{\beta_1^T \mathbf{H}_1^T(\alpha_1) \left[ \Pi_{\mathbf{H}_0(\alpha_0)}^\perp - \Pi_{\mathbf{H}_1(\alpha_1)}^\perp \right] \mathbf{H}_1(\alpha_1) \beta_1}{\sigma^2} \\ &= \frac{\beta_1^T \mathbf{H}_1^T(\alpha_1) \Pi_{\mathbf{H}_0(\alpha_0)}^\perp \mathbf{H}_1(\alpha_1) \beta_1}{\sigma^2}. \end{aligned} \quad (3.37)$$

Section 3.8 studies the interesting problem of detecting a deterministic sinusoidal signal embedded in a deterministic interference (for a known noise level), which can be formulated as (3.20).

#### Remark

It is interesting to observe that for this particular case, the same results in terms of detection performance can be obtained using Theorem 7.1 of [Kay98]. Indeed, following the notations in [Kay98], one can simply choose  $\mathbf{H} = [\mathbf{H}_0(\alpha_0); \mathbf{H}_s(\alpha_s)]$ ,  $\boldsymbol{\theta} = [\beta_0^T; \beta_s^T]$ ,  $\mathbf{A} = [\mathbf{0}_{m_s \times m_0}; I_{m_s}]$ ,  $\mathbf{b} = \mathbf{0}$  and after some calculations one can obtain

$$\begin{aligned} T\sigma^2 &= \hat{\beta}_1^T \mathbf{A}^T (\mathbf{A}(\mathbf{H}^T \mathbf{H})^{-1} \mathbf{A}^T)^{-1} \mathbf{A} \hat{\beta}_1 = \mathbf{y}^T \Pi_{\Pi_{\mathbf{H}_0}^\perp} \mathbf{H}_s \mathbf{y} \\ &= \mathbf{y}^T \Pi_{\mathbf{H}_1} \mathbf{y} - \mathbf{y}^T \Pi_{\mathbf{H}_0} \mathbf{y}. \end{aligned}$$

Unfortunately the case of an unknown vector  $\boldsymbol{\alpha}$  is not covered by the theorem.

### 3.8. Sinusoidal signal detection in deterministic interference

This section considers the following problem

$$\begin{cases} \mathcal{H}_0 : y(nT_s) &= \lambda x(nT_s - p) + w(nT_s) \\ \mathcal{H}_1 : y(nT_s) &= \lambda x(nT_s - p) + l_1 \cos(2\pi f nT_s) + l_2 \sin(2\pi f nT_s) + w(nT_s) \end{cases} \quad (3.38)$$

where  $n = 0, 1, \dots, N - 1$  and  $T_s$  is the sampling time. This problem is equivalent to (3.20) with the following unknown parameter vectors  $\boldsymbol{\alpha}_0 = [p] \in \mathbb{R}$ ,  $\boldsymbol{\beta}_0 = [\lambda] \in \mathbb{R}$ ,  $\boldsymbol{\alpha}_1 = [p, f]^T \in \mathbb{R}^2$ ,  $\boldsymbol{\beta}_1 = [\lambda, l_1, l_2]^T \in \mathbb{R}^3$  and the

observation matrices

$$\mathbf{H}_0(\boldsymbol{\alpha}_0) = [\mathbf{x}(p)] = \begin{pmatrix} x(-p) \\ x(T_s - p) \\ \vdots \\ x((N-1)T_s - p) \end{pmatrix}$$

$$\mathbf{H}_1(\boldsymbol{\alpha}_1) = [\mathbf{x}(p), \mathbf{c}(f), \mathbf{s}(f)] = \begin{bmatrix} x(-p) & 1 & 0 \\ x(T_s - p) & \cos(2\pi f T_s) & \sin(2\pi f T_s) \\ \vdots & \vdots & \vdots \\ x((N-1)T_s - p) & \cos(2\pi f (N-1)T_s) & \sin(2\pi f (N-1)T_s) \end{bmatrix}$$

The signal to detect  $\mathbf{s}$  is a classical sinusoidal signal of the type  $A \cos(2\pi f n T_s + \phi)$  that can be decomposed as

$$s(nT_s) = l_1 \cos(2\pi f n T_s) + l_2 \sin(2\pi f n T_s) \quad (3.39)$$

allowing the non-linear dependency with respect to  $\phi$  to be removed. In this case  $A = \sqrt{l_1^2 + l_2^2}$  and  $\phi = \arctan(\frac{-l_2}{l_1})$ . On the other hand, the interference  $\mathbf{i}$  is a function of the known signal  $\mathbf{x}$  and of the unknown parameters  $\lambda$  and  $p$ . It is interesting to observe that this very simple model can be used for the detection of spurious sinusoidal signals possibly affecting the output of a system P<sup>7</sup>, as illustrated in Fig. 3.2.

### 3.8.1. Maximum Likelihood Estimators and Test Statistic

The MLEs and the test statistic for this particular case directly result from (3.24), (3.23) and (3.27), leading to (3.40), (3.41), (3.42), (3.43) and (3.44),

$$\hat{\boldsymbol{\alpha}}_0 = \hat{p}_0 = \underset{p}{\operatorname{argmax}} (\mathbf{y}^T \mathbf{H}_0(\boldsymbol{\alpha}_0) (\mathbf{H}_0^T(\boldsymbol{\alpha}_0) \mathbf{H}_0(\boldsymbol{\alpha}_0))^{-1} \mathbf{H}_0^T(\boldsymbol{\alpha}_0) \mathbf{y}) = \underset{p}{\operatorname{argmax}} \left( \frac{(\mathbf{x}^T(p) \mathbf{y})^2}{\mathbf{x}^T(p) \mathbf{x}(p)} \right) \quad (3.40)$$

$$\hat{\boldsymbol{\beta}}_0 = \hat{\lambda}_0 = (\mathbf{H}_0^T(\hat{\boldsymbol{\alpha}}_0) \mathbf{H}_0(\hat{\boldsymbol{\alpha}}_0))^{-1} \mathbf{H}_0^T(\hat{\boldsymbol{\alpha}}_0) \mathbf{y} = \frac{\mathbf{x}^T(\hat{p}_0) \mathbf{y}}{\mathbf{x}^T(\hat{p}_0) \mathbf{x}(\hat{p}_0)} \quad (3.41)$$

<sup>7</sup>The system P can be approximated by a delay  $p \in \mathbb{R}$  and an attenuation/amplification effect  $\lambda \in \mathbb{R}$  applied to a known signal  $x$

$$\hat{\boldsymbol{\alpha}}_1 = \begin{pmatrix} \hat{p}_1 \\ \hat{f} \end{pmatrix} = \underset{p,f}{\operatorname{argmax}} (\mathbf{y}^T \mathbf{H}_1(\boldsymbol{\alpha}_1) (\mathbf{H}_1^T(\boldsymbol{\alpha}_1) \mathbf{H}_1(\boldsymbol{\alpha}_1))^{-1} \mathbf{H}_1^T(\boldsymbol{\alpha}_1) \mathbf{y})$$

$$\stackrel{N \rightarrow \infty}{=} \underset{p,f}{\operatorname{argmax}} \left( \frac{(\mathbf{x}^T(p) \mathbf{y})^2 + 2(\mathbf{x}^T(p) \mathbf{x}(p)) I_y(f) - 4(\mathbf{x}^T(p) \mathbf{y}) \operatorname{Re}[I_{xy}(f)] - 4(\operatorname{Im}[I_{xy}(f)])^2}{(\mathbf{x}^T(p) \mathbf{x}(p)) - 2I_x(f)} \right) \quad (3.42)$$

$$\hat{\boldsymbol{\beta}}_1 = \begin{pmatrix} \hat{\lambda}_1 \\ \hat{l}_1 \\ \hat{l}_2 \end{pmatrix} = (\mathbf{H}_1^T(\hat{\boldsymbol{\alpha}}_1) \mathbf{H}_1(\hat{\boldsymbol{\alpha}}_1))^{-1} \mathbf{H}_1^T(\hat{\boldsymbol{\alpha}}_1) \mathbf{y}$$

$$= \begin{pmatrix} \frac{\mathbf{x}^T(\hat{p}_1) \mathbf{y} - 2 \operatorname{Re}[I_{xy}(\hat{f})]}{\mathbf{x}^T(\hat{p}_1) \mathbf{x}(\hat{p}_1) - 2I_x(\hat{f})} \\ \left( \frac{\frac{2}{N} (\mathbf{x}^T(\hat{p}_1) \mathbf{x}(\hat{p}_1)) \mathbf{c}^T(\hat{f}) (\mathbf{y} - r'(\hat{p}_1) \mathbf{x}(\hat{p}_1)) + \frac{4}{N} (\mathbf{x}^T(\hat{p}_1) \mathbf{s}(\hat{f})) \operatorname{Im}[I_{xy}(\hat{f})]}{\mathbf{x}^T(\hat{p}_1) \mathbf{x}(\hat{p}_1) - 2I_x(\hat{f})} \right) \\ \left( \frac{\frac{2}{N} (\mathbf{x}^T(\hat{p}_1) \mathbf{x}(\hat{p}_1)) \mathbf{s}^T(\hat{f}) (\mathbf{y} - r'(\hat{p}_1) \mathbf{x}(\hat{p}_1)) - \frac{4}{N} (\mathbf{x}^T(\hat{p}_1) \mathbf{c}(\hat{f})) \operatorname{Im}[I_{xy}(\hat{f})]}{\mathbf{x}^T(\hat{p}_1) \mathbf{x}(\hat{p}_1) - 2I_x(\hat{f})} \right) \end{pmatrix} \quad (3.43)$$

$$T = \frac{1}{2\sigma^2} \left( \|\boldsymbol{\Pi}_{\mathbf{H}_1(\hat{\boldsymbol{\alpha}}_1)} \mathbf{y}\|^2 - \|\boldsymbol{\Pi}_{\mathbf{H}_0(\hat{\boldsymbol{\alpha}}_0)} \mathbf{y}\|^2 \right)$$

$$= \frac{1}{2\sigma^2} \left( \frac{(\mathbf{x}^T(\hat{p}_1) \mathbf{y})^2 + 2(\mathbf{x}^T(\hat{p}_1) \mathbf{x}(\hat{p}_1)) I_y(\hat{f}) - 4(\mathbf{x}^T(\hat{p}_1) \mathbf{y}) \operatorname{Re}[I_{xy}(\hat{f})] - 4(\operatorname{Im}[I_{xy}(\hat{f})])^2}{(\mathbf{x}^T(\hat{p}_1) \mathbf{x}(\hat{p}_1)) - 2I_x(\hat{f})} - \frac{(\mathbf{x}^T(\hat{p}_0) \mathbf{y})^2}{\mathbf{x}^T(\hat{p}_0) \mathbf{x}(\hat{p}_0)} \right) \quad (3.44)$$

where

$$r'(p) = \frac{\mathbf{x}^T(p) \mathbf{y}}{\mathbf{x}^T(p) \mathbf{x}(p)}$$

and where the terms  $I_x(f)$  and  $I_y(f)$  are the periodograms of  $\mathbf{x}$  and  $\mathbf{y}$

$$I_x(f) = \frac{1}{N} [(\mathbf{c}^T(f) \mathbf{x})^2 + (\mathbf{s}^T(f) \mathbf{x})^2]$$

$$I_y(f) = \frac{1}{N} [(\mathbf{c}^T(f) \mathbf{y})^2 + (\mathbf{s}^T(f) \mathbf{y})^2].$$

Note that  $\text{Re}[I_{xy}(f)]$  and  $\text{Im}[I_{xy}(f)]$  are the real and imaginary parts of the cross-periodogram  $I_{xy}(f)$  (also referred to as co-periodogram and quadrature periodogram)

$$\begin{aligned} I_{xy}(f) &= \frac{1}{N} [(\mathbf{c}^T(f)\mathbf{x} - i\mathbf{s}^T(f)\mathbf{x})(\mathbf{c}^T(f)\mathbf{y} + i\mathbf{s}^T(f)\mathbf{y})] \\ \text{Re}[I_{xy}(f)] &= \frac{1}{N} [(\mathbf{c}^T(f)\mathbf{x})(\mathbf{c}^T(f)\mathbf{y}) + (\mathbf{s}^T(f)\mathbf{x})(\mathbf{s}^T(f)\mathbf{y})] \\ \text{Im}[I_{xy}(f)] &= \frac{1}{N} [(\mathbf{c}^T(f)\mathbf{x})(\mathbf{s}^T(f)\mathbf{y}) - (\mathbf{s}^T(f)\mathbf{x})(\mathbf{c}^T(f)\mathbf{y})]. \end{aligned}$$

Note also that a large sample approximation has been considered for the derivation of  $\hat{\beta}_1$  and  $\hat{\alpha}_1$ . In this case, when  $f$  is not too close to 0 or  $1/2$  (otherwise the parameters are not identifiable), the following approximations can be made  $\mathbf{c}^T \mathbf{c}/N \approx 1/2$ ,  $\mathbf{s}^T \mathbf{s}/N \approx 1/2$  and  $\mathbf{c}^T \mathbf{s}/N \approx 0$ .

### 3.8.2. Theoretical performance

The performance of the corresponding approximate GLRT can be computed using (3.33), where the chi-square non-centrality parameter can be obtained from (3.37) and (3.35)

$$\begin{aligned} k &= \frac{\beta_1^T \mathbf{H}_1^T(\alpha_1) \Pi_{\mathbf{H}_0(\alpha_0)}^\perp \mathbf{H}_1(\alpha_1) \beta_1}{\sigma^2}, & \alpha \text{ known} \\ k_a &= \frac{\beta_1^T \mathbf{H}_1^T(\alpha_1) \mathbf{L}_0^\perp \mathbf{H}_1(\alpha_1) \beta_1}{\sigma^2}, & \alpha \text{ unknown} \end{aligned}$$

and the chi-square degree of freedom can be obtained from (3.36) and (3.34)

$$\begin{aligned} r &= \text{rank}(\mathbf{H}_s) = 2, & \alpha \text{ known} \\ r_a &= \text{rank}(\mathbf{K}_a) = 3, & \alpha \text{ unknown} \end{aligned}$$

Note that, for a known vector  $\alpha$ ,  $k$  reduces to

$$k = \frac{NA^2}{2\sigma^2} - \frac{(l_1(\mathbf{c}^T(f)\mathbf{x}(p)) + l_2(\mathbf{s}^T(f)\mathbf{x}(p)))}{\mathbf{x}(p)^T \mathbf{x}(p) \sigma^2}$$

that can be considered as a signal to noise ratio

$$\text{SNR}_1 = \frac{NA^2}{2\sigma^2}.$$

### Interpretation and comments

It is interesting to observe that if the signal  $\mathbf{x}$  does not contain any signal component at the frequency  $\hat{f}$  ( $\text{Re}[I_x(\hat{f})] = 0$  and  $\text{Im}[I_x(\hat{f})] = 0$ ), the test statistic reduces to the simple periodogram of  $\mathbf{y}$  (indeed, we would

have  $I_x(\hat{f}) = 0$ ,  $\hat{p}_0 = \hat{p}_1$ ,  $\text{Re}[I_{xy}(\hat{f})] = 0$  and  $\text{Im}[I_{xy}(\hat{f})] = 0$ ). In this case, the signal  $\mathbf{x}$  does not bring any useful information for the detection of  $\mathbf{s}$ , and the power spectrum of  $\mathbf{y}$  is all we need to detect the presence of the signal  $\mathbf{s}$ .

If we cannot guarantee the absence of signal power at the frequency  $\hat{f}$  in  $\mathbf{x}$ , but we can consider that the power of the anomaly is small compared to the energy and covariance terms  $\mathbf{x}^T(\hat{p})\mathbf{x}(\hat{p})$  and  $\mathbf{x}^T(\hat{p})\mathbf{y}$ , we can assume that  $\hat{p}_0 \approx \hat{p}_1 \approx \hat{p}$ ,  $(\text{Im}[I_{xy}(\hat{f})])^2 \approx 0$  being a second order term in  $\text{Re}[I_x(\hat{f})]$  and  $\text{Im}[I_x(\hat{f})]$ . The sufficient statistic of our detection problem can then be written as

$$T = \frac{1}{\sigma^2} \left( I_y(\hat{f}) - 2r'(\hat{p})\text{Re}[I_{xy}(\hat{f})] \right)$$

whose dominant term is still the periodogram of  $\mathbf{y}$ , but corrected by an additional term depending on the correlation between  $\mathbf{x}$  and  $\mathbf{y}$  (in the time and frequency domains).

It is also important to mention that when the hypothesis  $\hat{p}_0 \approx \hat{p}_1 \approx \hat{p}$  is valid, the MLEs of  $p$  and  $f$  can be obtained via two 1-dimensional optimization problems<sup>8</sup>. Moreover, the estimation of the system dynamic  $P$  and the detection of the anomaly  $\mathbf{s}$  can be decoupled<sup>9</sup>.

Closed form expressions for the MLEs and the test statistic have been presented as a complement to the matrix form in Section 3.8.1. Indeed, this simple expression for our detector is very appealing if we are looking for a recursive online implementation of the detector. Moreover, the analytic expression of the detector performance, as derived in Section 3.8.2, is a clear advantage in the threshold tuning process for a constant false alarm rate detector. We mention here that only one observation window has been considered in our analysis. However, our results can be easily extended to non-overlapping sliding windows<sup>10</sup>.

### 3.8.3. Synthetic data

The theoretical performance determined in Section 3.8 has been validated numerically by means of Monte Carlo simulations using synthetic data. More precisely,  $\mathbf{x}$  and  $\mathbf{w}$  were generated according to the model discussed in Section 3.8, with a white Gaussian input signal  $\mathbf{x}$ . Figs. 3.11 and 3.12 compare the theoretical performance of the approximate GLRT with the empirical performance of the GLRT for unknown vectors  $\beta$  and  $\alpha$ . The estimation of the unknown parameters  $\alpha$  is carried out considering a grid search optimization, varying the parameters  $(p, f)$  in a priori known ranges  $[p_a, p_b]$  and  $[f_a, f_b]$ . Fig. 3.11 shows  $P_{\text{FA}}$  as a function of the threshold  $\gamma$  for a particular grid associated with  $(p, f)$ , where  $(\Delta p = 1e^{-5}s, \Delta f = 1e^{-4}Hz)$ . For an unknown vector  $\alpha$ , we have shown that the asymptotic performance presented in Section 3.8.2 is valid for a specific value

<sup>8</sup>If we do not have any hypothesis on  $\hat{p}_0$  and  $\hat{p}_1$  we can still reduce the 2-dimensional optimization problem with respect to  $p, f$  by using the so-called Alternating Projection (AP) approach as in [ZW88].

<sup>9</sup>This approach can be very interesting to reduce the computational cost of the algorithm.

<sup>10</sup>For  $M$  non-overlapping windows (white noise) one can simply consider  $P_{\text{FA}} = \prod_{i=1}^M P_{\text{FA}}^i$ , where  $P_{\text{FA}} \ll 1$ . The overlapping windows case (colored noise) is more difficult to handle. However, the case of non-overlapping windows can be considered as a reference in terms of detection performance.

of  $\widehat{d\alpha}$  (see (3.31)).

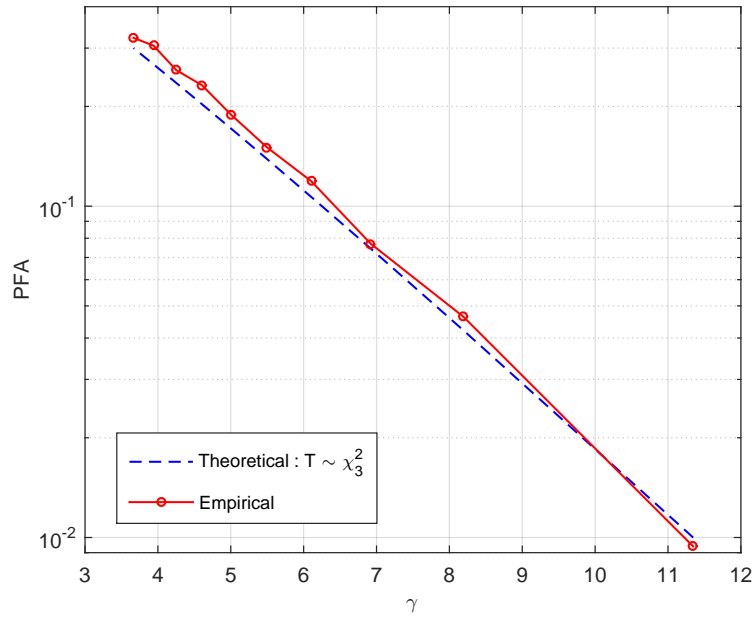


Figure 3.11.: Empirical ( $N_{MC} = 10^4$  realizations,  $\Delta p = 1e^{-5}s$ ,  $\Delta f = 1e^{-4}Hz$ ) and theoretical  $P_{FA}$  as a function of the threshold  $\gamma$ .  $SNR_1 = SNR_2 = 20dB$ .

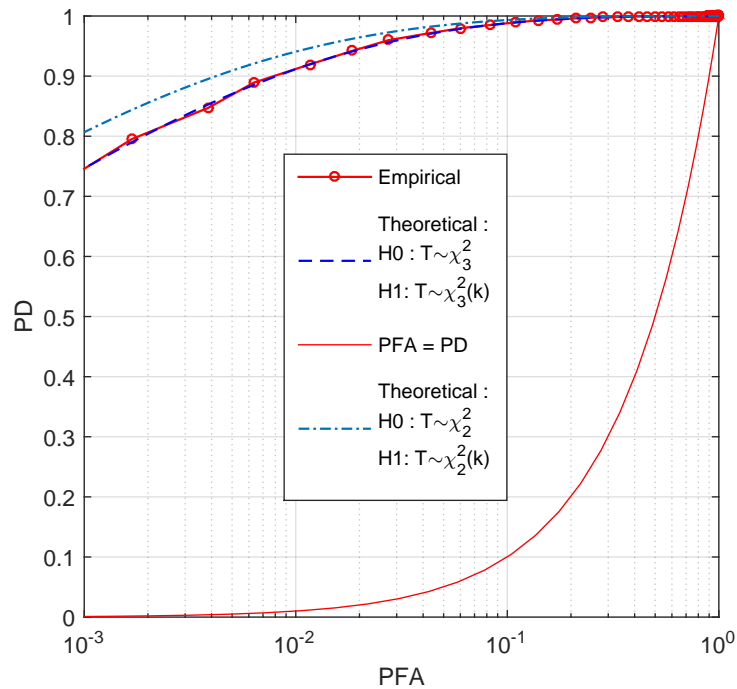


Figure 3.12.: Empirical ( $N_{MC} = 10^5$  realizations,  $\Delta p = 1e^{-5}s$ ,  $\Delta f = 1e^{-3}Hz$ ) and theoretical ROC curves.  $SNR_1 = SNR_2 = 13dB$ .

Finally, the empirical results computed with Monte Carlo runs confirm that the theoretical performance of the approximate GLRT can be used as a reference for the GLRT for the considered test case. Note that the

theoretical curve corresponding to known values of  $\alpha$  is also shown in Fig. 3.12 for comparison. Indeed, it is interesting to observe the performance loss induced by the lack of knowledge about  $\alpha$ .

### 3.9. Conclusions and perspectives

This chapter investigate LCO detection and diagnostic via GLR tests proposing several solutions. The GLRT is derived for the conditional observation model in the general case of parameter dependent observation matrices. The GLRT performance cannot be analytically computed. Thus, we have proposed and analyzed the performance of a test called approximate GLRT, for which the performance can be computed exactly in the high-SNR region. Indeed, the approximate GLRT can be used as a reference for the GLRT. The specific case of deterministic signal detection in deterministic interference has been considered with a specific attention.

The main scientific contributions of this work are the considered general form of the conditional observation model and the proposed procedure to derive the approximate GLRT performance. More precisely, a closed form expression of the approximate GLRT performance is obtained in the asymptotic region by using a Taylor expansion of the test statistic. Indeed, while there exist some interesting results when the asymptotic region is attained through the large sample size hypothesis [MJ15][Wil38], these results cannot be applied in the high-SNR regime for small sample size. The results obtained in this high-SNR regime were compared to those obtained with known observation matrices. We showed that the approximate GLRT test statistic for the conditional observation model can always be expressed as a linear combination of variables distributed according to chi-square distributions, depending on the existing relationship between the observation matrices. Monte Carlo simulations have been considered to compare the empirical GLRT performance and the theoretical approximate GLRT performance (signal detection in deterministic interference case). The results confirm that the approximate GLRT theoretical performances in the asymptotic region are a good reference also for the GLRT.

Multiple research paths can be identified starting from the contribution presented in this chapter.

- this study considered a particular interference model related to our application and a known noise variance. It would be interesting to extend our derivations to different interference models<sup>11</sup> with a possible unknown noise variance.
- the considered composite hypothesis testing problem involves an estimation scheme intrinsically and hence suffers from the curse of dimensionality and a zone of indifference. Indeed, with a high-dimensionality of the unknown parameters, there is a zone in terms of the geometry of the unknown parameters where a detector is rendered inconclusive. In order to face this type of issue, there exists different tools that can be used to transform a problem with a large number of dimensions into an equivalent problem involving

---

<sup>11</sup>For example, the first order model considered for the actuator system is an approximation that is quite accurate only for low input frequencies, for higher frequencies we should consider also the effect of higher order dynamics.

only a small number of dimensions [Lev08]. This is another interesting research path for further studies.

- The Alternating Projection approach (see Appendix A.4) could be considered to simplify the test computation.
- Having some a priori information about our problem and willing to introduce these information in the detector, a Bayesian approach can be considered for the derivation of the test statistic.
- for some application a different noise model can be more relevant. For example a Laplacian noise model ( $w(n) \sim \mathcal{L}(0, b)$ ) could be closer to reality [Lav+14].
- In case we have multiple observation of the signal  $y$ , the presented formulation can be easily modified

$$\mathbf{y}_t = \mathbf{H}(\boldsymbol{\alpha})\boldsymbol{\beta}_t + \mathbf{w}_t, \quad 1 \leq t \leq T, \quad \mathbf{w}_t \text{ i.i.d}$$

$$\mathbf{J}(\boldsymbol{\alpha}, \boldsymbol{\beta})_T = \sum_{t=1}^T \|\mathbf{y}_t - \mathbf{H}(\boldsymbol{\alpha})\boldsymbol{\beta}_t\|^2 \boldsymbol{\beta}_t = (\mathbf{H}^T(\boldsymbol{\alpha})\mathbf{H}(\boldsymbol{\alpha}))^{-1}\mathbf{H}^T(\boldsymbol{\alpha})\mathbf{y}_t$$

$$\boldsymbol{\alpha} = \operatorname{argmax}_{\boldsymbol{\alpha}} \sum_{t=1}^T \|\boldsymbol{\Pi}_{\mathbf{H}}(\boldsymbol{\alpha})\mathbf{y}_t\|^2 = \operatorname{argmax}_{\boldsymbol{\alpha}} \{\operatorname{tr}(\boldsymbol{\Pi}_{\mathbf{H}}(\boldsymbol{\alpha})\hat{\mathbf{R}}_y)\}, \quad \hat{\mathbf{R}}_y = \frac{1}{T} \sum_{t=1}^T \mathbf{y}_t\mathbf{y}_t^T$$

The direct application of this estimator is often computationally expensive. In the literature other methods have been proposed to solve the problem in more efficient way, avoiding the full search procedure [Chu10].

- Other signals can be used for LCO detection or to complement the information provided by the signal  $\mathbf{x}$  and  $\mathbf{y}$ . It is the case for some accelerometers information available in the Flight Control Computers (for example the aircraft  $N_z$  and  $N_y$  measured in the air data inertial reference unit (ADIRU)). A data fusion algorithm or a multiple hypothesis testing algorithm might be investigated for LCO detection.



# 4

## Freeplay estimation via Wiener model identification

### Contents

---

<b>4.1. Introduction</b> . . . . .	<b>53</b>
<b>4.2. Introduction to Kernel Regression</b> . . . . .	<b>54</b>
4.2.1. Kernel density estimation . . . . .	54
4.2.2. Kernel regression . . . . .	54
4.2.3. Bandwidth selection . . . . .	55
<b>4.3. Non-parametric Wiener system identification</b> . . . . .	<b>57</b>
4.3.1. Nadaraya-Watson kernel estimator . . . . .	57
Example on synthetic data . . . . .	59
Bandwidth selection . . . . .	62
Filter order selection . . . . .	62
Effect of the number of samples and SNR . . . . .	63
4.3.2. Wiener model identification for hysteresis non linearity . . . . .	64
Example on synthetic data . . . . .	65
Effect of the number of samples and SNR . . . . .	68
4.3.3. Constrained Kernel Regression . . . . .	69
Constraints on $g(\omega)$ . . . . .	70
Constraints on $g^{(s)}(\omega)$ . . . . .	72
<b>4.4. Parametric estimation</b> . . . . .	<b>75</b>
4.4.1. Deterministic Cramér-Rao bounds . . . . .	77
4.4.2. A lower bound on the global estimation error . . . . .	78
4.4.3. Maximum Likelihood estimator . . . . .	79
<b>4.5. Conclusions and Perspectives</b> . . . . .	<b>83</b>

---

### 4.1. Introduction

The purpose of this chapter is to study a suitable method for mechanical free play estimation and as a consequence for LCO diagnosis/prevention. The basic idea is to model the control surface servoloop as a block model where the free play (that we want to measure) is an unknown that can be estimated from the system input/output signals (as already mentioned in Section 2.5). The chosen approach is based on the theory of Wiener system identification. Inspired by the work of Pawlak [PHW07] on **nonparametric** Wiener model

identification, we have tried to adapt this solution to our technical problem defining some variants to the original algorithm (hysteresis non linearity and multiple constraints) and we have compared this solution to the maximum likelihood estimator and to some theoretical performance bounds.

## 4.2. Introduction to Kernel Regression

### 4.2.1. Kernel density estimation

The oldest and most widely used non parametric density estimator is the histogram. This is usually formed by dividing the real line into equally sized intervals, often called bins. The histogram is then a step function whose heights are the proportions of the sample contained in that bin divided by the width of the bin. Kernel density estimates are closely related to histograms, but can be endowed with properties such as smoothness or continuity by using a suitable kernel (see Figure 4.1).

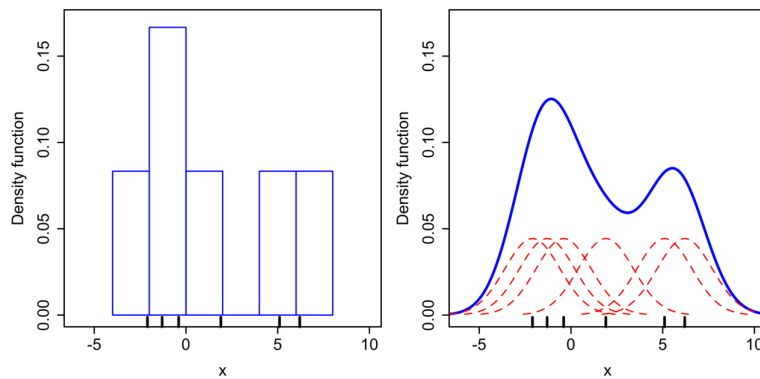


Figure 4.1.: Comparison of the histogram and kernel density estimate on the same data [Wik19a].

The expression of the simplest univariate kernel density estimator is

$$\hat{f}_h(x) = \frac{1}{n} \sum_{i=1}^n K_h(x - x_i) = \frac{1}{nh} \sum_{i=1}^n K\left(\frac{x - x_i}{h}\right) \quad (4.1)$$

where  $K$  is the kernel (a non-negative function that integrates to one) and  $h > 0$  is a smoothing parameter called the bandwidth. The bandwidth of the kernel is a free parameter which exhibits a strong influence on the resulting estimate. It can be used as a trade-off parameter allowing the bias and variance of the estimator to be controlled.

### 4.2.2. Kernel regression

In this section the Kernel regression approach is presented as in [Wik19b], for more information the reader may refer to [WJ94].

In a non parametric regression, the conditional expectation of a variable  $Y$  relative to a variable  $X$  may be written as

$$E(Y|X) = m(X) \quad (4.2)$$

where  $m$  is an unknown function. Nadaraya and Watson, both in 1964, proposed to estimate  $m$  as a locally weighted average, using a kernel as a weighting function. Indeed, considering that

$$E(Y|X = x) = \int y f(y|x) dy = \int y \frac{f(x, y)}{f(x)} dy \quad (4.3)$$

and using the following kernel density estimators

$$\hat{f}(x, y) = \frac{1}{n} \sum_{i=1}^n K_h(x - x_i) K_h(y - y_i) \quad (4.4)$$

$$\hat{f}(x) = \frac{1}{n} \sum_{i=1}^n K_h(x - x_i) \quad (4.5)$$

one can obtain

$$\begin{aligned} \hat{E}(Y|X = x) &= \int y \frac{\sum_{i=1}^n K_h(x - x_i) K_h(y - y_i)}{\sum_{j=1}^n K_h(x - x_j)} dy \\ &= \frac{\sum_{i=1}^n K_h(x - x_i) \int y K_h(y - y_i) dy}{\sum_{j=1}^n K_h(x - x_j)} \\ &= \frac{\sum_{i=1}^n K_h(x - x_i) y_i}{\sum_{j=1}^n K_h(x - x_j)} \end{aligned} \quad (4.6)$$

which is the Nadaraya–Watson Kernel estimator. Note that the Gaussian kernel is one of the most widely used. It can be expressed as

$$K_h(x) = \exp\left(-\frac{x^2}{2h^2}\right) \quad (4.7)$$

where  $h$  is a bandwidth parameter allowing the variance of the Gaussian to be adjusted.

### 4.2.3. Bandwidth selection

The bandwidth of the kernel is a free parameter which exhibits a strong influence on the resulting estimate. The most common criterion used to select this parameter is the mean integrated squared error (MISE)

$$\text{MISE}(h) = E\left[\int (\hat{f}_h(x) - f(x))^2 dx\right].$$

A problem with the MISE expression is that it depends on the bandwidth in a complicated way. A way of overcoming this problem is to derive a large sample approximation for the leading variance

$$\text{MISE}(h) = \text{AMISE}(h) + o((nh)^{-1} + h^4) \quad (4.8)$$

where the AMISE (Asymptotic MISE) is

$$\text{AMISE}(h) = (nh)^{-1}R(K) + \frac{1}{4}h^4\mu_2^2(K)R(f''). \quad (4.9)$$

where the notation  $R(g) = \int g^2(x)dx$  is considered. In the AMISE expression the integrated squared bias is proportional to  $h^4$  and the integrated variance is proportional to  $(nh)^{-1}$ . So, there exists a variance-bias trade-off that defines the optimal bandwidth parameter  $h$ . Setting  $\text{AMISE}(h)$  to zero leads to

$$h_{\text{AMISE}} = \left[ \frac{R(K)}{\mu_2^2(K)R(f'')n} \right]^{1/5} \quad (4.10)$$

Unfortunately, a direct use of the previous expression is not possible since  $R(f'')$  is unknown. There exists several ways for selecting a suitable value of  $h$  as plug-in methods and cross validation methods [JMS96][WJ94]. The plug-in methods are among the simpler and most adopted methods for bandwidth selection. To give an example, if Gaussian basis functions are used and the univariate density to be estimated is Gaussian, the optimal choice [Sil18] for  $h$  is

$$h_S \approx 1.06\hat{\sigma}n^{-1/5} \quad (4.11)$$

where  $\hat{\sigma}$  is the standard deviation of the samples. This value can be used as a reference for the selection of  $h$  and is referred to as Silverman's rule of thumb. While this rule is easy to compute, it should be used with caution as it can yield inaccurate estimates when the density is not normal.

## Kernel density estimator variants

Two variants of the aforementioned kernel density estimator are often considered to tackle specific issues

- Variable kernel density estimators [WJ94, Section 2.10.2]. When the bandwidth is not a constant parameter and depends on the location of either the estimate (balloon estimator) or the samples (pointwise estimator), we obtain adaptive kernel density estimators also referred to as variable bandwidth estimators.
- Transformation kernel density estimator [WJ94, Section 2.10.3]. If the random sample  $X_1, \dots, X_n$  has a density  $f$  that is difficult to estimate, a possibility is to apply a transformation to the data to obtain a

new sample  $Y_1, \dots, Y_n$  having a density  $g$  that can be more easily estimated using the basic kernel density estimator. One would then back-transform the estimate of  $g$  to obtain the estimate of  $f$ . The resulting estimator is called the transformation kernel density estimator.

### 4.3. Non-parametric Wiener system identification

#### 4.3.1. Nadaraya-Watson kernel estimator

Many nonlinear models such as Wiener and Hammerstein models are composed by a combination of a linear filter and a static nonlinearity (see Fig. 4.2). The combination of these very simple structures is known to approximate a wide range of nonlinear processes [GS01][Nel01][GP08][GB10][Gir+13]. In particular, these models become particularly attractive if one considers a general class of nonlinearities that are not assumed to be parametric and smooth, providing better results than a simple polynomial of finite order [MS00]. It is possible to extend even more their applicability to nonlinear system identification if one assumes a nonparametric model for the static nonlinearity, as introduced in [GP08][Gre92] for nonlinear Wiener models (NWMs) and extended in [GP08][PHW07] for noninvertible nonlinearities. A nonparametric identification algorithm was proposed in [PHW07] for NWMs. The convergence of this algorithm relies on the following assumptions: (i) the input signal  $\{x_n\}$  is a sequence of i.i.d. random variables with known probability density function (pdf) and finite first and second order moments, (ii) the noise process  $\{z_n\}$  is an i.i.d. sequence with zero mean and finite but unknown variance  $\sigma_z^2$ , (iii) the noise  $\{z_n\}$  and the input signal  $\{x_n\}$  are mutually independent. The above basic assumptions imply that both the interconnecting signal  $\{\omega_n\}$ <sup>1</sup> and the output signal  $\{y_n\}$  are second-order stationary stochastic processes. The nonlinear Wiener model shown in Fig. 4.2 is defined as

$$y_n = g(\omega_n) + z_n, \quad \omega_n = \sum_{p=0}^P \lambda_p x_{n-p}, \quad 1 \leq n \leq N \quad (4.12)$$

where  $g(\cdot)$  is an unknown deterministic function of  $\Omega \rightarrow \mathbb{R}$ ,  $\Omega \subset \mathbb{R}$ ,  $\boldsymbol{\lambda} = (\lambda_0, \lambda_1, \dots, \lambda_P) \in \mathbb{R}^{P+1}$  is an unknown deterministic vector and  $\mathbf{y} = (y_1, \dots, y_N)^T$ ,  $\boldsymbol{\omega} = (\omega_1, \dots, \omega_N)^T$ ,  $\mathbf{g}(\boldsymbol{\omega}) = (g(\omega_1), \dots, g(\omega_N))^T$ ,  $\mathbf{z} = (z_1, \dots, z_N)^T$ ,  $\mathbf{x} = (x_1, \dots, x_N)^T$ .

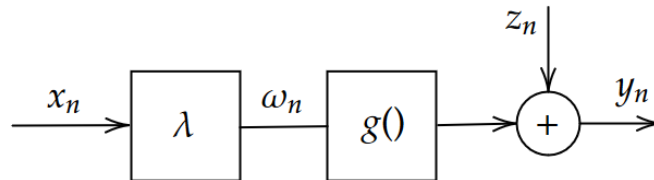


Figure 4.2.: Wiener Model.

<sup>1</sup>System identification algorithms assume that the input and output sequences  $\{x_n\}$  and  $\{y_n\}$  are available. However, the so-called interconnecting signal  $\{\omega_n\}$  is not observed.

It is important to observe that the pairs  $(\mathbf{g}(\boldsymbol{\omega}), \boldsymbol{\lambda})$  and  $(\mathbf{g}(\lambda_0 \boldsymbol{\omega}), \boldsymbol{\lambda}/\lambda_0)$  generate the same observations. Indeed, the pair  $(\mathbf{g}(\boldsymbol{\omega}), \boldsymbol{\lambda})$  can be identified up to an homothetic transformation affecting  $g(\cdot)$ . This identifiability problem can be bypassed by assuming  $\lambda_0 = 1$ , leading to

$$y_n = g(\omega_n) + z_n, \quad \omega_n = x_n + \sum_{p=1}^P \lambda_p x_{n-p}, \quad 1 \leq n \leq N \quad (4.13)$$

where  $\boldsymbol{\lambda} = (\lambda_1, \dots, \lambda_P) \in \mathbb{R}^P$ . In [PHW07] the identification of the model 4.13 is accomplished in three steps: (i) Partitioning of the training set  $T$  into two non overlapping subsets  $T_1, T_2$  as in Figure 4.3.  $T_1$  is used to estimate the non linearity  $g(\cdot)$ , while  $T_2$  is used to recover the impulse response sequence  $\boldsymbol{\lambda}$ . ( $T_1, T_2$  are chosen statistically independent in order to achieve the separation of the linear and non linear estimation problems).

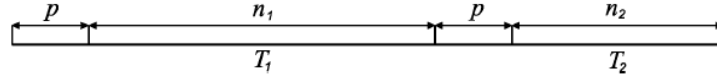


Figure 4.3.: Partition of the training set  $T$ .

(ii) Estimation of  $\boldsymbol{\lambda}$  by a nonlinear least-squares method utilizing a pilot non-parametric estimate of  $g(\cdot)$ , where the Nadaraya-Watson kernel estimate is considered [WJ94] and  $h > 0$  is a smoothing parameter. More precisely, the filter coefficients are estimated as the solution of the following optimization problem

$$\hat{\boldsymbol{\lambda}} = \underset{\boldsymbol{\lambda}}{\operatorname{argmin}} \hat{Q}(\boldsymbol{\lambda}) \quad (4.14)$$

where

$$\hat{Q}(\boldsymbol{\lambda}) = \frac{1}{n_2} \sum_{i \in I_2} \{y_i - \hat{g}(\omega_i; \boldsymbol{\lambda})\}^2 \quad (4.15)$$

$$\hat{g}(\omega; \boldsymbol{\lambda}) = \frac{\sum_{j \in I_1} y_j K_h(\omega - \omega_j(\boldsymbol{\lambda}))}{\sum_{j \in I_1} K_h(\omega - \omega_j(\boldsymbol{\lambda}))} \quad (4.16)$$

(iii) Estimation of  $g(\cdot)$  by using a non parametric kernel regression estimate of the regression function of  $y_n$  with the weights  $\hat{\omega}_n(\hat{\boldsymbol{\lambda}})$ , i.e.,

$$\hat{g}(\omega, \hat{\boldsymbol{\lambda}}) = \frac{\sum_{j \in I_1} y_j K_h(\omega - \omega_j(\hat{\boldsymbol{\lambda}}))}{\sum_{j \in I_1} K_h(\omega - \omega_j(\hat{\boldsymbol{\lambda}}))}. \quad (4.17)$$

The least-squares method previously proposed yields an implicit estimator of  $\boldsymbol{\lambda}$ . However, if we limit the class of input signals to be white and Gaussian, then it can be shown [PHW07] that the following explicit estimator

of  $\boldsymbol{\lambda}$  can be considered

$$\hat{\lambda}_i = \frac{\sum_{j=i+1}^n x_j y_j}{\sum_{j=1}^n x_j y_j}, \quad i = 1, 2, \dots, p. \quad (4.18)$$

In [PHW07] the following measures of performance are considered

$$E(\hat{\boldsymbol{\lambda}}) = \frac{1}{L} \sum_{i=1}^L \frac{\|\hat{\boldsymbol{\lambda}}^i - \boldsymbol{\lambda}\|}{\|\boldsymbol{\lambda}\|}$$

$$\text{MISE} = \frac{1}{LT} \sum_{i=1}^L \sum_{j=1}^T (g(\omega_j) - \hat{g}^i(\omega_j, \hat{\boldsymbol{\lambda}}))^2$$

where  $L$  and  $T$  are the number of realizations and the number of points that approximate the non linearity. In the next sections we will consider also the normalized mean square error (NMSE) as index of performance (the true values of  $\boldsymbol{\lambda}$  and  $g()$  are generally unknown) defined as

$$\text{NMSE} = 1 - \frac{\|\mathbf{y} - \hat{\mathbf{y}}\|^2}{\|\mathbf{y} - \bar{\mathbf{y}}\|^2} \in [-\infty, 1] \quad (4.19)$$

where  $\mathbf{y}$  is the actual system output,  $\hat{\mathbf{y}}$  the estimated output from the Wiener model and  $\bar{\mathbf{y}} = \frac{1}{N} \sum_{i=1}^N y_i$ .

### Example on synthetic data

This section considers an example of application of the algorithm proposed by Pawlak [PHW07] on synthetic data in order to get familiar with the method and understand the influence of some specific parameters on the estimator performance. Figure 4.4 shows the input/output signals of a Wiener system. Figure 4.5 displays the histograms of the signals  $\{x_n\}$ ,  $\{\omega_n\}$ ,  $\{y_n\}$ , where we emphasize that  $\{x_n\}$  and  $\{y_n\}$  are observed, while  $\{\omega_n\}$  is unknown.

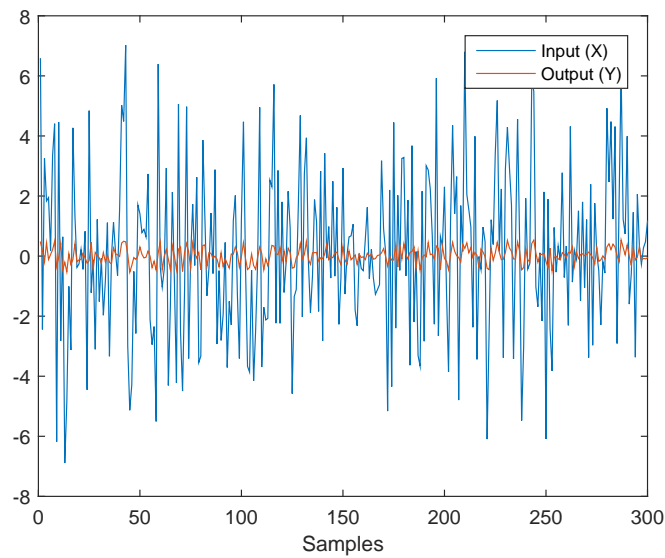


Figure 4.4.: Example of input/output data of a Wiener model.  $\text{SNR} = 20\text{dB}$ .

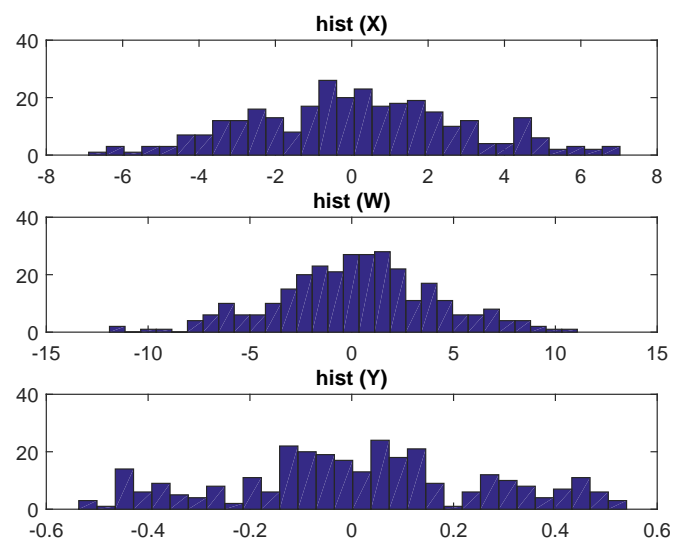


Figure 4.5.: Histograms of the synthetic data of Fig. 4.4.

Figure 4.6 compares the output of the algorithm (estimated parameters  $\lambda$  and estimated non linearity  $g$ ) with the true simulated values. For the considered input signal and system dynamic, Pawlak's method [PHW07] (called PM1 in Figure 4.6) performs very well.

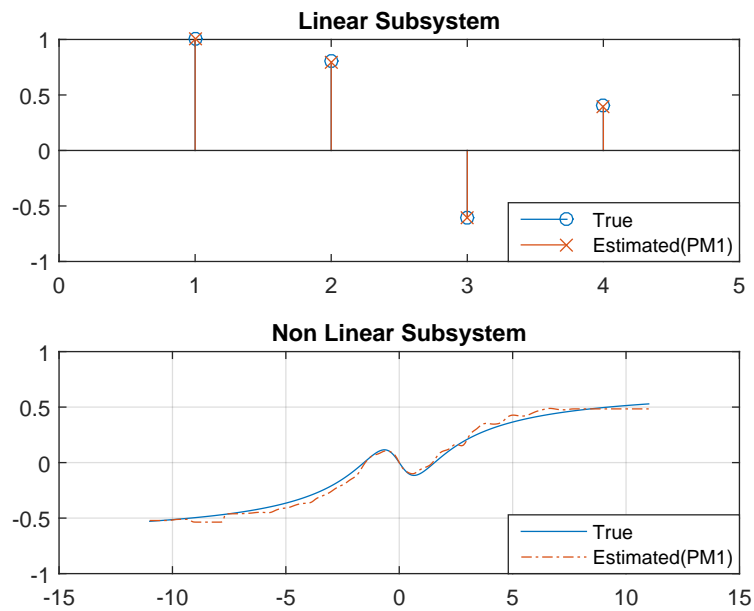


Figure 4.6.: Estimated Linear and Nonlinear subsystems from the synthetic data of Fig. 4.4.  $h = h_S/4$ .

It is also interesting to have a look to the variance of the estimator. In Figure 4.7, fifty identified models are superimposed and compared to the true system. It can be seen that all identified models are close to the true system. Table 4.1 provides some quantitative results in terms of NMSE. Note that the estimated response is always very close to the true response.

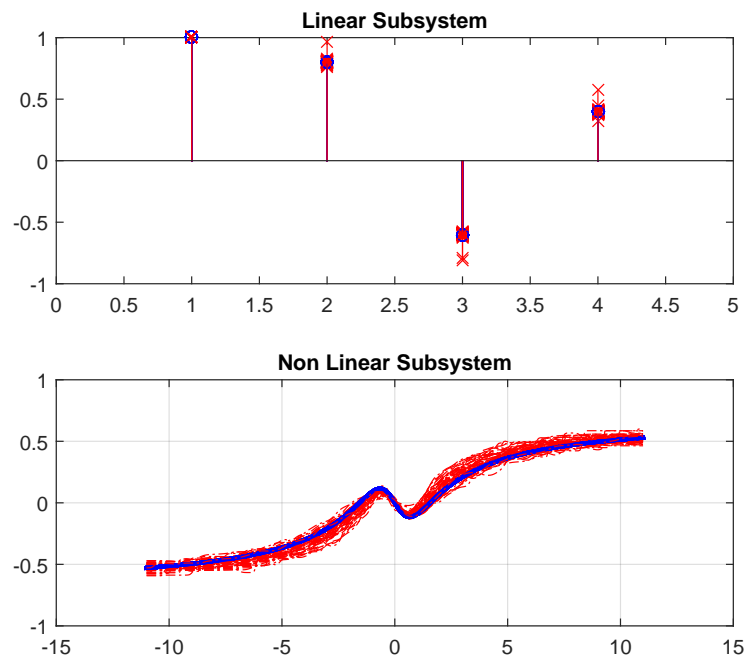


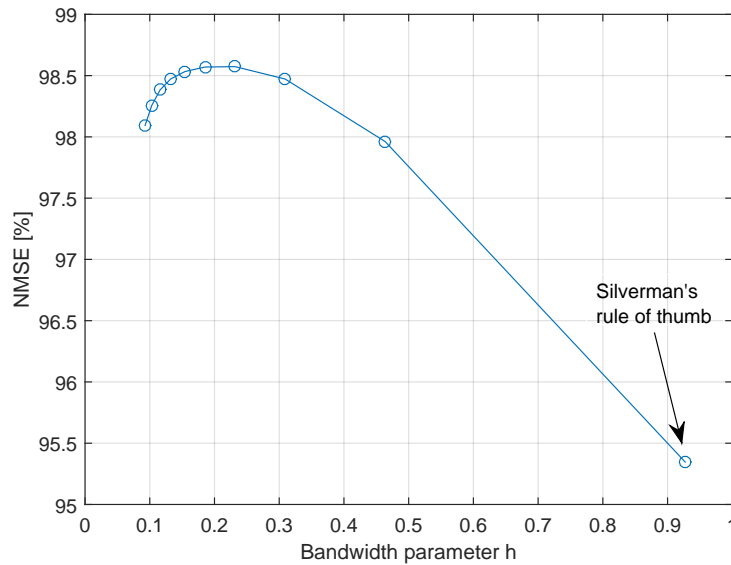
Figure 4.7.: Different realizations of the estimator for the set in Fig. 4.4.  $h = h_S/4$ . 50 identified models are superimposed in the figure (red) compared to the true system (blue).

Table 4.1.: NMSE for 50 runs on the set in Fig. 4.4.

	NMSE
Mean	96.9%
Median	98.9%
$\sigma$	6.4%

### Bandwidth selection

In Section 4.2.3 we have mentioned that the bandwidth of the kernel can have a strong influence on the resulting estimator. The previous Figures 4.6 and 4.7 were obtained with a specific bandwidth parameter ( $h = h_S/4$ ). This value of the bandwidth was chosen in order to maximize the NMSE; Indeed, the value  $h = h_S/4$  is close to the optimum (in terms of NMSE) for the considered example, as shown in Figure 4.8. The Silverman's rule of thumb ( $h = h_S$ ) is slightly sub-optimal<sup>2</sup> in terms of NMSE for our test case (and for higher values of  $h$  the NMSE tends to decrease further).

Figure 4.8.: Normalized Mean Square Error (NMSE) as a function of the bandwidth parameter  $h$  for the set in Fig. 4.4.

### Filter order selection

The filter order was supposed to be known in [PHW07], which is often not the case in practical applications. Figure 4.9 shows the effect of mispecifying the value of  $p$  for a true filter order equal to  $p_{\text{true}} = 3$ . It can be seen that overestimating the value of  $p$  leads to good estimations of the filter response. However, underestimating  $p$  provides a significant drop of the estimator performance.

<sup>2</sup>Silverman's rule has been obtained for Gaussian density estimation. There are no guarantees to obtain optimal results applying the same rule to the considered Kernel regression problem (Wiener model identification).

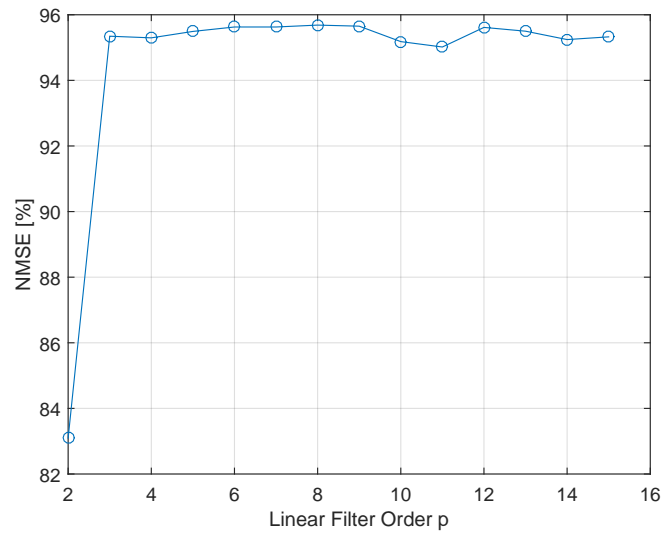


Figure 4.9.: Normalized Mean Square Error (NMSE) as a function of the filter order  $p$  for the set in Fig. 4.4.  $h = h_S$ . Actual order  $p_{\text{true}} = 3$ .

### Effect of the number of samples and SNR

The considered number of samples has also a strong impact on the estimator performance. It can be seen that, for the considered example, there is a strong threshold effect around 200 samples (see Figure 4.10).

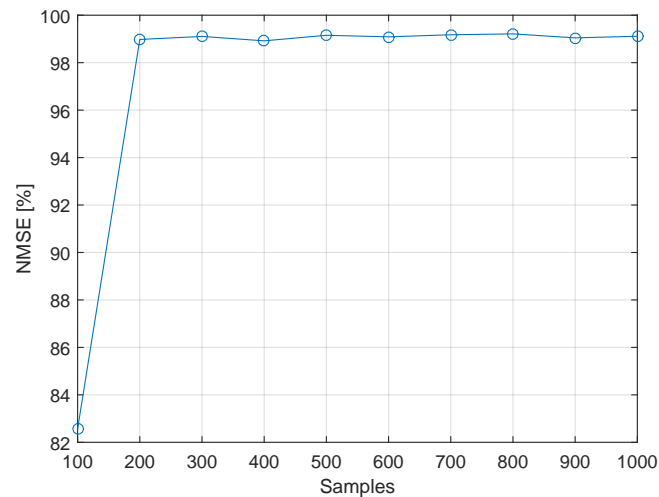


Figure 4.10.: Normalized Mean Square Error (NMSE) as a function of the number of samples  $N$  for the set in Fig. 4.4.  $h = h_S/4$ .

The additive noise  $\mathbf{z}$  has also a strong influence on the estimation performance. Figure 4.11 displays the NMSE as a function of SNR for the previous examples. A higher noise power yields reduced estimation performance.

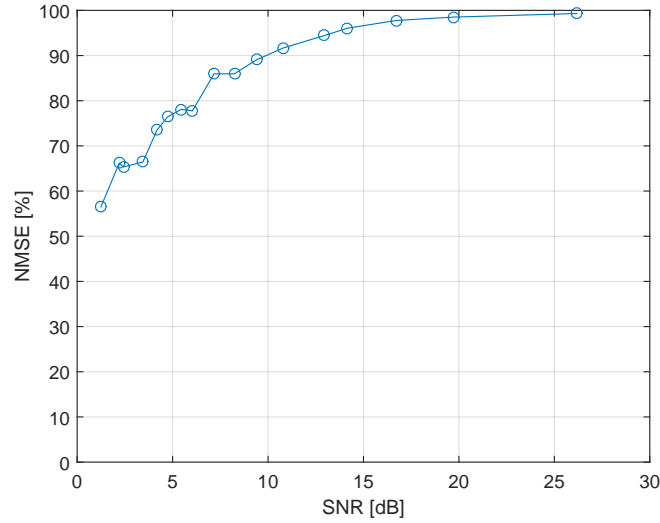


Figure 4.11.: Normalized Mean Square Error (NMSE) as a function of the Signal to Noise Ratio (SNR) for the set in Fig. 4.4.  $h = h_S/4$ .

The effect of the initialization on the optimization algorithm used to solve (4.14) needs to be studied. If the input signal is Gaussian, as in Figure 4.4, one can choose to initialize the vector  $\lambda$  directly via (4.18). However, if the input is not Gaussian, initialization deserves a more specific attention. It is important to observe that the optimization problem in (4.14) is nonconvex and can thus be characterized by several local minima [PHW07]. In addition to sensitivity to initialization, it is important to observe that kernel density estimators may perform very poorly for some particular density shapes. Indeed, densities close to the Gaussian one are easier to estimate than other densities having large skeweness or kurtosis or being multimodal. To give an example, it can be shown that estimating the log-normal density with the same accuracy as for the normal density requires a number of samples 15 times larger [WJ94].

**Note:**

The optimization routine considered in this study to solve (4.14) is the Levenberg–Marquardt algorithm [Lev44][Mar63][Mor78] (i.e., *lsqnonlin* function in MATLAB).

### 4.3.2. Wiener model identification for hysteresis non linearity

This section investigates the problem of Wiener model identification when the system is subjected to hysteresis phenomena. Indeed, play and backlash may induce hysteresis phenomena in the control surface position measure, which needs to be handled for the proposed application. Hysteresis is the dependence of the state of a system on its history. A loop or hysteresis curve can be observed when there are different values of one variable depending on the direction of change of another variable, as illustrated in Figure 4.12.

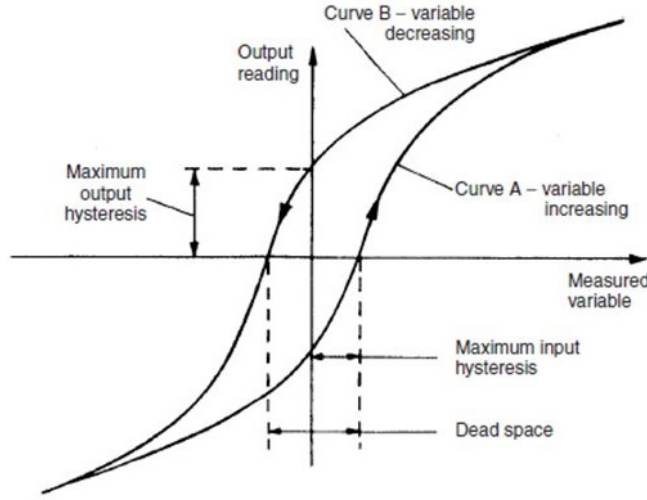


Figure 4.12.: Hysteresis effect.

There exists a wide literature about hysteresis modeling [Vis96]. However, for the purpose of this study we will consider the simple model (due to the physicist P. Duhem) where for any differentiable input function  $u(t)$  and output function  $w(t)$  we have

$$\frac{dw}{du} = \begin{cases} g_1(u, w) & \text{if } du > 0 \\ g_2(u, w) & \text{if } du < 0 \end{cases} \quad (4.20)$$

The curves  $g_1$  and  $g_2$  respectively represent the paths of evolution of the pair  $(u, w)$  for increasing and decreasing  $u$ . The method presented in Section 4.3.1 can be easily adapted to tackle this type of nonlinearity considering a four step procedure: (i) partitioning of the training set  $T$  into two non overlapping subsets  $T_1, T_2$  as in Figure 4.3; (ii) Partitioning of the test set  $T_i$  in two subsets  $T_i^+, T_i^-$  such as

$$\begin{cases} T_i^+, & \Delta\omega_n = \omega_n(k) - \omega_n(k-1) > 0 \\ T_i^-, & \Delta\omega_n < 0 \end{cases} \quad (4.21)$$

(iii) Linear sub-system estimation from  $T_2$  and (iv) estimation of the non linearity from  $T_1$ .

Finally, we can observe that the algorithm is the same as in Section 4.3.1 except that the function  $g$  is now composed of two functions  $g^+$  and  $g^-$  resulting from  $T_i^+$  and  $T_i^-$ .

### Example on synthetic data

This section studies an example of application of the proposed algorithm for synthetic data subjected to hysteresis. Figures 4.13 and 4.14 displays the input/output data and the histograms of the signals  $\{x_n\}, \{\omega_n\}, \{y_n\}$

for this example.

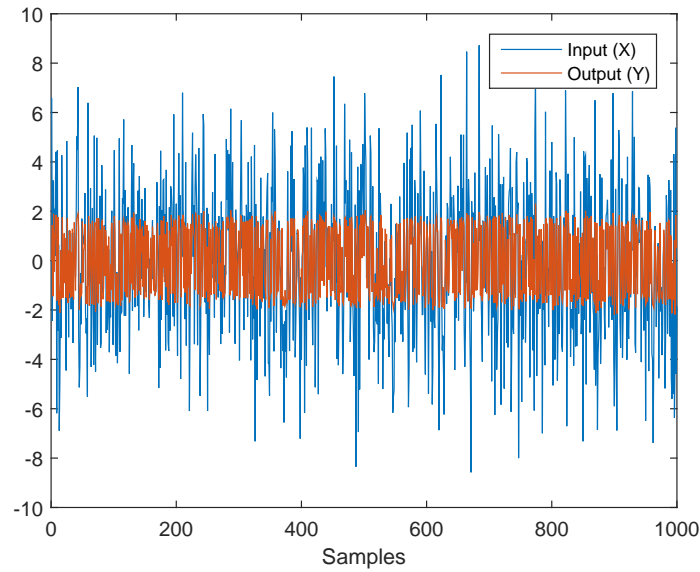


Figure 4.13.: Example of Input/Output data that can be related via a Wiener model with hysteresis non linearity. SNR = 40dB.

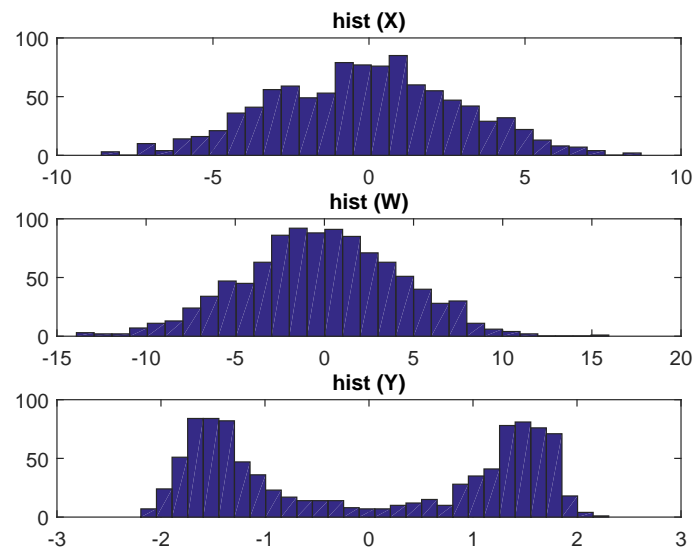


Figure 4.14.: Histograms of the synthetic data of Fig. 4.13.

Figure 4.15 compares the true and estimated Wiener system as in Figure 4.6. The estimated nonlinearity is very close to the true simulated hysteresis cycle confirming the applicability of the method.

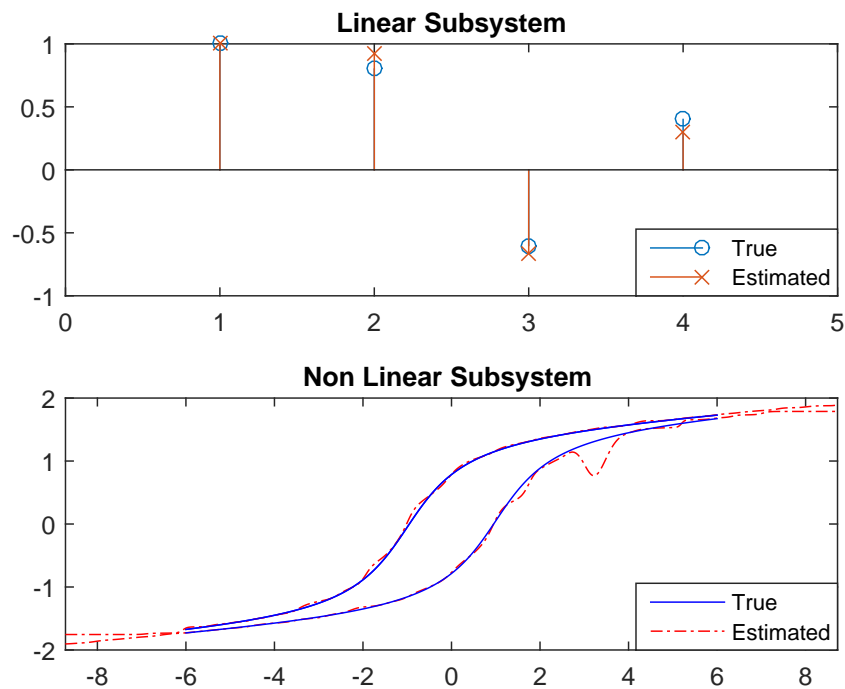


Figure 4.15.: Estimated Linear and Nonlinear subsystems from the synthetic data of Fig. 4.13.  $h = h_S/4$ .

Due to the presence of hysteresis, the density to be estimated is a bimodal distribution (see Figure 4.14). The multimodality generally raises an additional difficulty to the estimation problem. However, in the considered example the algorithm still performs very well<sup>3</sup> (see Figure 4.16).

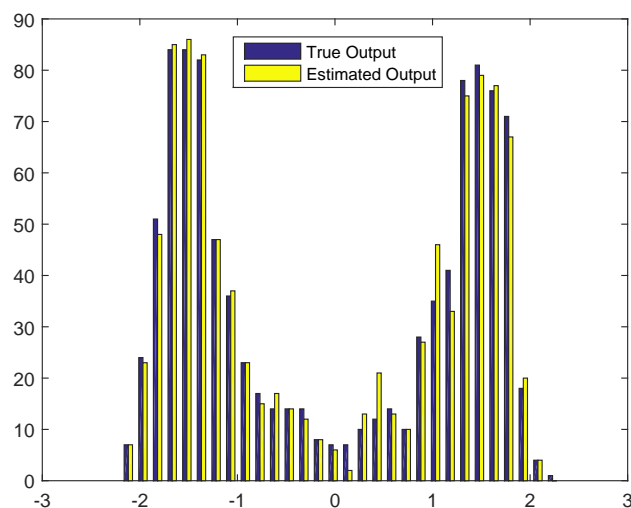


Figure 4.16.: Histograms of the actual and estimated outputs.

Analyzing the variance of the estimator (Figure 4.17), we can observe (as in Figure 4.7) that all identified

<sup>3</sup>This is also possible thanks to the larger number of samples ( $N = 1000$ ) and the higher SNR when compared to the case in Figure 4.4.

models are close to the true system. Table 4.2 provides some quantitative results of this analysis in terms of NMSE, which confirm that the estimated nonlinearity is always very close to the true system response.

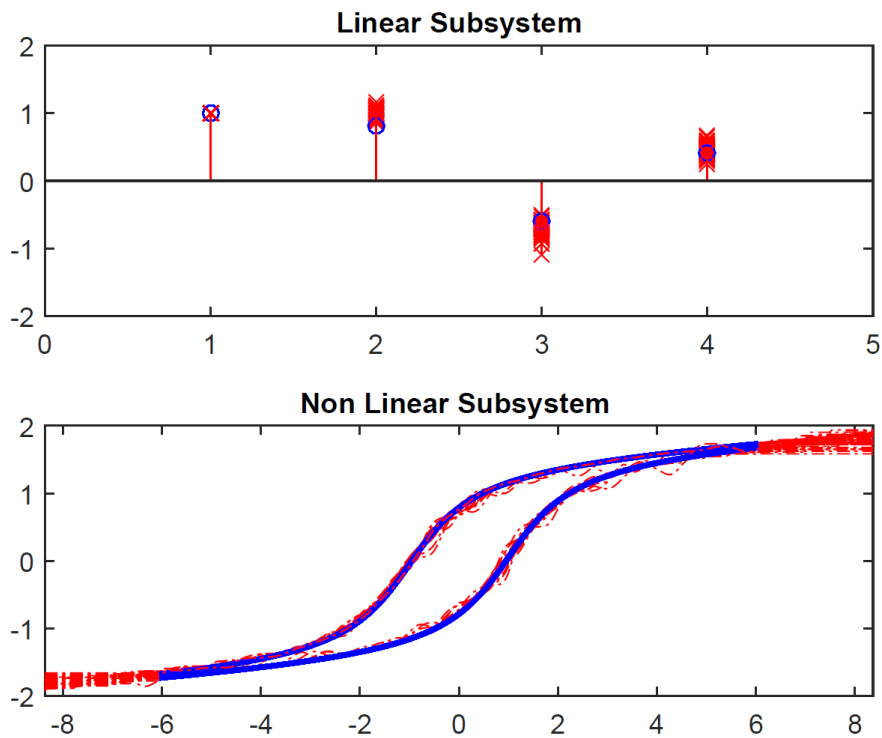


Figure 4.17.: Different realizations of the estimator for the set in Fig. 4.13.  $h = h_S/4$ . 50 identified models are superimposed in the figure (red) that can be compared to the true system (blue).

Table 4.2.: NMSE for 50 runs on the set in Fig. 4.13

	NMSE
Mean	99.8%
Median	99.9%
$\sigma$	0.5%

### Effect of the number of samples and SNR

The influence of the number of samples and the noise level is shown in Figures 4.18 and 4.19 that are similar to Figures 4.10 and 4.11.

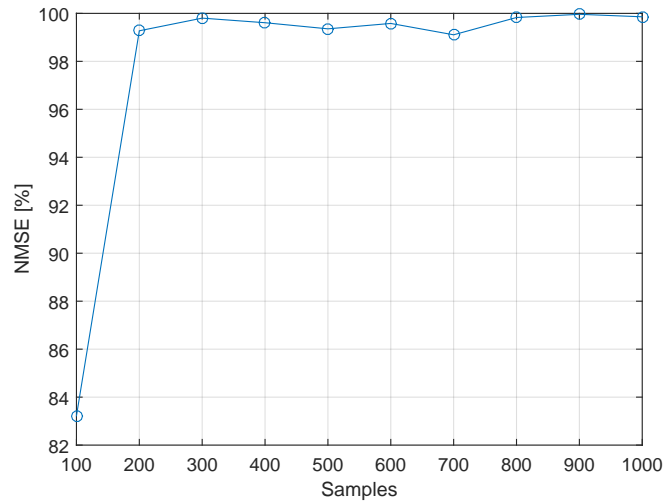


Figure 4.18.: Normalized Mean Square Error (NMSE) as a function of the number of samples  $N$  for the set in Fig. 4.13.  $h = h_S/4$ .

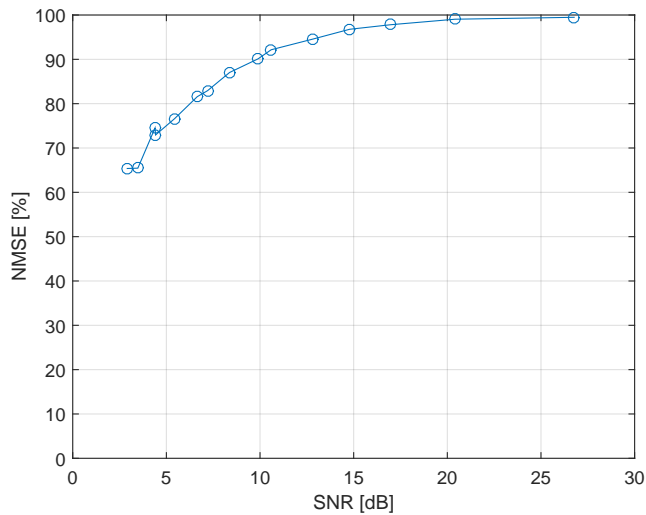


Figure 4.19.: Normalized Mean Square Error (NMSE) as a function of the Signal to Noise Ratio (SNR) for the set in Fig. 4.13.  $h = h_S/4$ .

### 4.3.3. Constrained Kernel Regression

In our application (free play estimation in the control surface servo loop) the practitioner may have some a priori information about the nonlinearity shape. Thus, it is interesting to be able to integrate this information in the estimation process.

In [RPD09] a general approach to consider different types of constraints on a kernel estimator is proposed. In order to consider this constrained regression estimation method, it is interesting to observe that the estimator

of  $g(\cdot)$  can be written as

$$\hat{g}(\omega|\mathbf{q}) = \sum_{i=1}^n q_i A_i(\omega) y_i \quad (4.22)$$

where the parameters  $q_i = 1/n$  ( $i = 1, 2, \dots, n$ ) and

$$A_i(\omega) = \frac{nK_h(\omega - \omega_i)}{\sum_{j=1}^n K_h(\omega - \omega_j)} \quad (4.23)$$

lead to the unconstrained Nadaraya-Watson kernel estimator of Section 4.3.1. At this point, it is easy to see that when  $q_i \neq 1/n$  for some  $i$ , we attribute more or less importance to some of the samples  $y_i$ , yielding a constrained Nadaraya-Watson kernel estimator. The next part of this section considers some specific constraints applied to our estimation problem.

### Constraints on $g(\omega)$

If our purpose is to impose some constraints on the non linearity of the form

$$g_1(\omega) \leq g(\omega) \leq g_2(\omega) \quad (4.24)$$

then we would have

$$g_1(\omega) \leq \sum_{i=1}^n q_i A_i(\omega) y_i \leq g_2(\omega) \quad (4.25)$$

Considering the  $\mathbf{L}_2$  metric between the parameters  $q_i$  and  $1/n$  (unconstrained case) as in [RPD09], the constrained kernel density estimator can be written as

$$\tilde{\mathbf{q}} = \underset{\mathbf{q}}{\operatorname{argmin}} D(\mathbf{q}) \quad (4.26)$$

where

$$D(\mathbf{q}) = \sum_{i=1}^n \left( \frac{1}{n} - q_i \right)^2 \quad (4.27)$$

$$\sum_{i=1}^n q_i = 1, \quad -1 \leq q_i \leq 1 \quad (4.28)$$

$$g_1(\omega) \leq \sum_{i=1}^n q_i A_i(\omega) y_i \leq g_2(\omega) \quad (4.29)$$

This is a quadratic programming problem that can be conveniently written as (see *quadprog* function in Matlab):

$$\tilde{\mathbf{q}} = \underset{\mathbf{q}}{\operatorname{argmin}} (\mathbf{q}_u - \mathbf{q})^T (\mathbf{q}_u - \mathbf{q}) = \underset{\mathbf{q}}{\operatorname{argmin}} \frac{1}{2} \mathbf{q}^T \mathbf{q} - \mathbf{q}_u^T \mathbf{q} \quad (4.30)$$

$$\sum_{i=1}^n q_i = 1, \quad -1 \leq q_i \leq 1 \quad (4.31)$$

$$\sum_{i=1}^n \tilde{q}_i A_i(\omega) y_i \leq g_2(\omega) \quad (4.32)$$

$$-\sum_{i=1}^n \tilde{q}_i A_i(\omega) y_i \leq -g_1(\omega) \quad (4.33)$$

where  $\mathbf{q}_u$  is an  $n \times 1$  vector whose components are equal to  $1/n$ . Figure 4.20 shows an example of application of the constrained estimator for synthetic data. The method called PM1 is based on (4.14) while PM1C is the constrained version.

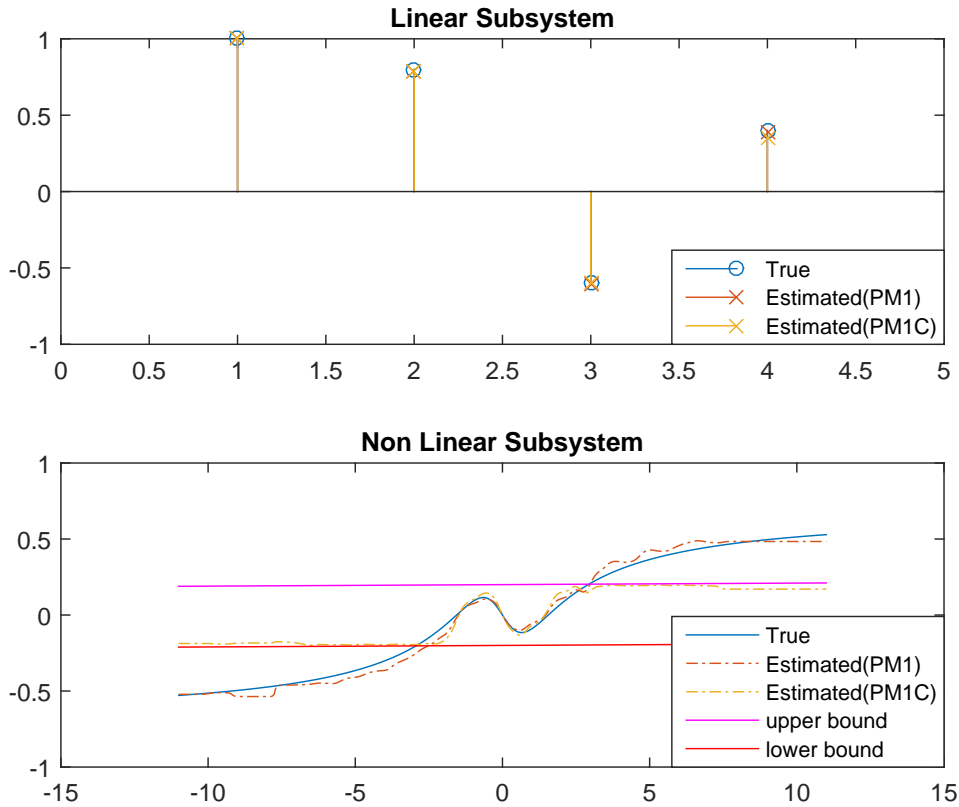


Figure 4.20.: Estimated linear and nonlinear subsystems from the synthetic data of Fig. 4.4 considering a constrained kernel estimator. PM1C (yellow) is the constrained version.

**Constraints on  $g^{(s)}(\omega)$** 

In this section we use the notation  $g^{(s)}(\omega) = \frac{\partial g^s(\omega)}{\partial \omega^s}$ , such that, e.g., for  $s = 1$ , we have  $g^{(1)}(\omega) = \frac{\partial g(\omega)}{\partial \omega}$ . With this notation, the estimator of  $g^{(s)}(\cdot)$  can be written as

$$\hat{g}^{(s)}(\omega|q) = \sum_{i=1}^n q_i A_i^{(s)}(\omega) y_i \quad (4.34)$$

where

$$A_i^{(s)}(\omega) = \frac{\partial A_i^s(\omega)}{\partial \omega^s}. \quad (4.35)$$

As an example, for  $s = 1$ , we have  $A_i^{(1)}(\omega) = \frac{\partial A_i(\omega)}{\partial \omega}$ . At this point, we can express our restrictions as follows

$$l(\omega) \leq \sum_{i=1}^n q_i \left[ \sum_{s \in \mathbf{S}} \alpha_s A_i^{(s)}(\omega) \right] y_i \leq u(\omega) \quad (4.36)$$

where  $\alpha_s$  is a set of positive constants used to generate various constraints where  $l(\omega)$  and  $u(\omega)$  are known functions. As an example, for  $s = 1$ , we obtain

$$l(\omega) \leq \sum_{i=1}^n q_i \left[ \alpha_1 \frac{\partial A_i(\omega)}{\partial \omega} \right] y_i \leq u(\omega). \quad (4.37)$$

Moreover, for  $s = 1$  and  $\alpha_1 = 1$  we have

$$l(\omega) \leq \sum_{i=1}^n q_i \left[ \frac{\partial A_i(\omega)}{\partial \omega} \right] y_i \leq u(\omega). \quad (4.38)$$

For a Gaussian kernel of the type (as in [PHW07])

$$K_h(\omega, \omega_i) = \exp\left(-\frac{(\omega - \omega_i)^2}{2h^2}\right) \quad (4.39)$$

straightforward computations lead to

$$\frac{\partial A_i(\omega)}{\partial \omega} = \frac{\partial}{\partial \omega} \left( \frac{n K_h(\omega, \omega_i)}{\sum_{j=1}^n K_h(\omega, \omega_j)} \right) \quad (4.40)$$

$$= \frac{n}{h^2} \left( \frac{-(\omega - \omega_i) K_h(\omega, \omega_i) \sum_{j=1}^n K_h(\omega, \omega_j) + K_h(\omega, \omega_i) \sum_{j=1}^n (\omega - \omega_j) K_h(\omega, \omega_j)}{(\sum_{j=1}^n K_h(\omega, \omega_j))^2} \right) \quad (4.41)$$

$$= - \left( \frac{\omega - \omega_i}{h^2} \right) A_i(\omega) + A_i(\omega) \frac{\sum_{j=1}^n \left( \frac{\omega - \omega_j}{h^2} \right) K_h(\omega, \omega_j)}{\sum_{j=1}^n K_h(\omega, \omega_j)}. \quad (4.42)$$

Thus, the constraints on the first derivative of  $g(\omega)$  can be rewritten as

$$\sum_{i=1}^n \tilde{q}_i \left( \frac{\partial A_i(\omega)}{\partial \omega} \right) y_i \leq u(\omega) \quad (4.43)$$

$$-\sum_{i=1}^n \tilde{q}_i \left( \frac{\partial A_i(\omega)}{\partial \omega} \right) y_i \leq -l(\omega). \quad (4.44)$$

In Figure 4.21 we can see an example of application on synthetic data considering only bounds on the first derivative of the nonlinear characteristic.

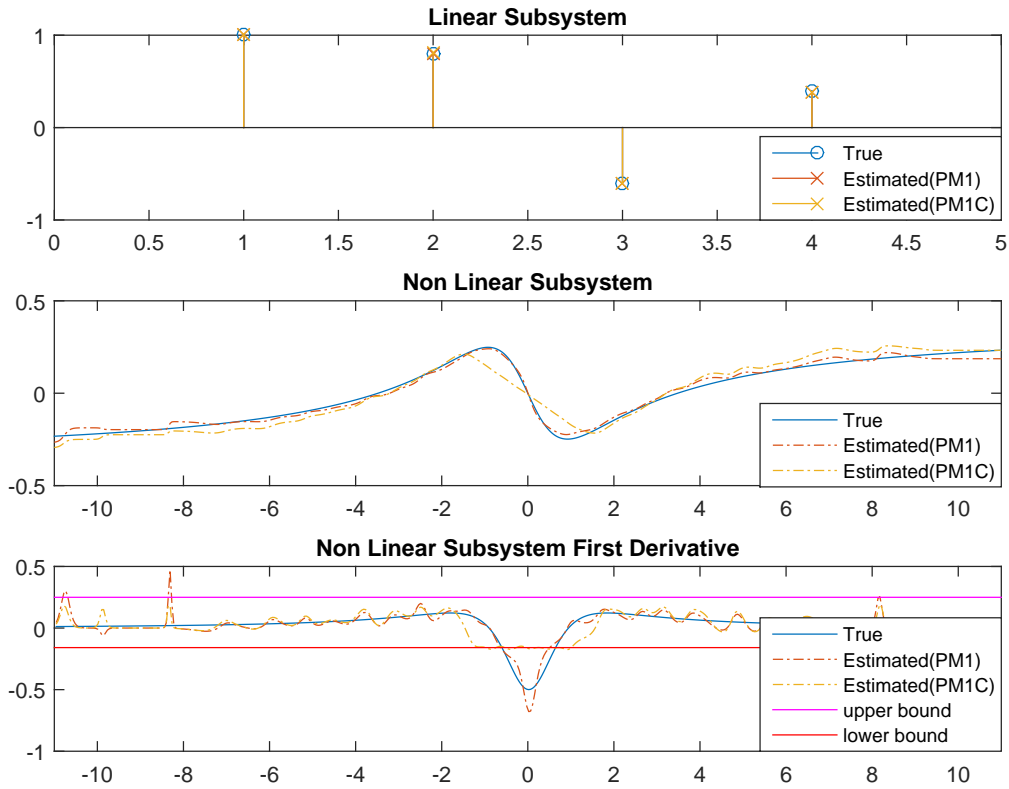


Figure 4.21.: Example of constrained kernel estimator considering bounds on the first derivative of the nonlinear characteristic. PM1C (yellow) is the constrained version.

It is clear that the constrained estimator introduced in Section 4.3.3 can be used to add multiple constraints on the unknown function  $g(\omega)$ . In Figure 4.22 an example of application is shown considering bounds on both the shape and the first derivative of the nonlinear characteristic.

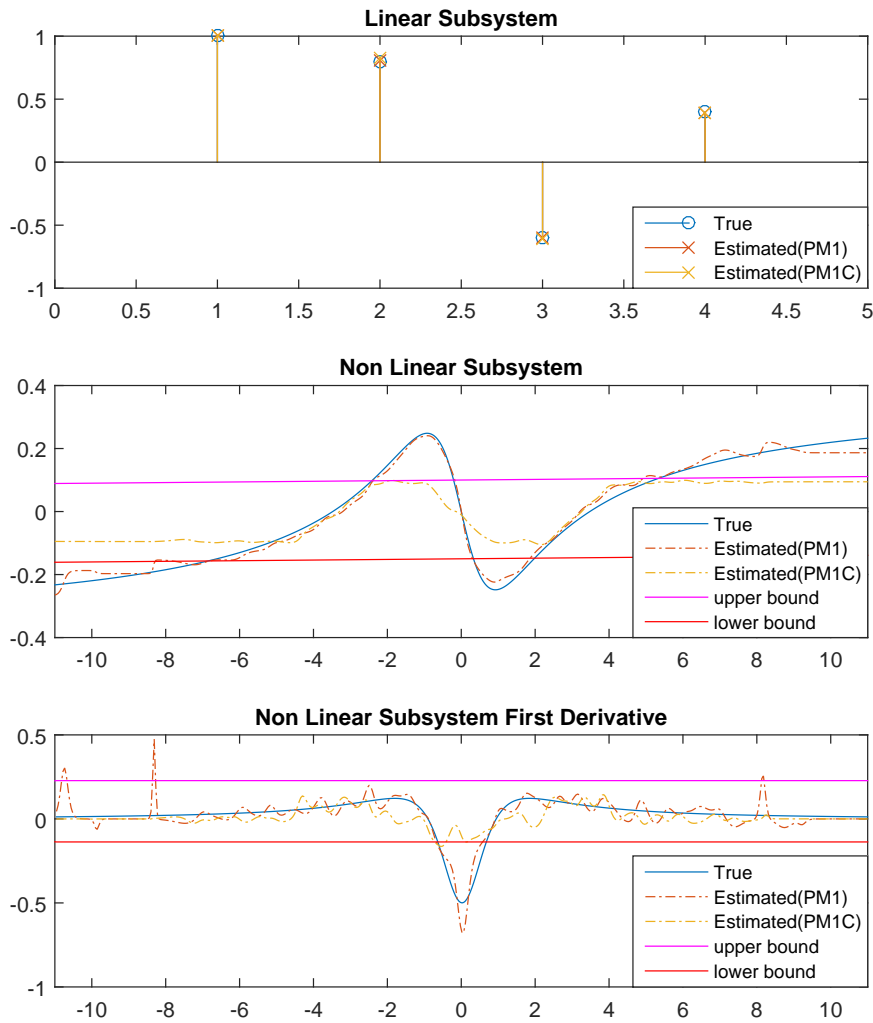


Figure 4.22.: Example of constrained kernel estimator considering bounds on the shape and the first derivative of the nonlinear characteristic. PM1C (yellow) is the constrained version.

The same approach can be used on the algorithm introduced in Section 4.3.2 for hysteresis nonlinearity. Figure 4.23 shows some results obtained with bounds on the first derivative of the hysteresis cycle.

The previous sections generalized Pawlak’s method for hysteresis estimation (see Section 4.3.2) and studied a variant accounting for constraints on the nonlinearity shape or its derivatives (see Section 4.3.3). The next section studies another approach to the problem of Wiener system identification that is based on the maximum likelihood estimator [Urb+19]. The idea is to exploit the fact that in many applications the input signal  $\mathbf{x}$  is not a sequence of i.i.d. random variables, which may be a problem for Pawlak’s method.

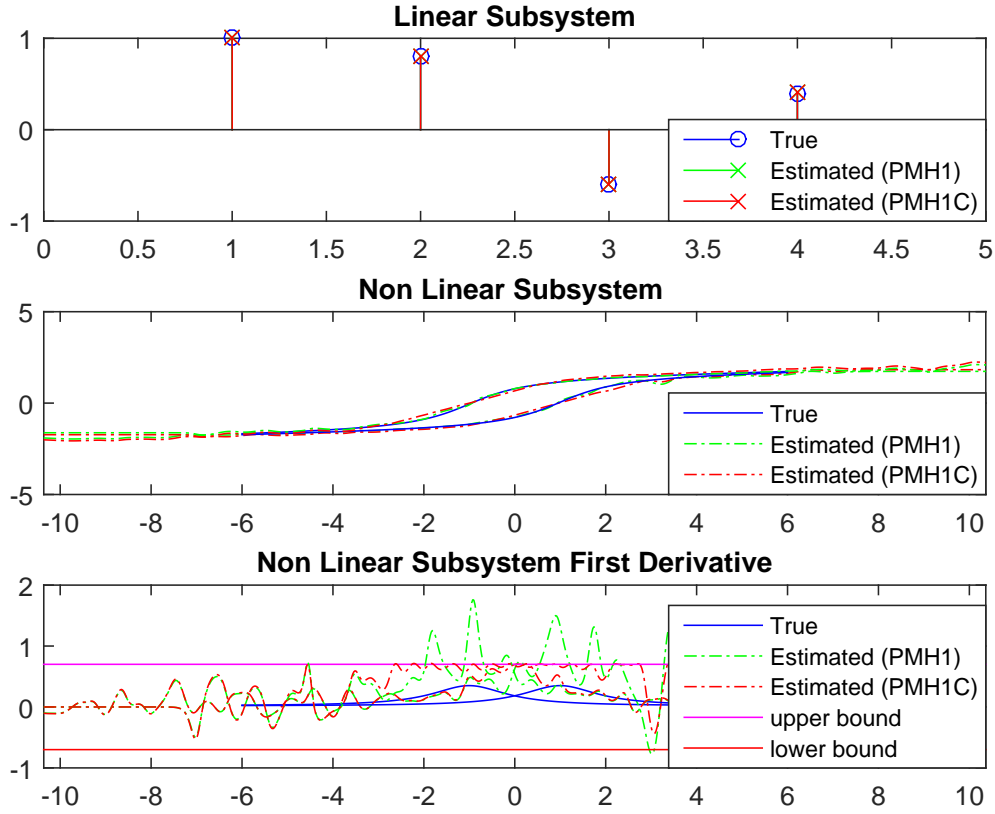


Figure 4.23.: Example of constrained kernel estimator considering bounds on the first derivative of the nonlinear characteristic (Hysteresis type). PMH1C (red) is the constrained version.

#### 4.4. Parametric estimation

In many applications, the input signal of the Nonlinear Wiener Model (NWM) is not a sequence of i.i.d. random variables, but rather a deterministic time series, and the noise sequence is simply an additive i.i.d. Gaussian noise with zero mean and finite but unknown variance  $\sigma_z^2$ . In the next sections we will see that the nonparametric kernel regression estimation of the nonlinear function  $g(\cdot)$  proposed in [PHW07], i.e., the Nadaraya-Watson kernel estimator [WJ94], can also be regarded as a parametric estimator, which is associated with the Gaussian conditional observation model [SN90b][Ott+93]. Indeed, it amounts to estimating a parameter vector  $\gamma$  associated with a given nonparametric kernel estimator of the nonlinearity  $g(\cdot)$ , as well as the weights  $\lambda$  associated with the filter relating  $x_n$  and  $\omega_n$  and the unknown noise variance  $\sigma_z^2$ .

By using the well-known Slepian-Bangs formula [Kay93], we will derive the deterministic Cramér-Rao (CR) bound (CRB) for the NWM parameters, i.e.,  $\gamma$ ,  $\lambda$  and  $\sigma_z^2$ . Furthermore, we will also derive an asymptotic CR-like bound on the global mean squared error (MSE) of the estimated nonlinearity  $g(\cdot; \gamma)$  for consistent and locally unbiased estimators of  $\gamma$ . An interesting property of this bound is its relation with the MISE criterion introduced in [PHW07]. Since we consider a conditional signal model, the maximum likeli-

hood estimator (MLE) of the NWM parameters have variances converging to the corresponding CRBs at high signal-to-noise-ratio (SNR) [Ren+06]. Therefore we derive the associated MLEs and compare their performance with the estimators proposed in [PHW07] (based on the Nadaraya-Watson kernel estimator), which are shown to be sub-optimal when the input signal  $x_n$  is not stationary. We introduce the following notations:  $\mathbf{y} = (y_1, \dots, y_N)^T$ ,  $\boldsymbol{\omega} = (\omega_1, \dots, \omega_N)^T$ ,  $\mathbf{g}(\boldsymbol{\omega}) = (g(\omega_1), \dots, g(\omega_N))^T$ ,  $\mathbf{z} = (z_1, \dots, z_N)^T$ ,  $\mathbf{x} = (x_1, \dots, x_N)^T$ ,  $\underline{\mathbf{x}} = ((x_{1-P}, \dots, x_0), \mathbf{x}^T)^T$ , and

$$\mathbf{T}_{\underline{\mathbf{x}}} = \begin{bmatrix} x_0 & \dots & x_{1-P} \\ \vdots & \vdots & \vdots \\ x_{N-1} & \dots & x_{N-P} \end{bmatrix}$$

where  $\mathbf{y}, \boldsymbol{\omega}, \mathbf{g}(\boldsymbol{\omega}), \mathbf{z}, \mathbf{x} \in \mathbb{R}^N$ ,  $\underline{\mathbf{x}} \in \mathbb{R}^{N+P}$ ,  $\mathbf{T}_{\underline{\mathbf{x}}} \in \mathbb{R}^{N \times P}$ . The nonparametric kernel regression estimation proposed in [PHW07], based on the Nadaraya-Watson kernel estimator of the nonlinearity  $g(\cdot)$  [WJ94], is defined as

$$\begin{aligned} \hat{g}(\omega) &= \hat{g}(\omega; \hat{\boldsymbol{\lambda}}), \quad \hat{g}(\omega; \boldsymbol{\lambda}) = \frac{\sum_{i \in \mathcal{I}_1} y_i K_h(\omega - \omega_i(\boldsymbol{\lambda}))}{\sum_{i \in \mathcal{I}_1} K_h(\omega - \omega_i(\boldsymbol{\lambda}))}, \\ K_h(\omega) &= \frac{K(\frac{\omega}{h})}{h}, \quad \hat{\boldsymbol{\lambda}} = \arg \min_{\boldsymbol{\lambda}} \left\{ \sum_{n \in \mathcal{I}_2} (y_n - \hat{g}(\omega_n(\boldsymbol{\lambda}); \boldsymbol{\lambda}))^2 \right\}, \end{aligned} \quad (4.45)$$

where  $\omega_j(\boldsymbol{\lambda}) = x_j + \sum_{p=1}^P \lambda_p x_{j-p}$ ,  $N = \text{card}(\mathcal{I}_1) + \text{card}(\mathcal{I}_2) + 2P$  and  $K(\omega)$  is a positive symmetric function (kernel) such that

$$\int_{-\infty}^{\infty} K_h(\omega) d\omega = \int_{-\infty}^{\infty} K(u) du = 1. \quad (4.46)$$

Let  $\mathcal{G}_I(\boldsymbol{\gamma})$  be the set of parametric functions  $g(\cdot; \boldsymbol{\gamma})$  defined as

$$g(\omega; \boldsymbol{\gamma}) = \frac{\sum_{i=1}^I \alpha_i K_h(\omega - \beta_i)}{\sum_{i=1}^I K_h(\omega - \beta_i)}, \quad \boldsymbol{\gamma} = \begin{pmatrix} \boldsymbol{\alpha} \\ \boldsymbol{\beta} \end{pmatrix} \in \mathbb{R}^{2I}. \quad (4.47)$$

From a broader perspective, (4.45) can also be regarded as an estimator of  $g(\cdot; \boldsymbol{\gamma})$  defined in (4.47) where  $I = \text{card}(\mathcal{I}_1)$ ,  $\hat{\alpha}_i = y_i$ ,  $\hat{\beta}_i = \omega_i(\hat{\boldsymbol{\lambda}})$ . Therefore the nonparametric kernel regression estimation of the nonlinearity  $g(\cdot)$  defined in (4.45) can be recast as a parametric estimation problem. The observation model (4.13) can be rewritten as follows

$$z_n = y_n - g\left(x_n + \sum_{p=1}^P \lambda_p x_{n-p}\right), \quad 1 \leq n \leq N.$$

If  $\underline{\mathbf{x}}$  is a known deterministic vector, the pdf of  $\mathbf{y}$  conditionally on  $\underline{\mathbf{x}}$  with parameters  $\boldsymbol{\lambda} \in \mathbb{R}^P$  is

$$p(\mathbf{y}|\underline{\mathbf{x}}; \boldsymbol{\lambda}) = p_{\mathbf{z}}(\mathbf{y} - \mathbf{g}(\mathbf{x} + \mathbf{T}_{\underline{\mathbf{x}}}\boldsymbol{\lambda})). \quad (4.48)$$

If  $p_{\mathbf{z}}(\mathbf{z})$  depends on a vector of unknown deterministic parameters  $\boldsymbol{\mu}$ , then  $p_{\mathbf{z}}(\mathbf{z}) \triangleq p_{\mathbf{z}}(\mathbf{z}; \boldsymbol{\mu})$  and (4.48) becomes

$$p(\mathbf{y}|\underline{\mathbf{x}}; \boldsymbol{\lambda}, \boldsymbol{\mu}) = p_{\mathbf{z}}(\mathbf{y} - \mathbf{g}(\mathbf{x} + \mathbf{T}_{\underline{\mathbf{x}}}\boldsymbol{\lambda}); \boldsymbol{\mu}). \quad (4.49)$$

At this point, if  $g(\cdot) \triangleq g(\cdot; \boldsymbol{\gamma}) \in \mathcal{G}_I(\boldsymbol{\gamma})$  and if we consider  $\boldsymbol{\theta}^T = (\boldsymbol{\mu}^T, \boldsymbol{\lambda}^T, \boldsymbol{\gamma}^T)$ , then (4.49) becomes

$$p(\mathbf{y}|\underline{\mathbf{x}}; \boldsymbol{\theta}) = p_{\mathbf{z}}(\mathbf{y} - \mathbf{g}(\mathbf{x} + \mathbf{T}_{\underline{\mathbf{x}}}\boldsymbol{\lambda}; \boldsymbol{\gamma}); \boldsymbol{\mu}) \quad (4.50)$$

where  $g(\cdot; \boldsymbol{\gamma})$  is an unknown parametric deterministic function.

Finally, if  $\mathbf{z} \sim \mathcal{N}(\mathbf{0}, \sigma_z^2 \mathbf{I}_N)$  then (4.50) is a Gaussian pdf as well and thus (4.13) defines a Gaussian conditional observation model.

#### 4.4.1. Deterministic Cramér-Rao bounds

The general theory about lower bounds on the MSE of estimators of deterministic parameters is detailed in [Cha+08, Section II & III][TT10] (and summarized in [Kba+17, Section II]). In particular, if  $\underline{\mathbf{x}}$  is a known deterministic vector, the inverse CRB of  $\boldsymbol{\theta}$  is [Kay93]

$$\mathbf{CRB}_{\boldsymbol{\theta}}^{-1}(\underline{\mathbf{x}}) = \mathbf{F}_{\boldsymbol{\theta}}(\underline{\mathbf{x}}) = -E_{\mathbf{y}|\underline{\mathbf{x}}; \boldsymbol{\theta}} \left[ \frac{\partial^2 \ln p(\mathbf{y}|\underline{\mathbf{x}}; \boldsymbol{\theta})}{\partial \boldsymbol{\theta} \partial \boldsymbol{\theta}^T} \right] \quad (4.51)$$

where  $\mathbf{F}_{\boldsymbol{\theta}}(\underline{\mathbf{x}})$  is the Fisher information matrix (FIM). Under the hypothesis that  $\mathbf{y} \triangleq \mathbf{y}|\underline{\mathbf{x}} \sim \mathcal{N}(\mathbf{m}(\boldsymbol{\theta}), \mathbf{C}(\boldsymbol{\theta}))$ , the FIM (4.51) is obtained from the Slepian-Bangs formula [Kay93, (3.31)]

$$(\mathbf{F}_{\boldsymbol{\theta}})_{i,j} = \frac{\partial \mathbf{m}(\boldsymbol{\theta})^T}{\partial \theta_i} \mathbf{C}(\boldsymbol{\theta})^{-1} \frac{\partial \mathbf{m}(\boldsymbol{\theta})}{\partial \theta_j} + \frac{1}{2} \text{tr} \left( \mathbf{C}(\boldsymbol{\theta})^{-1} \frac{\partial \mathbf{C}(\boldsymbol{\theta})}{\partial \theta_i} \mathbf{C}(\boldsymbol{\theta})^{-1} \frac{\partial \mathbf{C}(\boldsymbol{\theta})}{\partial \theta_j} \right). \quad (4.52)$$

In the Gaussian case considered in this work,  $\boldsymbol{\theta}^T = (\sigma_z^2, \boldsymbol{\lambda}^T, \boldsymbol{\gamma}^T)$ ,  $\mathbf{C}(\boldsymbol{\theta}) = \sigma_z^2 \mathbf{I}_N$  and  $\mathbf{m}(\boldsymbol{\theta}) = \mathbf{g}(\mathbf{x} + \mathbf{T}_{\underline{\mathbf{x}}}\boldsymbol{\lambda}; \boldsymbol{\gamma})$ .

As a consequence, the FIM of  $\boldsymbol{\theta}$  is

$$\mathbf{F}_{\boldsymbol{\theta}}(\underline{\mathbf{x}}) = \begin{bmatrix} \frac{1}{2} \frac{N}{\sigma_z^4} & \mathbf{0} & \mathbf{0} \\ \mathbf{0} & \mathbf{F}_{\boldsymbol{\lambda}}(\underline{\mathbf{x}}) & \mathbf{F}_{\boldsymbol{\lambda}, \boldsymbol{\gamma}}(\underline{\mathbf{x}}) \\ \mathbf{0} & \mathbf{F}_{\boldsymbol{\lambda}, \boldsymbol{\gamma}}^T(\underline{\mathbf{x}}) & \mathbf{F}_{\boldsymbol{\gamma}}(\underline{\mathbf{x}}) \end{bmatrix}$$

where

$$\begin{aligned}\mathbf{F}_\lambda(\underline{\mathbf{x}}) &= \frac{1}{\sigma_z^2} \left( \frac{\partial \mathbf{g}(\underline{\mathbf{x}} + \mathbf{T}_x \boldsymbol{\lambda}; \boldsymbol{\gamma})}{\partial \boldsymbol{\lambda}^T} \right)^T \frac{\partial \mathbf{g}(\underline{\mathbf{x}} + \mathbf{T}_x \boldsymbol{\lambda}; \boldsymbol{\gamma})}{\partial \boldsymbol{\lambda}^T} \\ \mathbf{F}_\gamma(\underline{\mathbf{x}}) &= \frac{1}{\sigma_z^2} \left( \frac{\partial \mathbf{g}(\underline{\mathbf{x}} + \mathbf{T}_x \boldsymbol{\lambda}; \boldsymbol{\gamma})}{\partial \boldsymbol{\gamma}^T} \right)^T \frac{\partial \mathbf{g}(\underline{\mathbf{x}} + \mathbf{T}_x \boldsymbol{\lambda}; \boldsymbol{\gamma})}{\partial \boldsymbol{\gamma}^T} \\ \mathbf{F}_{\lambda, \gamma}(\underline{\mathbf{x}}) &= \frac{1}{\sigma_z^2} \left( \frac{\partial \mathbf{g}(\underline{\mathbf{x}} + \mathbf{T}_x \boldsymbol{\lambda}; \boldsymbol{\gamma})}{\partial \boldsymbol{\lambda}^T} \right)^T \frac{\partial \mathbf{g}(\underline{\mathbf{x}} + \mathbf{T}_x \boldsymbol{\lambda}; \boldsymbol{\gamma})}{\partial \boldsymbol{\gamma}^T}\end{aligned}$$

which leads to

$$\begin{aligned}\mathbf{CRB}_\lambda^{-1}(\underline{\mathbf{x}}) &= \mathbf{F}_\lambda(\underline{\mathbf{x}}) - \mathbf{F}_{\lambda, \gamma}(\underline{\mathbf{x}}) \mathbf{F}_\gamma^{-1}(\underline{\mathbf{x}}) \mathbf{F}_{\lambda, \gamma}^T(\underline{\mathbf{x}}) \\ \mathbf{CRB}_\gamma^{-1}(\underline{\mathbf{x}}) &= \mathbf{F}_\gamma(\underline{\mathbf{x}}) - \mathbf{F}_{\lambda, \gamma}^T(\underline{\mathbf{x}}) \mathbf{F}_\lambda^{-1}(\underline{\mathbf{x}}) \mathbf{F}_{\lambda, \gamma}(\underline{\mathbf{x}}).\end{aligned}\tag{4.53}$$

With a few additional computations, it is easy to show that

$$\begin{aligned}\frac{\partial \mathbf{g}(\underline{\mathbf{x}} + \mathbf{T}_x \boldsymbol{\lambda}; \boldsymbol{\gamma})}{\partial \boldsymbol{\lambda}^T} &= \left( \frac{\partial \mathbf{g}(\underline{\mathbf{x}} + \mathbf{T}_x \boldsymbol{\lambda}; \boldsymbol{\gamma})}{\partial \omega} \mathbf{1}_P^T \right) \odot \mathbf{T}_x \\ \frac{\partial g(\omega; \boldsymbol{\gamma})}{\partial \alpha_{i'}} &= \frac{K_h(\omega - \beta_{i'})}{\sum_{i=1}^I K_h(\omega - \beta_i)} \\ \frac{\partial g(\omega; \boldsymbol{\gamma})}{\partial \beta_{i'}} &= K_h^{(1)}(\omega - \beta_{i'}) \frac{\sum_{i=1}^I (\alpha_i - \alpha_{i'}) K_h(\omega - \beta_i)}{\left( \sum_{i=1}^I K_h(\omega - \beta_i) \right)^2}\end{aligned}$$

where  $\odot$  denotes the Hadamard product,  $\mathbf{1}_P^T = (1, \dots, 1) \in \mathbb{R}^P$ ,  $K_h^{(1)}(\omega) = \partial K_h(\omega) / \partial \omega$  and

$$\frac{\partial g(\omega; \boldsymbol{\gamma})}{\partial \omega} = \frac{\sum_{i=1}^I \alpha_i K_h^{(1)}(\omega - \beta_i)}{\sum_{i=1}^I K_h(\omega - \beta_i)} - \frac{\sum_{i=1}^I K_h^{(1)}(\omega - \beta_i)}{\sum_{i=1}^I K_h(\omega - \beta_i)} g(\omega; \boldsymbol{\gamma}).$$

#### 4.4.2. A lower bound on the global estimation error

The quality of the estimation of  $g(\cdot; \boldsymbol{\gamma}) \in \mathcal{G}_I(\boldsymbol{\gamma})$  based on the estimator  $g(\cdot; \hat{\boldsymbol{\gamma}})$  can be measured via the global estimation error

$$\|g(\cdot; \boldsymbol{\gamma}) - g(\cdot; \hat{\boldsymbol{\gamma}})\|^2 = \int_{\Omega} (g(\omega; \boldsymbol{\gamma}) - g(\omega; \hat{\boldsymbol{\gamma}}))^2 d\omega.\tag{4.54}$$

From a theoretical point of view, (4.54) is a random variable whose distribution is difficult to determine in the general case. As a consequence, we consider a simpler performance criterion, i.e., its mean value which equals the global MSE defined as

$$\mathcal{C}(\boldsymbol{\gamma}, \hat{\boldsymbol{\gamma}}) = E_{\mathbf{y}|\underline{\mathbf{x}}; \boldsymbol{\theta}} \left[ \|g(\cdot; \boldsymbol{\gamma}) - g(\cdot; \hat{\boldsymbol{\gamma}})\|^2 \right] = \int_{\Omega} E_{\mathbf{y}|\underline{\mathbf{x}}; \boldsymbol{\theta}} \left[ (g(\omega; \boldsymbol{\gamma}) - g(\omega; \hat{\boldsymbol{\gamma}}))^2 \right] d\omega.\tag{4.55}$$

It is interesting to note that  $\mathcal{C}(\gamma, \hat{\gamma})$  in (4.55) is the limiting value for  $T, L \rightarrow \infty$  of the MISE performance criterion [PHW07, (28)] (weak law of large numbers)

$$MISE(\hat{g}(\cdot)) = \frac{1}{LT} \sum_{l=1}^L \|\mathbf{g}(\omega_T; \gamma) - \mathbf{g}(\omega_T; \hat{\gamma}_l)\|^2 \quad (4.56)$$

where  $L$  is the number of independent observations,  $\Omega = [a, b]$  is the compact interval containing the possible values of  $\omega$  ( $\omega_t = a + \frac{b-a}{T}(t-1)$ ), and  $\mathbf{g}(\omega_T; \gamma') = (g(\omega_1; \gamma'), \dots, g(\omega_T; \gamma'))^T$ . Under the assumption that  $\hat{\gamma} \triangleq \hat{\gamma}(\mathbf{y}|\mathbf{x})$  is a consistent estimator of  $\gamma$ , i.e., provided that  $\hat{\gamma} = \gamma + d\hat{\gamma}$  with  $d\hat{\gamma}^T d\hat{\gamma} \rightarrow 0$  when  $\sigma_z^2 \rightarrow 0$ , then  $g(\omega; \hat{\gamma}) - g(\omega; \gamma) \rightarrow \frac{\partial g(\omega; \gamma)}{\partial \gamma^T} d\hat{\gamma}$  when  $\sigma_z^2 \rightarrow 0$  leading to

$$\mathcal{C}(\gamma, \hat{\gamma}) \xrightarrow{\sigma_z^2 \rightarrow 0} \int_{\Omega} \frac{\partial g(\omega; \gamma)}{\partial \gamma^T} \mathbf{C}_{d\hat{\gamma}}(\mathbf{x}) \frac{\partial g(\omega; \gamma)}{\partial \gamma} d\omega = \text{tr} \left( \mathbf{C}_{d\hat{\gamma}}(\mathbf{x}) \int_{\Omega} \frac{\partial g(\omega; \gamma)}{\partial \gamma} \frac{\partial g(\omega; \gamma)}{\partial \gamma^T} d\omega \right).$$

Moreover, if  $\hat{\gamma}$  is a locally unbiased estimator of  $\gamma$ , then  $\mathbf{C}_{d\hat{\gamma}}(\mathbf{x}) \geq \mathbf{CRB}_{\gamma}(\mathbf{x})$  [Kay93] (in the sense that the difference between the two matrices is positive) and

$$\frac{\partial g(\omega; \gamma)}{\partial \gamma^T} \mathbf{C}_{d\hat{\gamma}}(\mathbf{x}) \frac{\partial g(\omega; \gamma)}{\partial \gamma} \geq \frac{\partial g(\omega; \gamma)}{\partial \gamma^T} \mathbf{CRB}_{\gamma}(\mathbf{x}) \frac{\partial g(\omega; \gamma)}{\partial \gamma}$$

which allows us to define the following CR-like bound

$$\mathcal{C}(\gamma, \hat{\gamma}) \geq \text{tr} \left( \mathbf{CRB}_{\gamma}(\mathbf{x}) \int_{\Omega} \frac{\partial g(\omega; \gamma)}{\partial \gamma} \frac{\partial g(\omega; \gamma)}{\partial \gamma^T} d\omega \right). \quad (4.57)$$

#### 4.4.3. Maximum Likelihood estimator

When  $g(\cdot)$  is an unknown parametric deterministic function, i.e.,  $g(\cdot) \triangleq g(\cdot; \gamma) \in \mathcal{G}_I(\gamma)$ , the analysis can be conducted by rewriting (4.13) as

$$y_n = \sum_{i'=1}^I \left( \frac{K_h(\omega_n(\boldsymbol{\lambda}) - \beta_{i'})}{\sum_{i=1}^I K_h(\omega_n(\boldsymbol{\lambda}) - \beta_i)} \right) \alpha_{i'} + z_n$$

which leads to the well known conditional Gaussian linear model [SN90b][Ott+93][Kay93]

$$\mathbf{y} = \mathbf{H}_{\mathbf{x}}(\boldsymbol{\beta}, \boldsymbol{\lambda}) \boldsymbol{\alpha} + \mathbf{z}, \quad \mathbf{H}_{\mathbf{x}}(\boldsymbol{\beta}, \boldsymbol{\lambda}) = \frac{\partial \mathbf{g}(\mathbf{x} + \mathbf{T}_{\mathbf{x}} \boldsymbol{\lambda}; \gamma)}{\partial \boldsymbol{\alpha}^T}, \quad (4.58)$$

for which the MLE of  $\boldsymbol{\theta}^T = (\sigma_z^2, \boldsymbol{\lambda}^T, \boldsymbol{\gamma}^T)$  is

$$\begin{aligned}\widehat{\sigma}_z^2(\mathbf{y}|\mathbf{x}) &= \frac{1}{N} \left\| \mathbf{y} - \mathbf{H}_{\mathbf{x}}(\widehat{\boldsymbol{\beta}}, \widehat{\boldsymbol{\lambda}}) \widehat{\boldsymbol{\alpha}} \right\|^2 \\ (\widehat{\boldsymbol{\alpha}}, \widehat{\boldsymbol{\beta}}, \widehat{\boldsymbol{\lambda}})(\mathbf{y}|\mathbf{x}) &= \arg \min_{\boldsymbol{\alpha}, \boldsymbol{\beta}, \boldsymbol{\lambda}} \left\{ \frac{1}{N} \left\| \mathbf{y} - \mathbf{H}_{\mathbf{x}}(\boldsymbol{\beta}, \boldsymbol{\lambda}) \boldsymbol{\alpha} \right\|^2 \right\}.\end{aligned}\quad (4.59)$$

Straightforward computations lead to [SN90b][Ott+93][Kay93]:

$$\widehat{\boldsymbol{\alpha}}(\mathbf{y}|\mathbf{x}) = \left( \mathbf{H}_{\mathbf{x}}(\boldsymbol{\beta}, \boldsymbol{\lambda})^T \mathbf{H}_{\mathbf{x}}(\boldsymbol{\beta}, \boldsymbol{\lambda}) \right)^{-1} \mathbf{H}_{\mathbf{x}}(\boldsymbol{\beta}, \boldsymbol{\lambda})^T \mathbf{y} \quad (4.60)$$

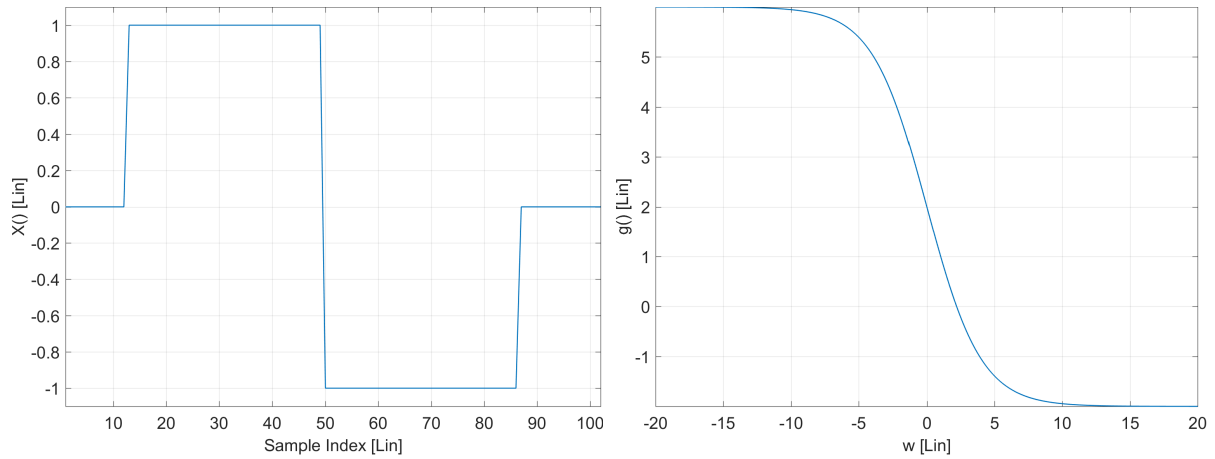
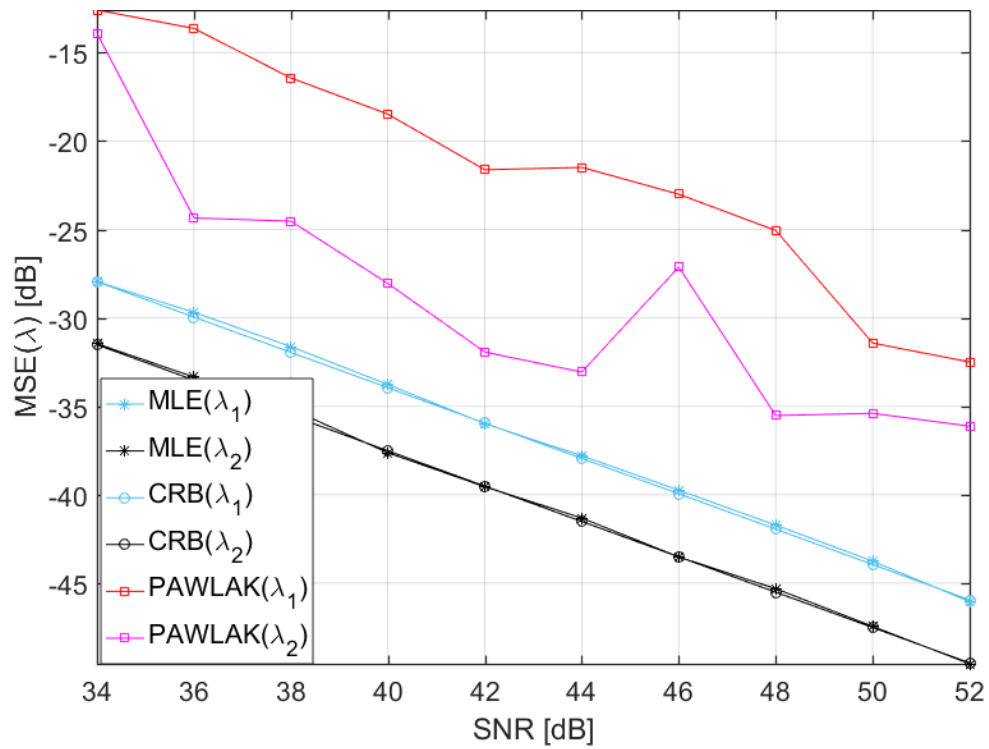
$$(\widehat{\boldsymbol{\beta}}, \widehat{\boldsymbol{\lambda}})(\mathbf{y}|\mathbf{x}) = \arg \max_{\boldsymbol{\beta}, \boldsymbol{\lambda}} \left\{ \mathbf{y}^T \boldsymbol{\Pi}_{\mathbf{H}_{\mathbf{x}}(\boldsymbol{\beta}, \boldsymbol{\lambda})} \mathbf{y} \right\}. \quad (4.61)$$

We can observe that the MLE of  $\boldsymbol{\alpha}$  (4.60) is different from the Nadaraya-Watson kernel estimator (4.45) [PHW07, (11)]. In [Ren+06] it is shown that when  $\sigma_z^2 \rightarrow 0$ , the MLEs  $(\widehat{\boldsymbol{\alpha}}, \widehat{\boldsymbol{\beta}}, \widehat{\boldsymbol{\lambda}})(\mathbf{y}|\mathbf{x})$  (4.60-4.61) are consistent, Gaussian, locally unbiased and efficient (minimum variance). As a consequence, when  $\sigma_z^2 \rightarrow 0$ , for a given pair  $(\widehat{\boldsymbol{\beta}}, \widehat{\boldsymbol{\lambda}})(\mathbf{y}|\mathbf{x})$ , (4.45)[PHW07, (11)] leads likely to a biased estimator which is sub-optimal (in the MSE sense) compared to the MLE (4.60). In a nutshell, the following results can be obtained asymptotically (when  $\sigma_z^2 \rightarrow 0$ ): (i) the proposed MLEs  $(\widehat{\boldsymbol{\alpha}}, \widehat{\boldsymbol{\beta}}, \widehat{\boldsymbol{\lambda}})(\mathbf{y}|\mathbf{x})$  are efficient; (ii)  $g(\cdot; \widehat{\boldsymbol{\gamma}}(\mathbf{y}|\mathbf{x}))$  reaches (4.57).

To summarize the MLE of the unknown parameters can be determined by solving the optimization problem (4.61) with respect to  $\boldsymbol{\beta}$  and  $\boldsymbol{\lambda}$  and then to estimate the unknown parameters  $\sigma_z^2$  and  $\boldsymbol{\alpha}$  using (4.59) and (4.60).

### Example on synthetic data

We consider a synthetic scenario based on a pulse wave input signal  $\mathbf{x}$  as displayed in Fig. 4.24 ( $N = 100$ ), and a dynamical system defined by  $\boldsymbol{\lambda} = (1/2, 1/2)^T$ ,  $\boldsymbol{\alpha} = (6, -2)^T$ ,  $\boldsymbol{\beta} = (-1/4, 1/4)^T$ . A Gaussian kernel with bandwidth  $h = 1$  is considered. The nonlinearity  $g(\cdot)$  resulting from this choice is shown in Fig. 4.24, where  $\Omega = [a, b] = [-20, 20]$  and  $T = 800$ . Note that all the results presented in this section have been obtained by averaging  $L = 5000$  Monte Carlo runs. In Fig. 4.25 and 4.26 we compare the MSE of the MLEs (4.60-4.61) to the CRBs (4.53) as a function of the SNR defined as  $SNR = \left( \frac{1}{N} \left\| \mathbf{g}(\mathbf{x} + \mathbf{T}_{\mathbf{x}} \boldsymbol{\lambda}; \boldsymbol{\gamma}) \right\|^2 \right) / \sigma_z^2$ . Fig. 4.25 also compares the performance of two estimators of  $\boldsymbol{\lambda}$ , i.e., the MLE defined in (4.61) and Pawlak's estimator defined in (4.45) where  $\text{card}(\mathcal{I}_1) = 51$  and  $\text{card}(\mathcal{I}_2) = 47$ . We can observe that the MLEs (4.60-4.61) converge to the CRBs (4.53) when the SNR increases, as expected [Ren+06]. Moreover, we can note that the MLE outperforms the kernel estimator of  $g(\cdot)$  proposed in [PHW07]. Fig. 4.27 displays the estimated global estimation error, i.e.,  $MISE(\widehat{g}(\cdot))$ , of the two estimators versus SNR, which is compared with the proposed CR-like bound (4.57). As already mentioned for the estimation of  $\boldsymbol{\lambda}$ , the global estimation error of the MLE converges to the bound and outperforms the kernel estimator(4.45)[PHW07]. These observations are confirmed in Fig. 4.28 showing the estimator of the nonlinearity  $g(\cdot)$  in both cases (for a given SNR), with a biased kernel estimator, as anticipated.

Figure 4.24.: Input signal  $x$  (left) and non linearity  $g(\cdot)$  (right)Figure 4.25.: MSEs of the MLE (4.61) and of Pawlak's estimator (4.45) for  $\lambda$  versus SNR, and the corresponding CRB( $\lambda$ ) (4.53).

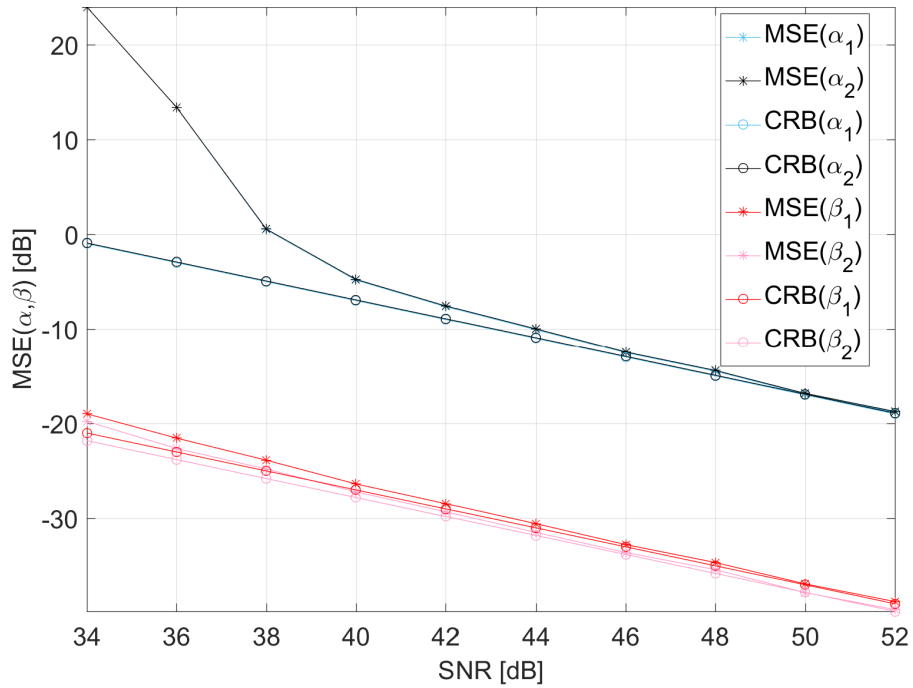


Figure 4.26.: MSE of the MLEs of  $(\alpha, \beta)$  (4.60-4.61) versus SNR, and the corresponding  $\text{CRB}(\alpha, \beta)$  (4.53).

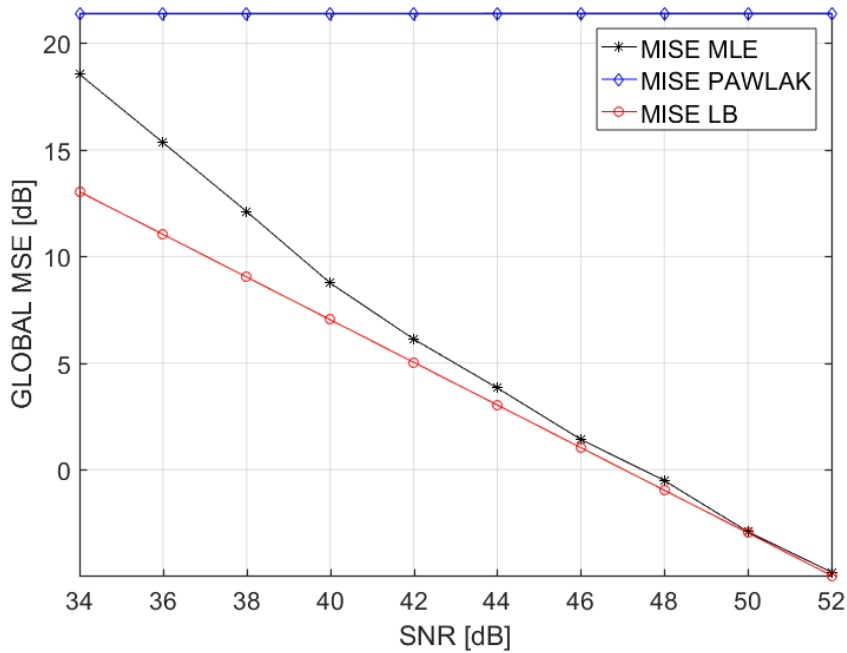


Figure 4.27.:  $MISE(\hat{g}(\cdot))$  (4.56) of the MLE (4.60-4.61) and of Pawlak's estimator (4.45) versus SNR, compared with the lower bound (4.57).

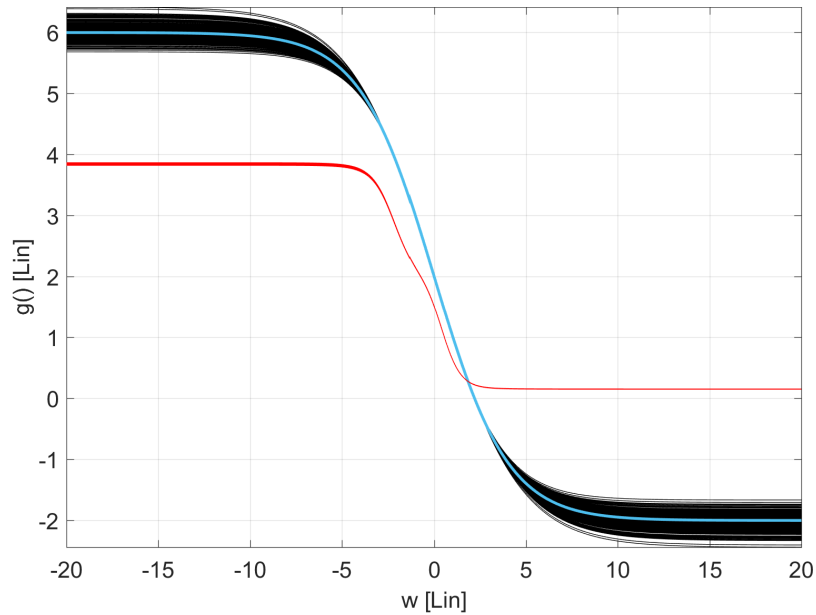


Figure 4.28.: Estimated nonlinearity  $\hat{g}(\cdot)$  obtained with the MLEs (4.60-4.61, in black) and Pawlak's estimators (4.45, in red) of  $(\lambda, \alpha, \beta)$ , compared to the ground truth  $g(\cdot)$  (in blue) at  $SNR = 52dB$ .

## 4.5. Conclusions and Perspectives

This chapter addressed the problem of Wiener model identification for free play estimation. The main contributions are the proposed variants to Pawlak's method [PHW07] (hysteresis cycle estimation and constrained kernel regression) and the derivation of the deterministic CRBs, the MLE and an asymptotic CR-like bound for the global estimation error of the estimated nonlinearity. Furthermore, some simulation results confirmed that the maximum likelihood estimator of the nonlinearity has a global estimation error closer to the corresponding Cramér-Rao bound when compared to Pawlak's estimator [PHW07] (when the input is not stationary and the additive noise is Gaussian). Based on the obtained results, further studies can be carried out to

- evaluate the optimal input signal for Wiener system identification
- evaluate the influence of the bandwidth parameter  $h$  and the kernel type on the MLE performance
- adapt the MLE to hysteresis cycle estimation and constrained estimation
- evaluate the sensitivity of the MLE to its initialization.



# 5

## Industrial Validation

### Contents

---

<b>5.1. Introduction</b> . . . . .	<b>85</b>
<b>5.2. LCO diagnostic</b> . . . . .	<b>87</b>
5.2.1. Example of LCO detection . . . . .	88
5.2.2. Simulation Results . . . . .	89
5.2.3. Experimental results . . . . .	94
<b>5.3. Freeplay diagnostic</b> . . . . .	<b>96</b>
5.3.1. Example of freeplay detection . . . . .	97
5.3.2. Simulation results . . . . .	98
5.3.3. Experimental results . . . . .	100

---

### 5.1. Introduction

This chapter presents the industrial validation of the most promising methods (from an industrial point of view) proposed in Chapter 3 and Chapter 4. In particular, from Chapter 3 we have selected two very simple detectors for LCO detection and diagnosis, the ones described in Figures 3.7 and 3.9. The choice of these detectors is mainly based on the limited computational capacity currently available in the EFCS computers. From Chapter 4 we have decided to test the modified version of Pawlak’s method for hysteresis nonlinearity, as described in Section 4.3.2, for freeplay detection and diagnosis. The choice of this detector is mainly related to the industrial constraints already mentioned in Sections 2.5 and 2.6. Based on the current hardware of in-series aircraft, one of the best solution that can be proposed for LCO **condition monitoring** is an hybrid approach: a simple real-time on-board LCO detector based on the command and control surface position (RVDT), plus an offline freeplay detector based on the rod and control surface positions (LVDT and RVDT, see Figure 2.3). This approach is interesting because the two algorithms are complementary and their combination represents a more robust and powerful method for LCO detection and diagnostic. For example in Table 5.1 the logic table for LCO troubleshooting is presented for a generic C/S (active/standby scheme as in Figure 2.8). It can be seen that the isolation of the LCO cause can be achieved by mixing the information from the two algorithms and monitoring only the active actuator control loop (the reader may refer to Figures 2.3 and 2.8 to recall the control architecture of the C/S).

Table 5.1.: LCO troubleshooting on a C/S as in Figure 2.8 (active/passive scheme).

Troubleshooting table	case 1	case 2	case 3	case 4
Vibration detection	1	1	0	0
Freeplay detection	1	0	1	0
Component to inspect	active actuator	standby actuator	active actuator	none

The on-board hardware capacity imposes very stringent constraints in terms of computational burden. Thus, the general form of the GLRT is tricky to implement. However, thanks to a few very reasonable hypothesis (LCO bandwidth is known and LCO amplitude is “small”) the detector described in Figures 3.7 and 3.9 can be used. Thanks to their simplicity these detectors can be easily rewritten with an auto recursive scheme. Moreover, the Goertzel algorithm (see Appendix A.5) can be used for the computation of the periodograms to reduce even more the computational burden.

Concerning the method for freeplay detection and diagnosis, we assume that the freeplay induces an hysteresis cycle between the LVDT and RVDT measurements. Thus the method described in Section 2.6 is the most suitable. Furthermore, considering an offline application, the freeplay detector is affected by less hardware and robustness constraints. Indeed, the method can be directly implemented on a dedicated mean on ground (without the need for any simplification or approximation).

It is important to remember that, for both LCO and freeplay diagnostic, the final goal is to generate a **condition monitoring signal (Figure 5.1)** that can be communicated to the airlines in order to avoid unscheduled (really expensive) maintenance task.

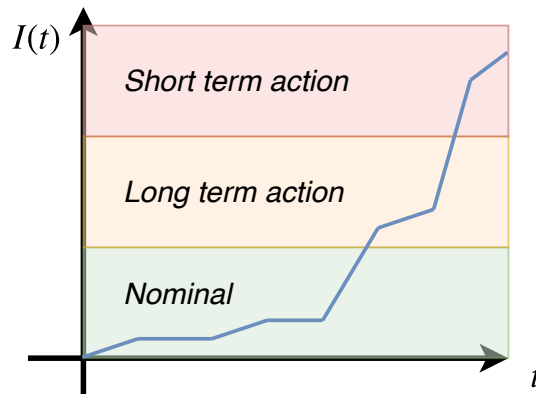


Figure 5.1.: Example of condition monitoring signal.

In the next sections the results obtained on simulated and experimental data applying the proposed methods will be presented.

## 5.2. LCO diagnostic

The idea is to detect and diagnose the LCO using a GLR test and then to estimate the amplitude and duration of the oscillation to derive a condition monitoring signal [Urb+18a]. Indeed, knowing the status and trend of the LCO energy, one can estimate the degradation of the system due to LCO (wear process) and finally propose to the airlines a maintenance action on the short or long term.

### Condition monitoring signal

The GLRT defined in Chapter 3 implicitly involves the estimation of the LCO amplitude  $\hat{A} = \sqrt{\hat{l}_1^2 + \hat{l}_2^2}$  and duration<sup>1</sup>  $\widehat{\Delta T}$  (see Section 3.8). This means that we can estimate the energy produced by the vibration as

$$\hat{E}_{\text{LCO}} = \int_{\widehat{\Delta T}} \hat{A}^2 dt.$$

Based on this observation, a very simple method for vibration diagnostic can be proposed. Indeed, if we consider that only a fraction of  $E_{\text{LCO}}$  is dissipated through wear process<sup>2</sup> that increases the freeplay level, we can define a simple diagnostic index  $I$  (for a given flight  $F$ ) as

$$I(F) = k_w \int_{\widehat{\Delta T}_F} \hat{A}_F^2 dt$$

where  $k_w$  is a wear severity coefficient. At this point, this definition of  $I$  can be easily extended to  $n$  flights by considering a recursive expression of the type

$$I(F_n) = \lambda_f I(F_{n-1}) + k_w \int_{\widehat{\Delta T}_{F_n}} \hat{A}_{F_n}^2 dt \quad (5.1)$$

where  $\lambda_f$  is a forgetting factor adjusted to reduce the undesired effects of estimation errors. The vibration diagnostic signal (5.1) provides a rough estimate of the system deterioration due to vibrations (freeplay increase) and thus it can be used for diagnostic purpose on a control surface. However, it is important to observe that the simple expression (5.1) has to be coupled with a relevant threshold to be meaningful, which may be a tricky task. Indeed, one can choose to link empirically the index  $I$  with an acceptable level of cabin and cockpit comfort. However, this concept may vary between pilots and airlines. For this reason, from now we will focus only on the estimation accuracy in terms of LCO amplitude and duration, leaving the computation of  $I$  and the associated threshold tuning to further studies. Note also that the parameters  $k_w$  and  $\lambda_f$  may be considered as time-varying for a more accurate prediction of the vibration evolution.

<sup>1</sup>The signal is detected in  $M$  observation windows of dimension  $N$ . If  $T_s$  denotes the sampling period, we can approximate the duration as  $\widehat{\Delta T} = MNT_s$ .

<sup>2</sup>Concerning the interaction between wear process and limit cycle oscillations, the reader can find an interesting description in [SKA02].

### 5.2.1. Example of LCO detection

Fig. 5.2 (top) shows the input and the output of the actuator control loop of the Control Surface (C/S) of an Airbus aircraft. Having only the command for the actuator from the flight control laws (signal  $\mathbf{x}$ ) and the measured position of the C/S (signal  $\mathbf{y}$ ), the objective is to detect the possible presence of an undesired oscillation on the measured position. Note that one cannot guarantee a priori that the frequency of the anomaly is not superimposed with the bandwidth of the known signal  $\mathbf{x}$ . Thus, we need to determine whether the oscillation appearing in the measurement vector  $\mathbf{y}$  is “desired” by the control laws or if it is an anomaly. Considering that the actuator dynamic can be approximated by a signal model of the type  $\lambda x(n-p)$  (where  $p \in \mathbb{R}$  is the delay and  $\lambda \in \mathbb{R}$  the attenuation/amplification induced by the actuator), we can apply directly the test derived in Section 3.8 using sliding non-overlapping windows to detect the presence of a potential anomaly. Fig. 5.2 (bottom) shows the successful detection of the anomalies (undesired oscillations) that correspond to the two undesired resonance peaks affecting the signal  $\mathbf{y}$  (the input signal  $\mathbf{x}$  is a specific chirp signal whose parameters cannot be provided for confidentiality reasons). Note that the detection threshold has been tuned using (3.33) for a constant false alarm rate (e.g., equal to  $10^{-t}$  per flight hour, where  $t \in [3, 6]$ ), considering an observation window tuned to achieve a detection probability close to 1 (in the example of Fig. 5.2 a window of 3 seconds is enough to meet the objective).

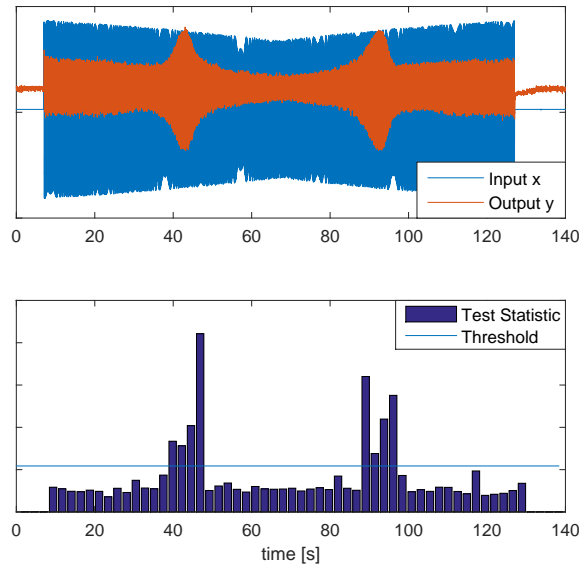


Figure 5.2.: Application of the GLRT for the detection of an undesired oscillation affecting a control surface of a civil aircraft. Please note that for confidentiality reasons the oscillation amplitude is not shown.

The reader should observe that in order not to reduce the reliability of the system under surveillance (e.g., the actuator of a civil aircraft), the false alarm rate of the detection algorithm must be lower than the mean time between failure (MTBF) of the system. Moreover, a given detection probability is always required in order

to comply with the industrial operational constraints to detect the vibrations before it impacts the comfort of the flight. In this context, the performance analysis carried out in chapter 3 is important. Indeed, the MTBF constraint (or equivalently  $P_{FA}$ ) and industrial  $P_D$  constraints can be used to tune directly the detector parameters (threshold and observation window), reducing considerably the time needed to develop and test the new monitoring algorithm. For example, one can choose the threshold directly as  $\gamma = Q_{\chi^2}^{-1}(P_{FA})$  and the observation window length  $N$  in order to obtain a given  $SNR$  (and a specific value of  $P_D$ ).

### 5.2.2. Simulation Results

A Monte Carlo test campaign has been conducted using an industrial Airbus desktop simulator to evaluate the detection performance of the proposed approach. A test set, composed of the signals  $x = \text{Command}$  and  $y = \text{RVDT}$ , has been generated for the elevator of a specific Airbus aircraft that flies on the typical mission profile for that aircraft (see Fig. 5.3) under different operating conditions in terms of Mass, balance, Mach number and turbulence level<sup>3</sup> (see Table 5.2). Various possible operating conditions (around 2500) have been simulated based on the typical profile mission in Fig. 5.3 and a particular combination of the parameters in Table 5.2.

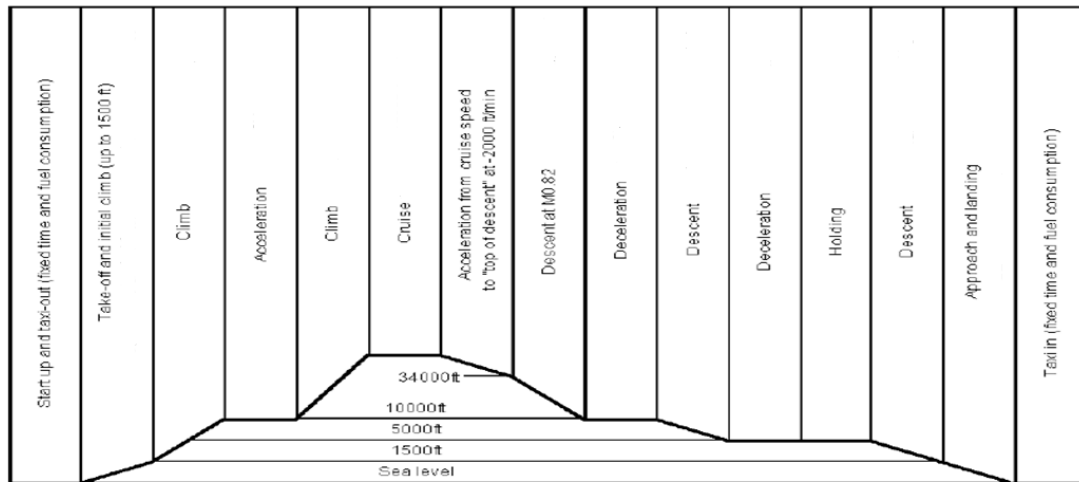


Figure 5.3.: Typical vertical flight path.

<sup>3</sup>The turbulence levels  $T_1 - T_2 - T_3$  are three increasing levels of turbulence (low, medium and strong) assessed with regard to Airbus pilots sensitivity.

Table 5.2.: Considered Operating Conditions.

Parameters	Range
Mass	63-95% Maximum takeoff weight
Balance	20-40%
Mach	0.6-0.8
Turbulence	$T_1 - T_2 - T_3$

A simplified version of the algorithm described in Section 3.8 has been considered for hardware capacity reasons. Indeed, we cannot guarantee the absence of signal power at the frequency  $\hat{f}$  in  $\mathbf{x}$ . However, we can consider that the power of the sinusoid is small compared to the energy and covariance terms  $\mathbf{x}^T(\hat{p})\mathbf{x}(\hat{p})$  and  $\mathbf{x}^T(\hat{p})\mathbf{y}$ , leading to  $\hat{p}_0 \approx \hat{p}_1 \approx \hat{p}$ . In this case, the estimation of the system dynamic  $P$  and the detection of the oscillation  $\mathbf{s}$  can be decoupled reducing the computational cost of the algorithm. In other terms, we have reduced the algorithm to a simple two steps approach of the type estimation plus detection (recursive estimation of the system dynamic for residual generation plus sinusoidal detection on the residuals, Figure 3.9). The system dynamic can be estimated based on the MLEs under  $\mathcal{H}_0$ , while the detection problem reduces to the surveillance of the power spectral density of the residuals. Note that the LCO frequency  $f$  is generally known a priori based on the aeroelastic properties of the system, so the frequency band to be monitored is narrow.

The threshold can be tuned as in Section 3.8.2 for a  $P_{\text{FA}} = 10^{-t}$  for flight hour, where  $t \in [3, 6]$  and  $r = 2$  under the considered hypotheses. Based on (3.33), the observation window has been chosen as the smallest one able to detect a given vibration amplitude  $A_1$  (lower than pilot sensitivity) with  $P_D$  close to one (for the given  $P_{\text{FA}}$ ). A value of 10 seconds has been chosen for the observation window, based on a sampling rate of  $F_s = 100\text{Hz}$ . First, the test set has been analyzed with the aforementioned algorithm in order to verify the robustness of the method (fault-free case). No false alarm was observed. Second, the original test set was modified for performance evaluation. Indeed, the vibrations (frequency  $f$ ) have been artificially added on the signal  $y$  only in the flight phases where the LCO is more likely to trigger on the elevator (e.g., when the hinge moment of the control surface is close to 0, see also Fig. 2.23). In particular, we have considered three target levels  $A_1, A_2$  and  $A_3$  to be detected in this campaign (three target levels corresponding to three cockpit vibration levels: lower than pilot sensitivity  $A_1$ , detectable by the average pilot  $A_2 \approx 1.35A_1$ , possible in-flight turn back  $A_3 \approx 2.2A_1$ , see Fig. 5.4). An example of one of the simulated scenarios for performance evaluation is shown in Fig. 5.5 with the control surface hinge moment. Almost 170 different flight conditions were considered for this specific scenario according to Table 5.2. An auto-recursive Simulink model was chosen to implement the algorithm and to evaluate its performance in terms of detection and estimation capabilities (we want to estimate amplitude and duration for the diagnostic objective as explained in Section 5.2). Fig. 5.6 shows an example of application

of the algorithm for the target amplitude  $A_2$ . We can observe that the vibration is always detected<sup>4</sup>. However, the estimation accuracy in terms of amplitude and duration depends on the particular flight condition (the same is true for the other target amplitudes). In Fig. 5.7 we can observe a bar plot of the mean estimation errors<sup>5</sup> as a function of the target amplitudes  $A_1, A_2, A_3$  and for a low level of turbulence  $T_1$ . It can be seen that the estimation errors are not monotone functions of the amplitude. In Fig. 5.8 we can observe a bar plot of the mean estimation errors as a function of the turbulence level ( $T_1 = \text{low}, T_2 = \text{medium}, T_3 = \text{strong}$ ) for the target amplitude  $A_2$ . As expected, the turbulence acts as an undesired interference for the detector and the estimation performance decreases as the turbulence level increases. It is interesting to observe that, from the analysis of Figs. 5.7 and 5.8, one can also derive a rough estimate of the propagation error on the predictive index in Section 5.2. Indeed, if we consider that  $I(F)/k_w \approx \widehat{\Delta T} \widehat{A}^2$ , assuming no correlation<sup>6</sup>, the propagation error can be estimated as

$$e(I)/k_w \approx \sqrt{e(\widehat{\Delta T})^2 + (2e(\widehat{A}))^2}.$$

Looking for example at Fig. 5.7, for the target level  $A_1$  and  $A_2$ , one would obtain  $e(I)/k_w \approx 27\%$  and  $e(I)/k_w \approx 6\%$ .

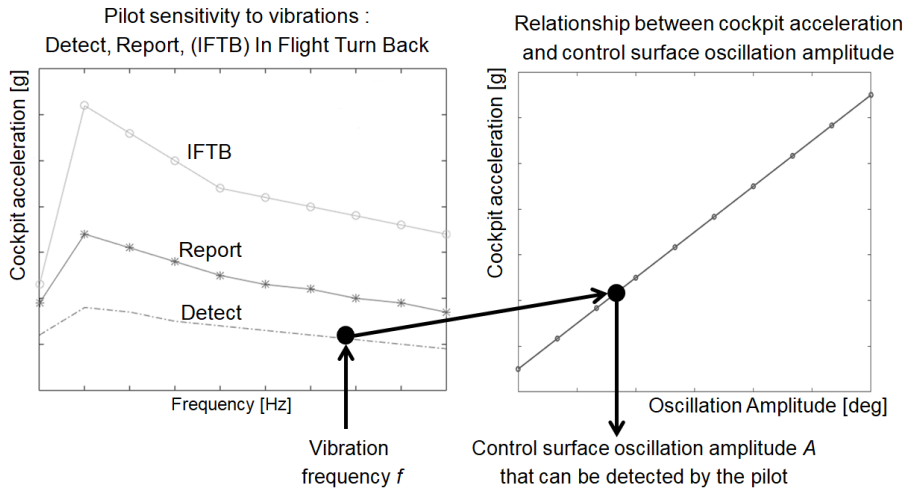


Figure 5.4.: Example of identification for the vibration target level  $A_2$ .

<sup>4</sup>Please note that for industrial confidentiality reasons the real amplitudes are not shown, but the Signal to Noise Ratio (SNR) justifies the use of statistical test as the GLRT.

<sup>5</sup>For a generic flight condition  $n$ , the normalized error is defined as:  $Error(n) = (True\ Value - Estimated\ Value)/True\ Value$ .

<sup>6</sup>only for the purpose of getting a simple estimate even if it is generally not true

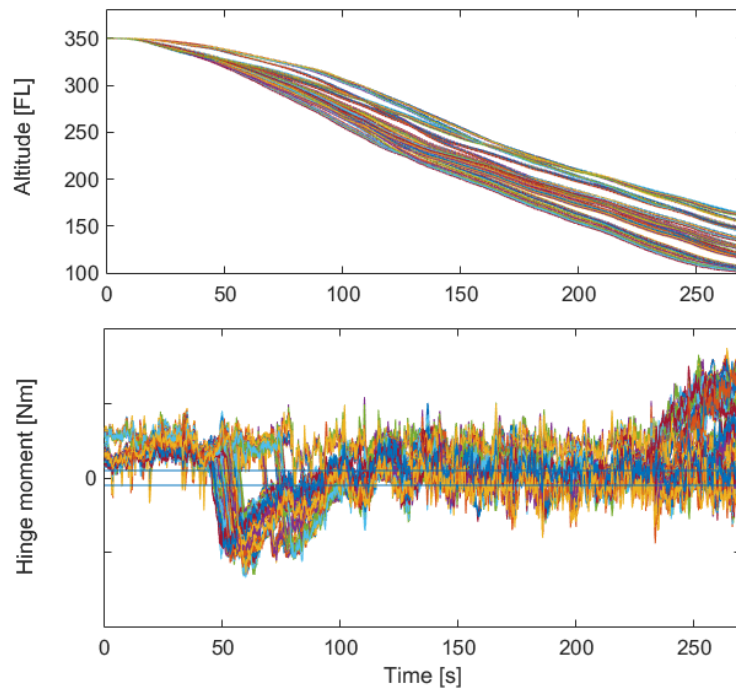


Figure 5.5.: Aircraft descent under different operating conditions: altitude (up) and control surface hinge moment (down). The hinge moment values are hidden for confidentiality reasons.

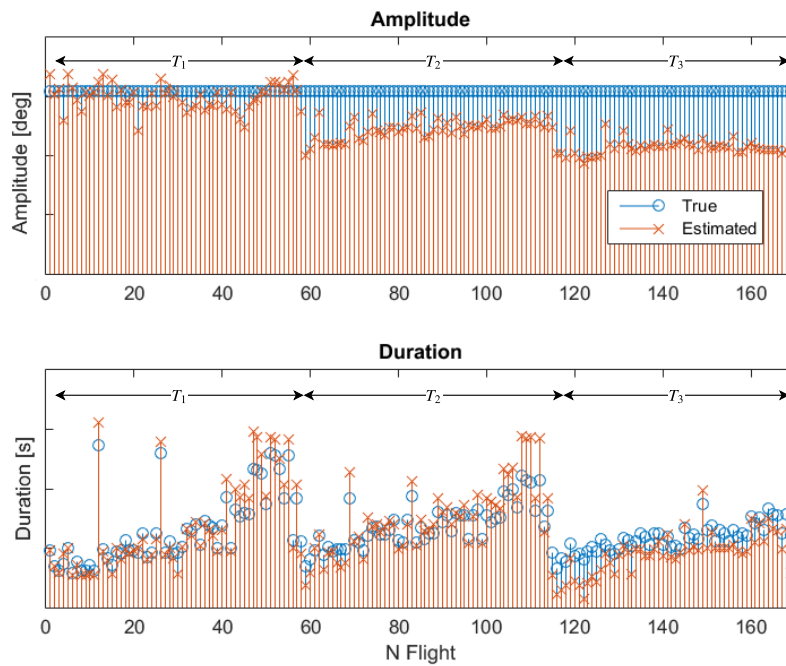


Figure 5.6.: Example of amplitude estimation (up) and duration estimation (down) for the simulated scenario in Fig. 5.5 and the target amplitude  $A_2$ . For 3 levels of turbulence ( $T_1 = \text{low}$ ,  $T_2 = \text{medium}$ ,  $T_3 = \text{strong}$ ).

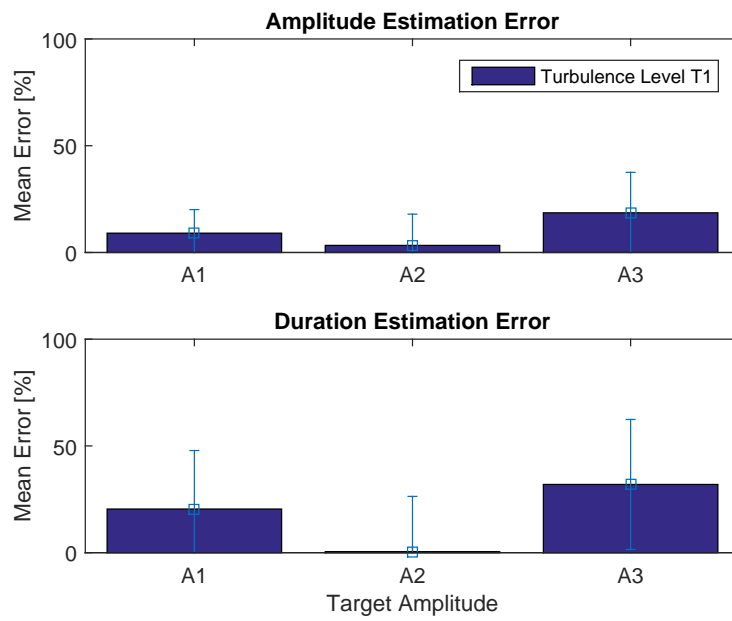


Figure 5.7.: Mean amplitude estimation error (up) and mean duration estimation error (down) for the case in Figure 5.5 as a function of the target amplitude for a low level of turbulence. A  $2\sigma$  error bar is also considered for each mean error.

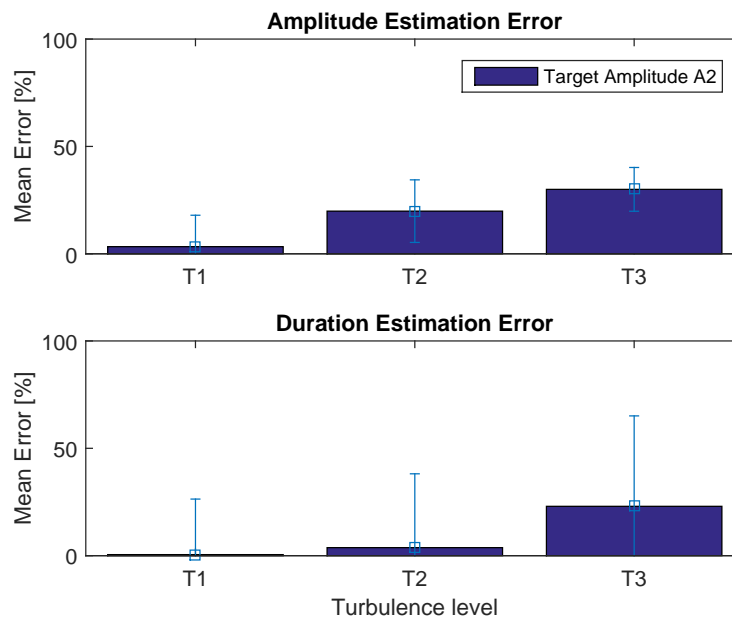


Figure 5.8.: Mean amplitude estimation error (up) and mean duration estimation error (down) for the case in Fig. 5.5 as a function of the turbulence level for the target amplitude  $A_2$ . A  $2\sigma$  error bar is also considered for each mean error.

### 5.2.3. Experimental results

#### Flight data

The vibration detection algorithm has been validated also on real flight data. In Figure 5.9 we can see the test statistic signal (detector of Figure 3.9) compared to the corresponding threshold for about 56 hours of real flight data of an Airbus aircraft. An artificial oscillation at the LCO frequency and  $A_1$  amplitude (pilot sensitivity) has been added on the data ( $\Delta T \approx 20s$ ) in the middle of the dataset, see Figure 5.9) and the algorithm is able to correctly detect and estimate the vibration. No false alarm is observed on the considered dataset. The threshold has been tuned as already explained in section 5.2.2 for a given  $P_{FA}$ . It is important to mention that, for the considered tuning, the long duration vibration ( $\Delta T > 20s$ ) of amplitude  $A_1$  is correctly detected and estimated, while short duration vibrations of amplitude  $A_1$  ( $\Delta T < 5s$ ) are not detected. However, the missed detection of small amplitude ( $A \leq A_1$ ) and short duration ( $\Delta T < 5s$ ) LCO is not critical for our application. Indeed, the wear process induced by LCO depends from the energy of the vibration. Thus, only long duration ( $\Delta T > 20s$ ) and/or large amplitude ( $A > A_1$ ) LCO is of primary interest.

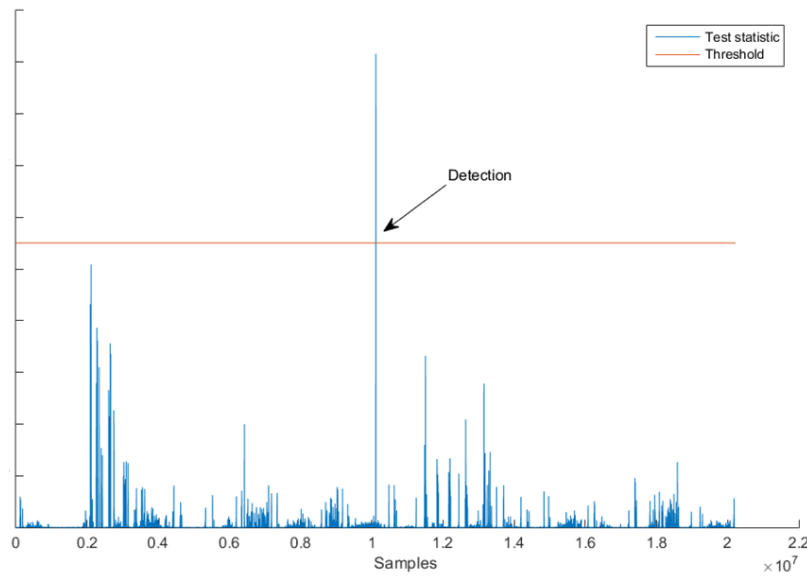


Figure 5.9.: GLR test for the detection of undesired oscillations affecting a C/S of an Airbus aircraft. The test statistic (in comparison to the threshold) is shown. Please note that for confidentiality reasons some data are not shown.

#### Laboratory

The LCO is a rare event and few data are available. Moreover, for a generic flight, we do not know the freeplay level. In this context, a laboratory test with calibrated freeplay levels and induced vibrations is really important to validate the LCO and freeplay detection techniques under investigation in this study.

In 2018 a specific test campaign has been conducted on the elevator test bench of an Airbus aircraft (ground test) to better assess the effectiveness of the proposed condition monitoring algorithm. The schematic of the considered elevator test bench is displayed in Figure 5.10. The considered test bench is a very high fidelity test mean. Indeed, it reproduces with very good fidelity the actuator control loop behavior of the real aircraft. The C/S inertia is represented via a specific shaft that can rotate if the active actuator is moving (active/standby scheme). A torque bar can be used to simulate the real aerodynamic efforts. The hardware components (actuators, sensors, control computers) are the same as on the real aircraft.

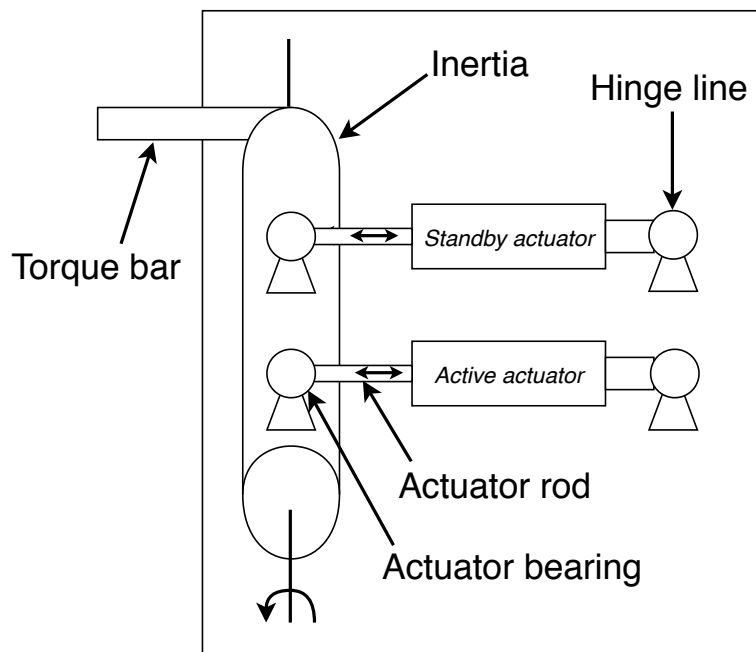


Figure 5.10.: Schematic of the actuator test bench.

An artificial oscillation (representing the LCO) is added to the shaft via the standby actuator and the active actuator control loop is monitored via the detectors described in Figs. 3.7 and 3.9. Different cases have been tested corresponding to different LCO amplitudes and freeplay levels. Figure 5.11 compares the true and estimated oscillation amplitudes for different flight phases, freeplay levels and tuning parameters (observation window). The minimum detectable LCO amplitude is displayed in red in Fig. 5.11. This amplitude is lower than the pilot sensitivity to vibration confirming the applicability of the two algorithms (Figs. 3.7 and 3.9). It can be seen that for the considered amplitudes the algorithms seem to systematically underestimate the real amplitude. The observed underestimation is related to the sliding window implementation of the algorithms. Indeed, the “transient phases” when the oscillation enters in the observation window tend to reduce the average value of the estimated amplitude. A simple way to tackle this problem is to eliminate the transient phases from

the computation of the average estimate of the amplitude.

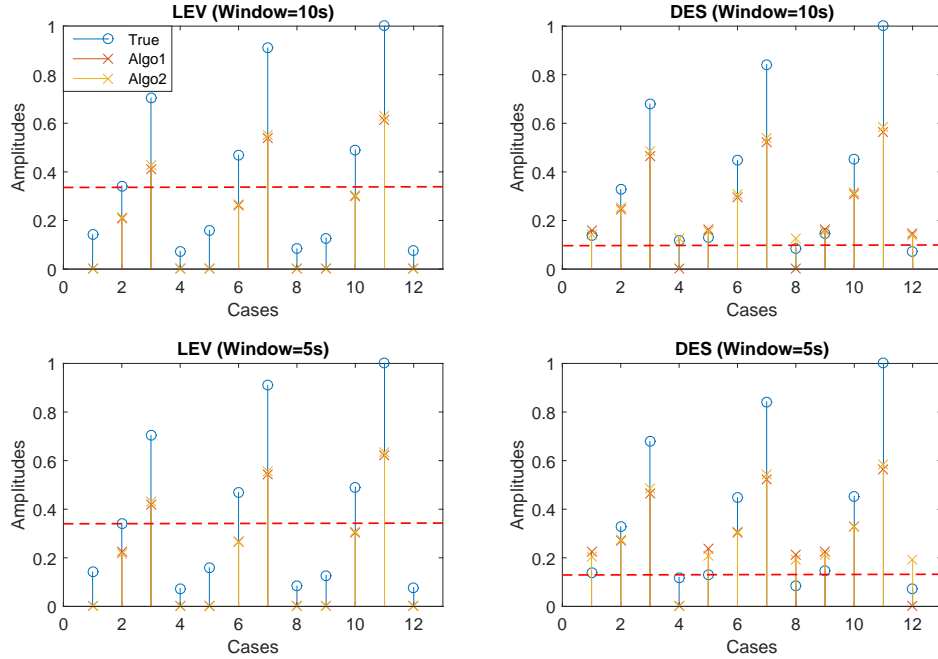


Figure 5.11.: True and estimated oscillation amplitudes for different flight phases and freeplay levels. Two different observation windows are considered. The amplitudes are normalized for confidentiality reasons.

### 5.3. Freeplay diagnostic

Several methods have been studied in Chapter 4 for Wiener model identification and freeplay diagnostic. The nonparametric method (adapted from [PHW07]) presented in Section 4.3.2 is the first one that we have derived and tested. On the other hand, the parametric method (MLE) studied in Section 4.4 is an interesting alternative as it is supposed to provide better results for deterministic input signals. In this section, due to the PhD thesis time constrains and to the more complex initialization of the MLE, we have decided to validate only the nonparametric method from Section 4.3.2, leaving to further studies the validation and comparison with the MLE.

It is important to note that trough the identification of the nonlinearity of the Wiener model at different time instant  $t_i$  one can evaluate the nonlinearity evolution due to the system aging. As a consequence, the freeplay evolution can be related to the nonlinearity evolution and a condition monitoring signal can be computed that is proportional to the freeplay level. A specific procedure can be defined for freeplay diagnostic

1. Data pre-processing (identifiability): select the flight phase and remove artefacts (NaN and outliers).
2. Wiener model identification [PHW07]: data partitioning, linear subsystem identification, non linear subsystem identification (hysteresis), goodness of fit evaluation (NMSE).

3. freeplay level estimation: condition monitoring signal  $I(t)$  computation (at  $t = t_0, t_1, t_2, \dots$ ) for all the actuator servoloops under surveillance.
4. freeplay diagnostic: anomaly isolation, maintenance recommendation.

The condition monitoring signal considered in this section represents a degree of nonlinearity (seen as a deviation from a normal behavior) and it can be computed in different ways. For example, by computing the distance between the current estimate of  $g(\cdot)$  and the estimate of  $g(\cdot)$  from a reference flight or directly by measuring a specific feature of the nonlinearity. If the estimated nonlinearity is of hysteresis type, one can choose to compute the norm and/or the area of the hysteresis cycle (see Section 4.3.2)

$$I(t) = \|\mathbf{g}^+(\omega) - \mathbf{g}^-(\omega)\| \quad \text{or} \quad I(t) = \int (g^+(\omega) - g^-(\omega)) d\omega. \quad (5.2)$$

### 5.3.1. Example of freeplay detection

A real test campaign has been conducted to test the effect of different levels of freeplays on control surface oscillations as LCO. For the purpose of this study we have considered 4 test sets representing 4 flights with different known levels of freeplay. Each test set is composed by the pair LVDT/RVDT of the actuator control loop, corresponding to the actuator rod position and the control surface position. Pawlak's method is applied to generate an estimate of the output nonlinearity of a Wiener model. The reader should observe that the nonlinearity shape is not a priori known, because multiple non linearities exist in the system. However, the different levels of freeplay among the 4 test sets should be visible comparing the 4 estimates. In Figure 5.12 we can see that an hysteresis cycle is estimated in the four cases and we can identify a trend among the flights (with some dispersion).

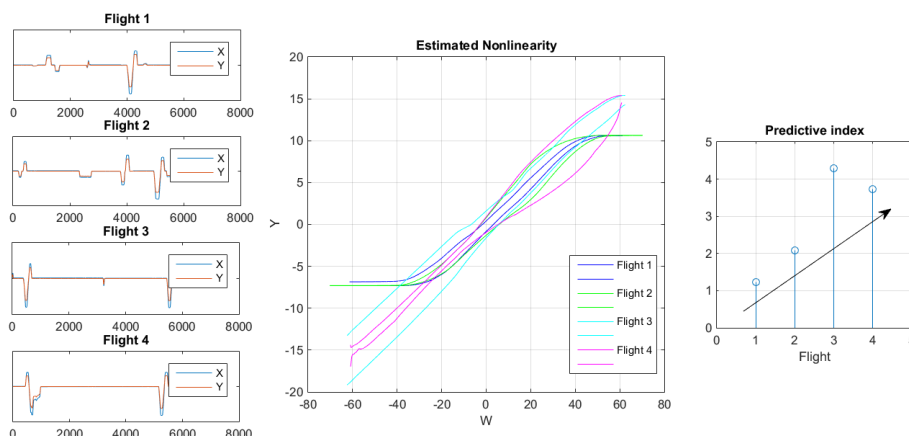


Figure 5.12.: Application to 4 test sets representing 4 flights with increasing known levels of freeplay. The predictive index corresponds to the area of the estimated hysteresis.

In Figure 5.13, repeating the same analysis on 4 different flights from a different aircraft and control surface,

but with no freeplay, we can see that there is a small dispersion among the estimated nonlinearities.

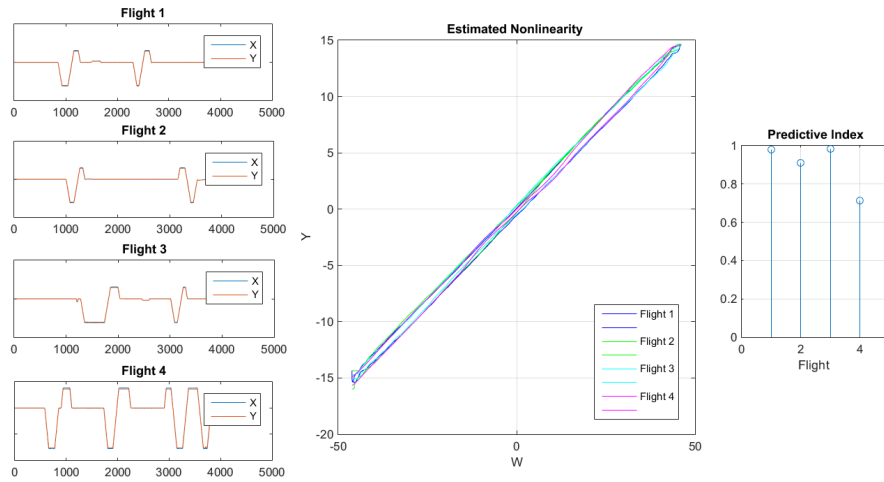


Figure 5.13.: Application to 4 test sets representing 4 flights with no freeplay. The predictive index corresponds to the area of the estimated hysteresis.

Figures 5.13 and 5.12 suggest that the chosen approach could be used for freeplay estimation. It can be seen that the input signals considered in the previous example are not i.i.d. random variables, however, Pawlak's method still provide reasonable results.

### 5.3.2. Simulation results

The proposed solution for freeplay estimation is based on the hypothesis that an increased freeplay between the rod position measure (LVDT) and the control surface position measure (RVDT) leads to a nonlinear behavior similar to an hysteresis cycle. However, in the nominal actuator's operation domain plenty of non linear behaviors may appear that can counterfeit the output of the identification algorithm. Thus, the following question arises: how can we guarantee that the algorithm is robust to other nonlinear behaviors that can be encountered in the actuator's operation domain ?. A first attempt in answering this question has been made based on an Airbus Matlab/Simulink model for the simulation of the actuator/surface behavior. The considered model, numerically and experimentally validated on Airbus aircraft, is able to represent, with reasonable approximation, the actuator response and its interaction with the flight control computers and the control surface (see Figure 5.14). Thirteen different parameters have been considered in a Monte Carlo test campaign to test multiple nonlinear behaviors that can be encountered by the actuator in normal operation. Figure 5.15 summarizes the results of this study. Indeed, representing the norm versus the area of the estimated nonlinearity, a cluster representing the nominal behavior can be observed. On the other hand, when a dead-zone or a backlash are introduced in the system (representing the freeplay) the norm (and the area) of the estimated hysteresis tends to be far from the nominal behavior. Finally, the simulator test campaign confirms the feasibility of the chosen approach and suggests that the area and the norm of the hysteresis are good features for freeplay diagnostic.

For more details about this study the reader may refer to [Car18].

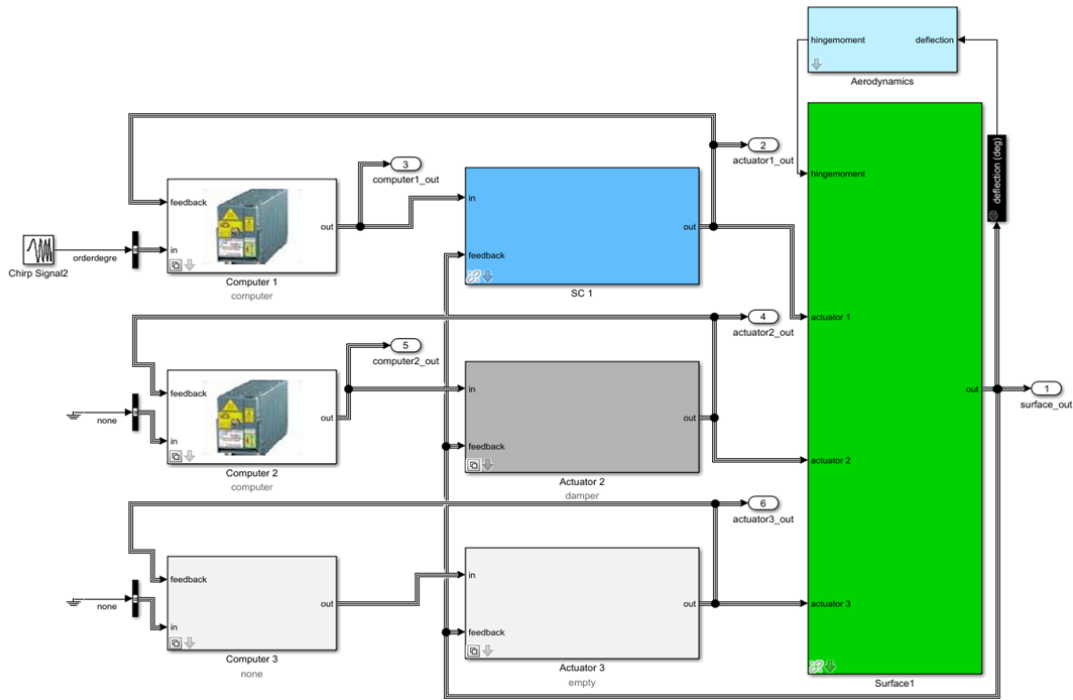


Figure 5.14.: Airbus Simulink/Matlab model used to represent the actuator response and its interaction with the flight control computers and the control surface.

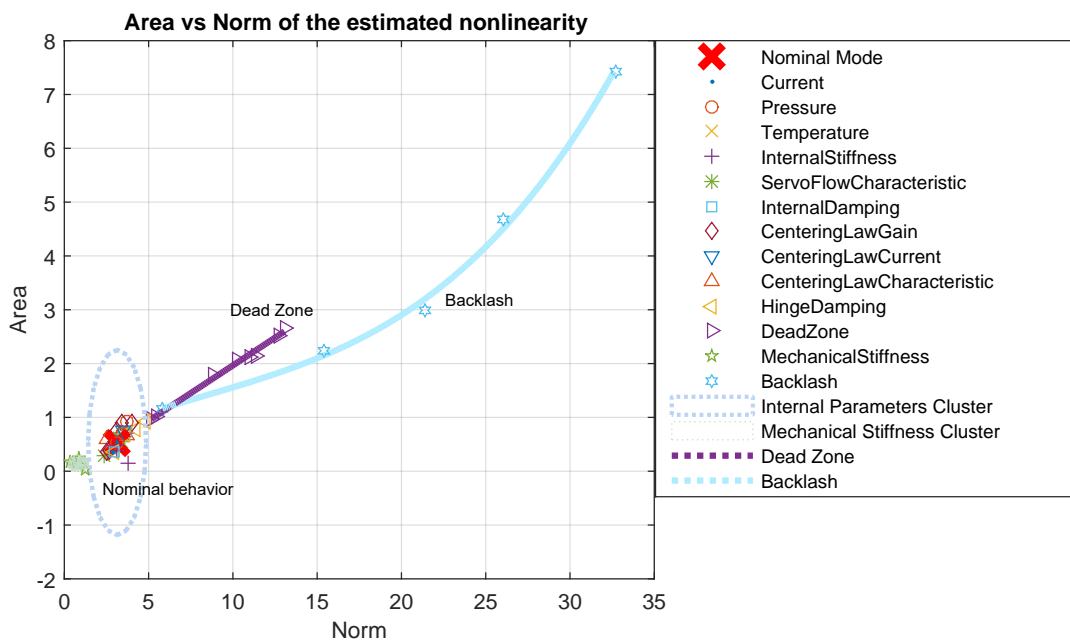


Figure 5.15.: Area versus norm of the estimated nonlinearity for the simulated data [Car18].

### 5.3.3. Experimental results

#### Laboratory

As already mentioned in Section 5.2.3, a test campaign has taken place in 2018 on a specific actuator test bench (Figure 5.10) with calibrated freeplay levels. In particular, two freeplay levels have been tested to confirm the feasibility of the proposed approach. The chosen freeplay levels correspond to a relatively “small” and “large” freeplay on the **actuator bearing** of a specific C/S of an Airbus aircraft (we cannot mention these values for confidentiality reasons). Multiple input signals and flight phases have been tested to evaluate the performance of the Wiener identification method of Pawlak. Indeed, as already seen in Chapter 4, the input can strongly affect the performance. Figures 5.16 and 5.17 display the results of this analysis where the area versus the norm (see (5.2)) of the estimated hysteresis cycle are displayed for two different input signals (CS = chirp signal, WGN = white Gaussian noise) and different freeplay levels. The reader should observe that only the active actuator servoloop is under surveillance and that the “small” and “large” freeplays have been introduced only on the actuator bearings (active and standby actuators) and not on the hinge line. Two distinct regions can be identified in Figs. 5.16 and 5.17: a small freeplay zone (corresponding to small values of the area and the norm) and a large freeplay zone (corresponding to increasing values of the area and the norm). Two different ways of tuning the algorithm are considered in Figures 5.16 and 5.17. Indeed, while in Fig. 5.16 we have considered constant values for the parameters  $h$  and  $g_{\max}$ , in Fig. 5.17 the parameters  $h$  and  $g_{\max}$  are adjusted as a function of the input signal ( $h = 1.06\sigma_{\text{LVDT}}n^{-1/5}$  and  $g_{\max} = \max(\text{LVDT})$ ).

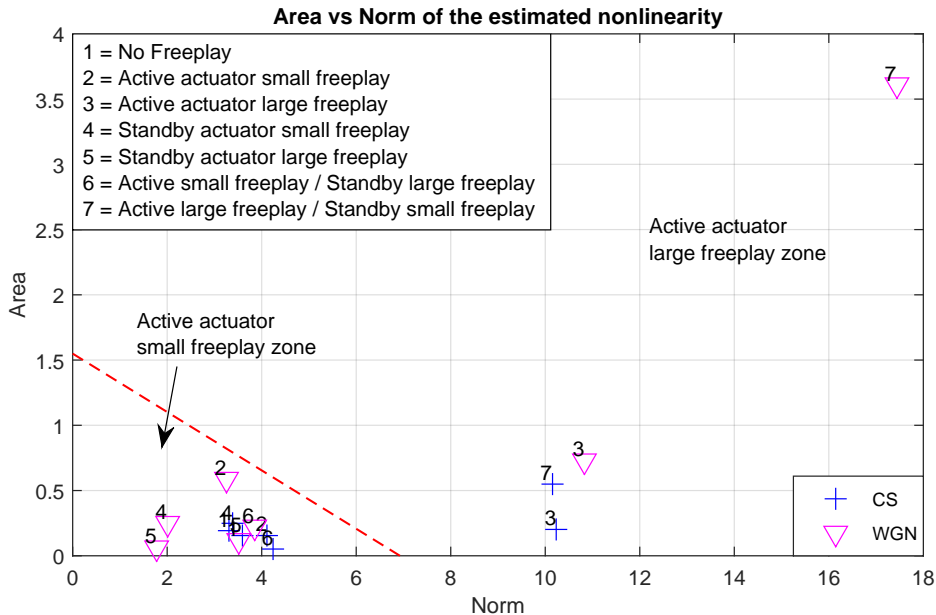


Figure 5.16.: Area versus norm of the estimated nonlinearity for the real actuator test bench. Fixed tuning.

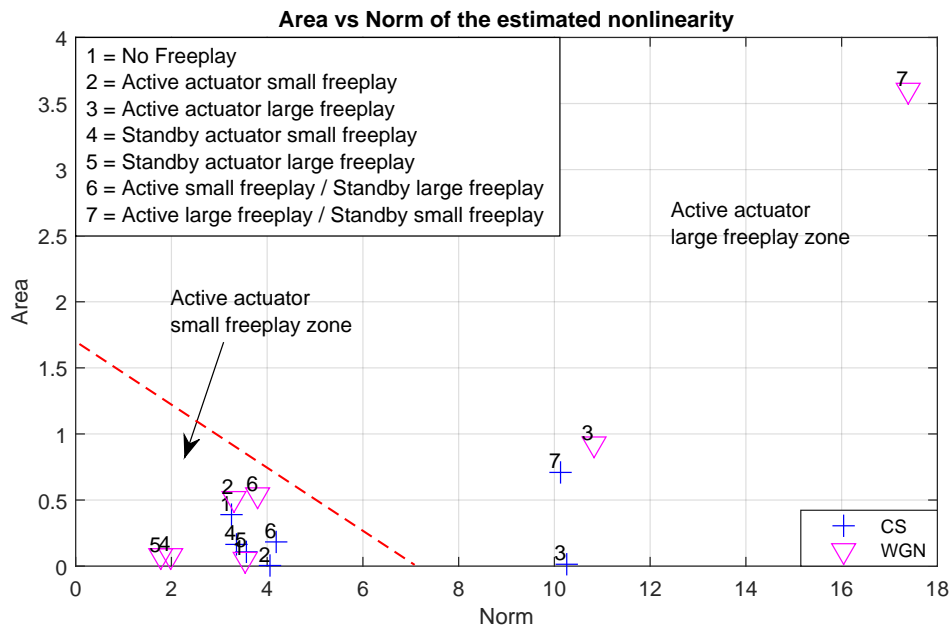


Figure 5.17.: Area versus norm of the estimated nonlinearity for the real actuator test bench. Variable tuning.

Figs. 5.16 and 5.17 confirm that the chosen approach can be used for freeplay diagnostic on a real control surface of a civil aircraft. It can also be observed that the minimum detectable freeplay level is somewhere between the calibrated levels. It is important to mention that in the test campaign multiple inputs and flight phases have been tested. However, only chirp and noise provided consistent results in terms of NMSE with Pawlak's method. A "sufficient excitation" is needed to guarantee the convergence of the method and this leads to some constraints for the industrial application. Persistent and repetitive input signals should be considered to ease the method convergence and to reduce the statistical dispersion of the results.



# 6

## Conclusions

The main contributions of this study are related to the proposal of two algorithmic solutions for LCO and freeplay diagnostic in the actuator control loop of a civil aircraft. LCO diagnostic state-of-the-art is mainly based on the pilot/crew sensitivity to vibrations. In this study a specific GLR test (plus some variants and simplifications) for LCO diagnostic was proposed, as well as a way to assess the GLRT performance analytically without using Monte Carlo runs (Chapter 3). Moreover, the proposed solution was validated considering a quite exhaustive dataset, evaluating its performance, robustness and tuning parameters (Chapter 5). An auto-recursive scheme based on Goertzel algorithm (Appendix A.5) was implemented on Matlab/Simulink to reduce the overall computational cost.

Freeplay diagnostic state-of-the-art is mainly based on planned maintenance checks. In this study it was proposed to estimate the freeplay level based on a system identification approach. The freeplay level between the actuator rod position measure and the control surface position measure is modeled as an hysteresis cycle at the output of a Wiener model. A well-known nonparametric method for Wiener model identification [PHW07] has been modified for the purpose of hysteresis estimation. Moreover, a constrained version of this method was proposed and its parametric version in comparison to the MLE and to some theoretical performance bounds was investigated. Indeed, it was shown that it is sub-optimal compared to the MLE (when the input is not stationary and the additive noise is Gaussian, see Chapter 4). Finally, the modified Pawlak's method was tested considering a quite exhaustive dataset, evaluating its performance and limitations in relation to different freeplay levels and input signals (Chapter 5).

Table 6.1 presents an overview of the datasets considered for the development and validation of the method investigated in this study. The reader should note that the algorithms were validated based on very heterogeneous and exhaustive datasets. Table 6.2 summarizes the results for the datasets of Table 6.1. It can be seen that for the considered vibration detection approach, there exists a tuning that guarantee no false alarm and at the same time allows to anticipate the pilot detection (see Section 5.1, 5.2.2 and 5.2.3). Indeed,

having the right sampling time<sup>1</sup>, the proposed GLR test (and its variants/simplifications) is a very appealing method for LCO diagnostic in terms of performance (minimum detectable amplitude), robustness (false alarm) and computational cost. Moreover, the detector can be easily coded with an auto-recursive scheme and thanks to the performance analysis of [Section 3.7](#), we also have a good theoretical reference for the threshold tuning process. Based on these observations, having the right sampling time for LCO detection (Shannon’s theorem), we can say that GLR tests are a good choice for the considered industrial application.

On the other hand, the proposed freeplay diagnostic algorithm (modified Pawlak’s method for hysteresis estimation) needs to be improved in order to be put into practice. Indeed, it is able to detect relatively large freeplay levels, but it does not provide consistent results for relatively small freeplay levels. Moreover, specific input types (chirp or Gaussian noise of a certain amplitude) are needed to guarantee repetitive and consistent results. The method may also be affected by local minima (as it implicitly involves a non-convex optimization problem) and identifiability problems (due to the considered input signal). The computational cost is high compared to other methods (as patent [\[PK11\]](#)). Finally, despite these drawbacks, the proposed approach for freeplay diagnostic still represent an interesting alternative to the state-of-the-art, thanks to its genericity (block-structured model) and adaptability to the current technology (no additional sensors, no need for too high sampling frequency). Indeed, the method is proven to be able to detect a given freeplay level, but some additional research step are required to improve its accuracy and robustness.

Table 6.1.: Summary of Validation datasets.

Data source	Validation data	
	Vibration diagnostic	Freeplay diagnostic
Synthetic data	simplified actuator control loop and anomaly	synthetic scenario of the type Wiener model
Simulator ( <a href="#">Fig. 5.14</a> )	~ 2500 flight conditions (Mach, Mass, Balance, Turbulence, Flight Phase)	Airbus Matlab/Simulink toolbox (13 parameters)
Flight data	~ 56 hours	4 flights with calibrated free play level
Laboratory ( <a href="#">Fig. 5.10</a> )	elevator test bench with calibrated freeplay and vibration	elevator test bench with calibrated freeplay

## Perspectives

This research study is the result of a 3 years **CIFRE** PhD thesis between Airbus and TésA laboratory. Thus, this research study has both industrial and academic vocations.

For the industrial project the results correspond to a technology readiness level (TRL) of 4, in a scale between

<sup>1</sup>this is not always possible, see [Section 2.6](#)

Table 6.2.: Results summary.

Data source	Validation results	
	Vibration diagnostic	Freeplay diagnostic
Synthetic data	Section 3.8.3: the algorithm is feasible, performance analysis validation.	Section 4.3.2 and 4.4: the algorithm is feasible, comparison Pawlak's method, MLE and performance bounds.
Simulator (Fig. 5.14)	Section 5.2.2: no false alarms, anticipate pilot detection, error analysis of estimators.	Section 5.3.2: freeplay segregation using LVDT/RVDT, choice of the features (area vs norm).
Flight data	Section 5.2.1 and 5.2.3: no false alarms, anticipate pilot detection (but $\Delta T > 20s$ ).	Section 5.3.1: there is a trend on the 4 flights with calibrated free play.
Laboratory (Fig. 5.10)	Section 5.2.3: no false alarms, anticipate pilot detection.	Section 5.3.3: "large" freeplay can be detected, input signal sensitivity.

1 and 9 [Man95] (Figure 6.1), that is the last step before the technology demonstration. Thus, to reach TRL9 (system launch) there is a long road ahead and the next levels are often very difficult to achieve [GDB14][Zol17]. In the present study a quite extensive validation has been accomplished, but a more extensive verification and validation ("V&V") campaign on real data and real hardware has to be accomplished to reach TRL5 (technology demonstration). Moreover, in the long-term, the in-service implementation has to be fully clarified and adapted to the airline need in order to reach the last steps of Fig. 6.1.

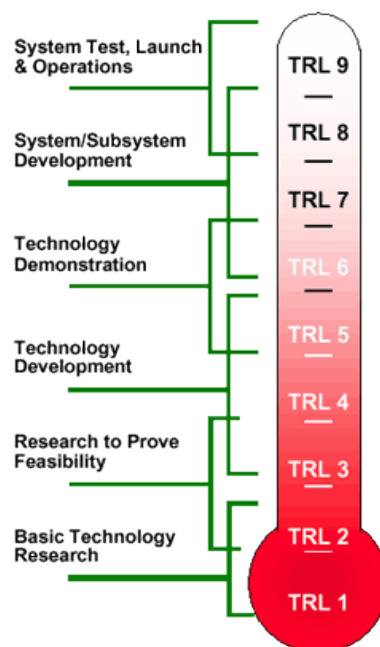


Figure 6.1.: NASA technology readiness levels (TRL).

From the academic point of view, multiple research paths can be identified starting from the contribution

presented in this study (see also Sections 3.9 and 4.5). In particular, as short-term perspective for LCO detection, it can be interesting to study a **Bayesian approach** to integrate the a priori information directly in the test statistic. Moreover, it can be useful to consider a data fusion algorithm to integrate other signals (already available in the flight control computers on board the aircraft) as accelerometers or pressure sensors. This study also considered a particular interference model and a known noise variance. It would be interesting to extend our derivations to different interference models with a possible unknown noise variance.

As short-term perspectives for freeplay diagnostic, it would be important to investigate the MLE when the non-linearity is an hysteresis cycle and to evaluate its sensitivity to initialization. Indeed, we had time to validate only Pawlak's method on experimental data, but we have shown (in theory and on synthetic data) that it is sub-optimal compared to the MLE (when the input is not stationary and the additive noise is Gaussian) and it leads to consistent results only for some specific inputs. Given the importance of the input signal in the identification problem, it would be useful also to analyze if there exists an optimal input signal, in terms of freeplay detection accuracy and robustness, for Pawlak method and for the MLE.

The main goal of this research study was to find a software solution for LCO diagnostic using only existing signals available in the flight control computers on board in-series aircraft, being compliant with the current hardware and possibly being independent from the specific surface/actuator combination. A contribution in this sense was given and further studies could lead to the technology deployment in operation. However, in the long-term, a different solution might be proposed. In Chapter 2 we have seen that the EFCS is a system in continuous evolution. New systems, sensors and communication means will be introduced in the next aircraft generation. For example, long endurance wireless accelerometers installed on the tip of the vertical and horizontal stabilizers would certainly improve the accuracy and robustness of LCO detection. Moreover, specific sensors might be developed to monitor the actuator bearings and the freeplay level. In parallel with new sensors, advanced health monitoring systems could be introduced. These systems would be able to host advanced machine learning techniques and manage multiple undesired vibrations at the same time. Finally, in Chapter 2 we have also seen that there is a wide literature about active control of vibrations like the LCO, but relatively few applications. The next generation aircraft would probably be able to control the LCO (and similar undesired vibrations) once it is detected in-flight, reducing the need for corrective and preventive maintenance tasks related to freeplay and LCO.



# Annexes

## A.1. Asymptotic approximation for the sufficient statistic

In the asymptotic region, at high SNR [Ren+06]

$$\hat{\alpha} = \alpha + d\hat{\alpha}, \quad \|d\hat{\alpha}\|^2 \ll 1$$

thus, developing the quadratic terms at the first order we obtain

$$\begin{aligned} & \left\| \Pi_{\mathbf{H}(\alpha+d\hat{\alpha})}^\perp \mathbf{y} \right\|^2 \\ & \approx \left\| \begin{aligned} & \Pi_{\mathbf{H}(\alpha)}^\perp \mathbf{H}(\alpha) \beta + \frac{\partial \Pi_{\mathbf{H}(\alpha)}^\perp}{\partial \alpha} \mathbf{H}(\alpha) \beta d\hat{\alpha} \\ & + \Pi_{\mathbf{H}(\alpha)}^\perp \mathbf{w} + \frac{\partial \Pi_{\mathbf{H}(\alpha)}^\perp}{\partial \alpha} \mathbf{w} d\hat{\alpha} \end{aligned} \right\|^2 \\ & \approx \left\| \Pi_{\mathbf{H}(\alpha)}^\perp \mathbf{H}(\alpha) \beta + \frac{\partial \Pi_{\mathbf{H}(\alpha)}^\perp}{\partial \alpha} \mathbf{H}(\alpha) \beta d\hat{\alpha} + \Pi_{\mathbf{H}(\alpha)}^\perp \mathbf{w} \right\|^2. \end{aligned}$$

The previous equation can be simplified by differentiating

$$\mathbf{0} = \Pi_{\mathbf{H}(\alpha)}^\perp \mathbf{H}(\alpha)$$

leading to

$$\frac{\partial \Pi_{\mathbf{H}(\alpha)}^\perp}{\partial \alpha} \mathbf{H}(\alpha) = -\Pi_{\mathbf{H}(\alpha)}^\perp \frac{\partial \mathbf{H}(\alpha)}{\partial \alpha}.$$

As a consequence

$$\begin{aligned}
 & \left\| \Pi_{\mathbf{H}(\boldsymbol{\alpha} + \widehat{d\boldsymbol{\alpha}})}^\perp \mathbf{y} \right\|^2 \\
 & \approx \left\| \Pi_{\mathbf{H}(\boldsymbol{\alpha})}^\perp \mathbf{H}(\boldsymbol{\alpha}) \boldsymbol{\beta} - \Pi_{\mathbf{H}(\boldsymbol{\alpha})}^\perp \frac{\partial \mathbf{H}(\boldsymbol{\alpha})}{\partial \boldsymbol{\alpha}} \boldsymbol{\beta} \widehat{d\boldsymbol{\alpha}} + \Pi_{\mathbf{H}(\boldsymbol{\alpha})}^\perp \mathbf{w} \right\|^2 \\
 & = \left\| \Pi_{\mathbf{H}(\boldsymbol{\alpha})}^\perp \mathbf{y} - \Pi_{\mathbf{H}(\boldsymbol{\alpha})}^\perp \frac{\partial \mathbf{H}(\boldsymbol{\alpha})}{\partial \boldsymbol{\alpha}} \boldsymbol{\beta} \widehat{d\boldsymbol{\alpha}} \right\|^2 = \left\| \Pi_{\mathbf{H}(\boldsymbol{\alpha})}^\perp \mathbf{y} - \mathbf{D} \widehat{d\boldsymbol{\alpha}} \right\|^2 \\
 & = \left\| \Pi_D^\perp \Pi_{\mathbf{H}(\boldsymbol{\alpha})}^\perp \mathbf{y} \right\|^2 + \left\| \Pi_D \Pi_{\mathbf{H}(\boldsymbol{\alpha})}^\perp \mathbf{y} - \mathbf{D} \widehat{d\boldsymbol{\alpha}} \right\|^2
 \end{aligned}$$

with  $\mathbf{D} = \Pi_{\mathbf{H}(\boldsymbol{\alpha})}^\perp \frac{\partial \mathbf{H}(\boldsymbol{\alpha}) \boldsymbol{\beta}}{\partial \boldsymbol{\alpha}}$ . The quantity  $\left\| \Pi_{\mathbf{H}(\boldsymbol{\alpha} + \widehat{d\boldsymbol{\alpha}})}^\perp \mathbf{y} \right\|^2$  reaches its minimum if  $\widehat{d\boldsymbol{\alpha}}$  is chosen as follows

$$\Pi_D \Pi_{\mathbf{H}(\boldsymbol{\alpha})}^\perp \mathbf{y} = \mathbf{D} \widehat{d\boldsymbol{\alpha}}$$

or equivalently if

$$\widehat{d\boldsymbol{\alpha}} = (\mathbf{D}^T \mathbf{D})^{-1} \mathbf{D}^T \Pi_{\mathbf{H}(\boldsymbol{\alpha})}^\perp \mathbf{y} \quad (\text{A.1})$$

leading to

$$\left\| \Pi_{\mathbf{H}(\boldsymbol{\alpha} + \widehat{d\boldsymbol{\alpha}})}^\perp \mathbf{y} \right\|^2 \approx \left\| \Pi_D^\perp \Pi_{\mathbf{H}(\boldsymbol{\alpha})}^\perp \mathbf{y} \right\|^2.$$

Straightforward computations allow the following result to be obtained

$$E[\widehat{d\boldsymbol{\alpha}} \widehat{d\boldsymbol{\alpha}}^T] = \text{CRB}(\boldsymbol{\alpha})$$

which proves that  $\boldsymbol{\alpha} + \widehat{d\boldsymbol{\alpha}}$  is a valid approximation of the CMLE in the asymptotic region.

## A.2. Characteristic functions and PDF approximation

The characteristic function of a random variable  $Z$ , defined as the linear combination of random variables  $X_n$  with real constant coefficients  $a_n$

$$Z = \sum_{n=1}^N a_n X_n$$

is simply given by

$$\varphi_Z(t) = \prod_{n=1}^N \varphi_{X_n}(a_n t).$$

Assume that  $X_n$  is distributed according to a non-central chi-square distribution with  $l$  degrees of freedom and non-centrality parameter  $k$ . The characteristic function of  $X_n$  is denoted as is  $\varphi_{k,l}$  and defined as

$$\varphi_{k,l}(t) = \frac{\exp\left(\frac{ikt}{1-2it}\right)}{(1-2it)^{l/2}}.$$

The approximated probability density function (pdf) of  $Z$  can then be obtained as the inverse Fourier transform of its characteristic function by numerical integration. However, to obtain directly the cumulative distribution function (CDF) of  $Z$  one can also use the Gil-Pelaez's formula [Gil51]

$$F_Z(z) = \frac{1}{2} - \frac{1}{\pi} \int_0^{\infty} \frac{\text{Im}[e^{-itz} \varphi_Z(t)]}{t} dt.$$

### A.3. Projection matrices

For the nested model (3.20), it can be shown that the ‘‘approximate GLRT’’ statistic (see Section 3.7) can be written as a quadratic form of the type  $\mathbf{x}^T \Pi \mathbf{x}$ , where  $\Pi$  is a symmetric and idempotent matrix. In this section it is verified that the matrix  $\Pi$  is a projection (for the two cases of  $\boldsymbol{\alpha}$  known and  $\boldsymbol{\alpha}$  unknown).

#### $\beta$ unknown and $\alpha$ known

The matrix  $\mathbf{K} = \Pi_{\mathbf{H}_0(\boldsymbol{\alpha}_0)}^\perp - \Pi_{\mathbf{H}_1(\boldsymbol{\alpha}_1)}^\perp$  is symmetric and idempotent. Indeed, it is symmetric by difference between symmetric matrices. In order to show its idempotence, One can simply consider  $\mathbf{H}_1(\boldsymbol{\alpha}_1)\mathbf{A} = \mathbf{H}_0(\boldsymbol{\alpha}_0)$  (where  $\mathbf{A}$  is a suitable matrix) to prove the following expressions

$$\begin{cases} \Pi_{\mathbf{H}_0(\boldsymbol{\alpha}_0)}^\perp \Pi_{\mathbf{H}_1(\boldsymbol{\alpha}_1)}^\perp = \Pi_{\mathbf{H}_1(\boldsymbol{\alpha}_1)}^\perp \\ \Pi_{\mathbf{H}_0(\boldsymbol{\alpha}_0)} \Pi_{\mathbf{H}_1(\boldsymbol{\alpha}_1)} = \Pi_{\mathbf{H}_0(\boldsymbol{\alpha}_0)} \end{cases} \quad (\text{A.2})$$

hence

$$\left[ \Pi_{\mathbf{H}_0(\boldsymbol{\alpha}_0)}^\perp - \Pi_{\mathbf{H}_1(\boldsymbol{\alpha}_1)}^\perp \right]^2 = \Pi_{\mathbf{H}_0(\boldsymbol{\alpha}_0)}^\perp - \Pi_{\mathbf{H}_1(\boldsymbol{\alpha}_1)}^\perp.$$

which proves the idempotence.

### $\beta$ unknown and $\alpha$ unknown

The matrix  $\mathbf{K}_a = \mathbf{L}_0^\perp - \mathbf{L}_1^\perp$  is symmetric and idempotent. Indeed, it is symmetric by difference between symmetric matrices

$$\mathbf{L}_0^\perp = \Pi_{\mathbf{H}_0(\alpha_0)}^\perp \Pi_{\mathbf{D}_0}^\perp \Pi_{\mathbf{H}_0(\alpha_0)}^\perp, \quad \mathbf{L}_1^\perp = \Pi_{\mathbf{H}_1(\alpha_1)}^\perp \Pi_{\mathbf{D}_1}^\perp \Pi_{\mathbf{H}_1(\alpha_1)}^\perp$$

where  $\mathbf{D} = \Pi_{\mathbf{H}(\alpha)}^\perp \frac{\partial \mathbf{H}(\alpha) \beta}{\partial \alpha}$ . In order to show the idempotence of  $\mathbf{K}_a$ , we recall (A.2) and consider the notation

$$\frac{\partial(\mathbf{H}_0(\alpha_0)\beta_0)}{\partial \alpha_0} = \mathbf{Q}_0, \quad \frac{\partial(\mathbf{H}_1(\alpha_1)\beta_1)}{\partial \alpha_1} = \mathbf{Q}_1, \quad \mathbf{Q}_1 \mathbf{B} = \mathbf{Q}_0$$

where  $\mathbf{B}$  is a suitable transformation matrix ( $\mathbf{Q}_0$  is included in  $\mathbf{Q}_1$ , as the matrix  $\mathbf{H}_0(\alpha_0)$  is included in  $\mathbf{H}_1(\alpha_1)$ ). One can observe that

$$\Pi_{\mathbf{H}_0}^\perp \Pi_{\mathbf{D}_0} \Pi_{\mathbf{H}_1}^\perp \Pi_{\mathbf{D}_1} = \Pi_{\mathbf{H}_0}^\perp \mathbf{Q}_0 (\mathbf{Q}_0^T \Pi_{\mathbf{H}_0}^\perp \mathbf{Q}_0)^{-1} \mathbf{B}^T (\mathbf{Q}_1^T \Pi_{\mathbf{H}_1}^\perp \mathbf{Q}_1) (\mathbf{Q}_1^T \Pi_{\mathbf{H}_1}^\perp \mathbf{Q}_1)^{-1} \mathbf{Q}_1^T = \Pi_{\mathbf{H}_0}^\perp \Pi_{\mathbf{D}_0}$$

hence

$$\Pi_{\mathbf{H}_1}^\perp \Pi_{\mathbf{D}_0} \Pi_{\mathbf{D}_1} = \Pi_{\mathbf{H}_0}^\perp \Pi_{\mathbf{D}_0}.$$

As a consequence

$$\Pi_{\mathbf{H}_0}^\perp \Pi_{\mathbf{D}_0}^\perp \Pi_{\mathbf{H}_1}^\perp \Pi_{\mathbf{D}_1}^\perp = \Pi_{\mathbf{H}_1}^\perp \Pi_{\mathbf{D}_0}^\perp \Pi_{\mathbf{D}_1}^\perp = \Pi_{\mathbf{H}_1}^\perp - \Pi_{\mathbf{H}_1}^\perp \Pi_{\mathbf{D}_1} - \Pi_{\mathbf{H}_1}^\perp \Pi_{\mathbf{D}_0} + \Pi_{\mathbf{H}_1}^\perp \Pi_{\mathbf{D}_0} \Pi_{\mathbf{D}_1} = \Pi_{\mathbf{H}_1}^\perp - \Pi_{\mathbf{H}_1}^\perp \Pi_{\mathbf{D}_1} = \Pi_{\mathbf{H}_1}^\perp \Pi_{\mathbf{D}_1}^\perp$$

or equivalently

$$\mathbf{L}_0^\perp \mathbf{L}_1^\perp = \mathbf{L}_1^\perp$$

which proves the idempotence of  $\mathbf{K}_a$  [PSZ96].

## A.4. GLRT by Alternating Projection (AP)

We have seen that the algorithm of the GLRT is not fully satisfactory from a computational point of view because it requires a nonlinear multivariate optimization. For this reason, we decided to consider a different approach to reduce the computational burden. The **Alternating Projection (AP) approach** [ZW88] consider a sequence of one-dimensional optimization for computing the ML estimator and thus it guarantee lower complexity and computational time. For every iteration a maximization is performed on a single parameter while all the others parameters are held fixed. Since a maximization is performed at every iteration, the algorithm will surely converge to a local maximum. However, depending on the initial condition, the local maximum may or may

not be the global one and this represents the main drawback of this approach.

In order to compute  $\hat{\alpha}_1$ , we have seen that we need to consider an optimization problem on the parameters  $p$  and  $f$ . Introducing the following notation for the matrix  $\mathbf{H}$

$$\mathbf{H}(\alpha) = [\mathbf{x}(p), \mathbf{c}(f), \mathbf{s}(f)] = [\mathbf{x}(p), \mathbf{z}(f)]$$

The MLE can be written in the form

$$\hat{\alpha}_1 = \operatorname{argmin}_{\alpha} \|\Pi_{\mathbf{H}}^{\perp} \mathbf{y}\|^2 = \operatorname{argmax}_{\alpha} \|\Pi_{\mathbf{H}} \mathbf{y}\|^2 = \operatorname{argmax}_{\alpha} \left( \|\Pi_{\mathbf{x}} \mathbf{y}\|^2 + \|\Pi_{\Pi_{\mathbf{x}}^{\perp} \mathbf{z}} \mathbf{y}\|^2 \right) \quad (\text{A.3})$$

where we have applied the following decomposition [Cha14][ZW88] of the projection matrix  $\Pi_{\mathbf{H}}$

$$\mathbf{H}(\alpha) = [\mathbf{x}(p), \mathbf{z}(f)] \rightarrow \Pi_{\mathbf{H}} = \Pi_{\mathbf{x}} + \Pi_{\Pi_{\mathbf{x}}^{\perp} \mathbf{z}}$$

It has to be observed that (A.3) requires the simultaneous optimization of two terms (the first dependent on  $p$  and the other on  $p$  and  $f$ ). In the AP approach, we can consider separately the optimization of the two terms. So, the ML estimation problem reduces to two one-dimensional optimization problems

- 1)  $\operatorname{argmax}_p \|\Pi_{\mathbf{x}} \mathbf{y}\|^2$
- 2)  $\operatorname{argmax}_f \|\Pi_{\Pi_{\mathbf{x}}^{\perp} \mathbf{z}} \mathbf{y}\|^2$

Considering the maximization of the first term, we can recognize that it leads to

$$\operatorname{argmax}_p \|\Pi_{\mathbf{x}} \mathbf{y}\|^2 = \operatorname{argmax}_p \left\{ \frac{(\sum_{n=0}^{N-1} y(n)x(n-p))^2}{\sum_{n=0}^{N-1} x(n-p)^2} \right\} = \hat{p}_1 = \hat{p}_0 = \hat{p}$$

The observation that  $\hat{p}_1 = \hat{p}_0 = \hat{p}$  is useful also to simplify the expression of the GLRT. In fact, the sufficient statistic reduces to

$$\begin{aligned} T' &= \frac{1}{2\sigma^2} \left( \|\Pi_{\mathbf{H}}(\hat{\alpha}_1) \mathbf{y}\|^2 - \|\Pi_{\mathbf{H}}(\hat{\alpha}_0) \mathbf{y}\|^2 \right) = \\ &= \frac{1}{2\sigma^2} \left( \|\Pi_{\mathbf{x}} \mathbf{y}\|^2 + \|\Pi_{\Pi_{\mathbf{x}}^{\perp} \mathbf{z}} \mathbf{y}\|^2 - \|\Pi_{\mathbf{x}} \mathbf{y}\|^2 \right) = \\ &= \frac{1}{2\sigma^2} \|\Pi_{\Pi_{\mathbf{x}}^{\perp} \mathbf{z}} \mathbf{y}\|^2 > \gamma_a'' \end{aligned}$$

For the maximization of the second term, we can rewrite  $\Pi_{\Pi_x^\perp \mathbf{z}}$  as

$$\Pi_{\Pi_x^\perp \mathbf{z}} = \Pi_x^\perp \mathbf{z} (\mathbf{z}^T \Pi_x^\perp \mathbf{z})^{-1} \mathbf{z}^T \Pi_x^\perp$$

So the ML estimation of  $f$  can be obtained from the following function

$$\begin{aligned} \hat{f} &= \operatorname{argmax}_\alpha \left( \|\Pi_{\Pi_x^\perp \mathbf{z}} \mathbf{y}\|^2 \right) = \\ &\operatorname{argmax}_\alpha \left( \|\Pi_x^\perp \mathbf{z} (\mathbf{z}^T \Pi_x^\perp \mathbf{z})^{-1} \mathbf{z}^T \Pi_x^\perp \mathbf{y}\|^2 \right) \\ &\operatorname{argmax}_\alpha \left( \mathbf{y}^T \Pi_x^\perp \mathbf{z} (\mathbf{z}^T \Pi_x^\perp \mathbf{z})^{-1} \mathbf{z}^T \Pi_x^\perp \mathbf{y} \right) \end{aligned}$$

AS the sufficient statistic for the AP approach is

$$T' = \frac{1}{2\sigma^2} \|\Pi_{\Pi_x^\perp \mathbf{z}} \mathbf{y}\|^2 > \gamma_a''$$

or equivalently

$$T' = \frac{1}{2\sigma^2} \left( \mathbf{y}^T \Pi_x^\perp \mathbf{z} (\mathbf{z}^T \Pi_x^\perp \mathbf{z})^{-1} \mathbf{z}^T \Pi_x^\perp \mathbf{y} \right)$$

for large sample ( $N \rightarrow \infty$ ) that corresponds to

$$T'' = \left( \frac{(\mathbf{x}^T(\hat{p}_1)\mathbf{y})^2 \frac{2I_x(\hat{f})}{\mathbf{x}^T(\hat{p}_1)\mathbf{x}(\hat{p}_1)} + 2(\mathbf{x}^T(\hat{p}_1)\mathbf{x}(\hat{p}_1))I_y(\hat{f}) - 4(\mathbf{x}^T(\hat{p}_1)\mathbf{y})\operatorname{Re}[I_{xy}(\hat{f})] - 4(\operatorname{Im}[I_{xy}(\hat{f})])^2}{(\mathbf{x}^T(\hat{p}_1)\mathbf{x}(\hat{p}_1)) - 2I_x(\hat{f})} \right) > 2\sigma^2\gamma''$$

if we can consider that the power of the anomaly is small compared to the energy and covariance terms  $\mathbf{x}^T(\hat{p})\mathbf{x}(\hat{p})$  and  $\mathbf{x}^T(\hat{p})\mathbf{y}$ ; we can consider  $(\operatorname{Im}[I_{xy}(\hat{f})])^2 \approx 0$  and  $\frac{2I_x(\hat{f})}{\mathbf{x}^T(\hat{p}_1)\mathbf{x}(\hat{p}_1)} \approx 0$ . So, the simplified statistic will be again

$$T''' = \left( I_y(\hat{f}) - 2r'(\hat{\rho}) \operatorname{Re}[I_{xy}(\hat{f})] \right) > \sigma^2 \gamma''$$

### Remark

We have argued before that the AP approach does not guarantee the convergence to a global maximum. However, it can be noticed that, for our case study, the global maximum of (A.3) is not so far from the one identified by optimization of the first term ( $\|\Pi_{\mathbf{x}}\mathbf{y}\|^2$ ) alone.

## A.5. Goertzel algorithm

The Goertzel algorithm is a digital signal processing technique used to identify the different frequency components of a signal. The main difference with the Fast Fourier Transform (FFT) approach is that while the general form of the FFT consider the whole bandwidth, the Goertzel algorithm consider only some specific frequencies. Moreover, this algorithm can be used to compute directly  $|X(\omega)|^2$ . The computational complexity of this algorithm for  $M$  computed frequencies is only  $NM$ . So, this algorithm can perform a faster analysis than FFT for

$$M \leq \frac{5N_2}{6N} \log_2 N_2 \quad (\text{A.4})$$

where  $N_2$  is the nearest exact power of 2 of  $N$ .

The main idea of this algorithm comes from the observation that, if we want to extract some frequencies from a signal  $x$ , we can observe that the last term of the sequence

$$y(n) = x(n) + y(n-1)e^{i\omega} \quad (\text{A.5})$$

is "almost" equal to the DFT of the signal computed at the frequency  $\omega$ . In fact, it is possible to show that:

$$y(n-1) = e^{i\omega(N-1)} \sum_{m=0}^{N-1} x_m e^{-i\omega m} \quad (\text{A.6})$$

thus  $y(n-1)$  is equal to  $X(\omega)$  multiplied for a complex constant  $e^{i\omega(N-1)}$ . The Goertzel algorithm computes  $X(w)$  using the combination of two filters: a second order IIR filter and a first order FIR filter. An example of a recursive algorithm that use the Goertzel algorithm is the one shown in Figure A.1 implemented on Simulink.

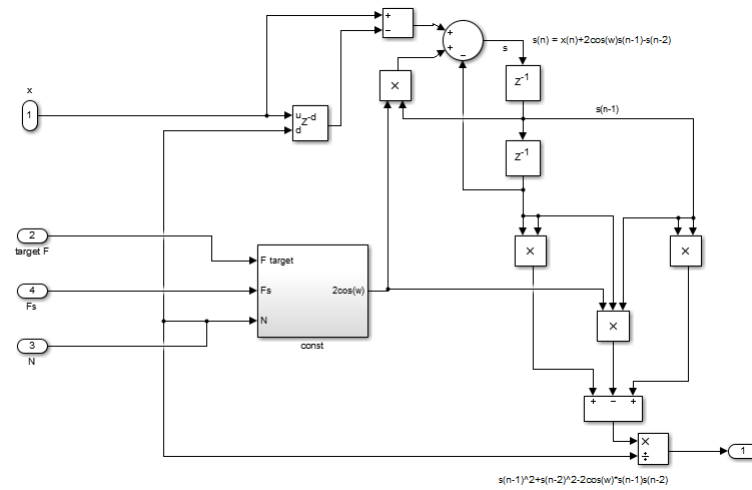


Figure A.1.: Simulink implementation of Goertzel algorithm ( $|X(\omega)|^2$ ) for a given frequency.

# Bibliography

- [Adm07] Federal Aviation Administration. *Memorandum ANM-05-115-019*. Tech. rep. 2007. URL: [http://rgl.faa.gov/Regulatory\\_and\\_Guidance\\_Library/rgPolicy.nsf](http://rgl.faa.gov/Regulatory_and_Guidance_Library/rgPolicy.nsf) (cit. on p. 24).
- [Air93] Naval air warfare center Aircraft division. *MIL-A-8870C: Airplane strength and rigidity vibration, flutter and divergence*. Tech. rep. 1993. URL: <http://everyspec.com/MIL-SPECS/MILSPECS-MIL-A/download.php?spec=MIL-A-8870C.006746.PDF> (cit. on p. 24).
- [Ath05] Fredrik Athley. “Threshold region performance of maximum likelihood direction of arrival estimators”. In: *IEEE Trans. Signal Process.* 53.4 (2005), pp. 1359–1373 (cit. on pp. 30, 43).
- [Bal+09] Edward Balaban et al. “A diagnostic approach for electro-mechanical actuators in aerospace systems”. In: *Proc. IEEE Aerospace conference*. IEEE. Big Sky, Montana, 2009, pp. 1–13 (cit. on p. 22).
- [Bia14] Brendan Bialy. “Lyapunov-based control of limit cycle oscillations in uncertain aircraft systems”. PhD thesis. University of Florida, 2014 (cit. on p. 22).
- [Car18] Jonathan Cardona. “Actuator servo loop analysis for mechanical free play diagnostic on the control surface of a civil aircraft.” MA thesis. INP-ENSEEIH, Toulouse, 2018 (cit. on p. 99).
- [Cas15] Mario Cassaro. “Model Reference Adaptive Control Laws: Application to Nonlinear Aeroelastic Systems”. PhD thesis. Politecnico di Torino, 2015 (cit. on p. 22).
- [CDF00] Robert L Clark, Earl H Dowell, and Kenneth D Frampton. “Control of a three-degree-of-freedom airfoil with limit-cycle behavior”. In: *Journal of Aircraft* 37.3 (2000), pp. 533–536 (cit. on p. 22).
- [Cha+08] Eric Chaumette et al. “A New Barankin Bound Approximation for the Prediction of the Threshold Region Performance of Maximum Likelihood Estimators”. In: *IEEE Trans. Signal Process.* 56.11 (2008), pp. 5319–5333 (cit. on p. 77).
- [Cha14] Eric Chaumette. *Caractérisation des problèmes conjoints de détection et d’estimation*. Habilitation à Diriger des Recherches, École Normale Supérieure de Cachan, 2014 (cit. on p. 111).
- [Chu10] Pei-Jung Chung. “A max-search approach for DOA estimation with unknown number of signals”. In: *IEEE Journal of Selected Topics in Signal Processing* 4.3 (2010), pp. 612–619 (cit. on p. 51).
- [Con+97] Mark D Conner et al. “Nonlinear behavior of a typical airfoil section with control surface freeplay: a numerical and experimental study”. In: *Journal of Fluids and structures* 11.1 (1997), pp. 89–109 (cit. on p. 20).

- [Dim99] Grigorios Dimitriadis. “Investigation of Nonlinear Aeroelastic Systems”. PhD thesis. University of Manchester, 1999 (cit. on p. 20).
- [Dow15] Earl H Dowell. *A modern course in aeroelasticity, Fifth Revised and Enlarged Edition*. Springer International Publishing, 2015 (cit. on pp. 15, 20).
- [EI00] EUROCAE and RTCA Inc. *Design Assurance Guidance for Airborne Electronic Hardware*. RTCA DO-254/EUROCAE ED-80. 2000 (cit. on p. 10).
- [EI92] EUROCAE and RTCA Inc. *Software Considerations in Airborne Systems and Equipment Certification*. RTCA/DO-178B. 1992 (cit. on p. 10).
- [EP13] Christopher W Emory and Mayuresh J Patil. “Predicting limit cycle oscillation in an aeroelastic system using nonlinear normal modes”. In: *Journal of Aircraft* 50.1 (2013), pp. 73–81 (cit. on p. 22).
- [FAA02] Federal Aviation Administration (FAA). *Airworthiness Directives, Boeing Model 737-600, -700, -700C, and -800 Series Airplanes, Federal Register, Rules and Regulations, Vol. 67, No. 81*. Tech. rep. 2002. URL: <https://www.gpo.gov/fdsys/pkg/FR-2002-04-26/pdf/02-10244.pdf> (cit. on p. 24).
- [FAA15] Federal Aviation Administration (FAA). *Airworthiness Directives, Boeing Model 777-200, -200LR, -300, and -300ER series airplanes, Federal Register, Rules and Regulations, Vol. 80, No. 115*. Tech. rep. 2015. URL: [http://ad.easa.europa.eu/blob/20151203\\_Correction.pdf/AD\\_US-2015-12-03\\_1](http://ad.easa.europa.eu/blob/20151203_Correction.pdf/AD_US-2015-12-03_1) (cit. on p. 24).
- [FS06] Spilios D Fassois and John S Sakellariou. “Time-series methods for fault detection and identification in vibrating structures”. In: *Philosophical Transactions of the Royal Society A: Mathematical, Physical and Engineering Sciences* 365.1851 (2006), pp. 411–448 (cit. on p. 23).
- [GB10] Fouad Giri and Er-Wei Bai. *Block-oriented nonlinear system identification*. Vol. 1. Springer, 2010 (cit. on p. 57).
- [GCL10] Jérôme Galy, Eric Chaumette, and Pascal Larzabal. “Joint detection estimation problem of monopulse angle measurement”. In: *IEEE Trans. Aerosp. Electron. Syst.* 46.1 (2010), pp. 397–413 (cit. on p. 30).
- [GDB14] Philippe Goupil, Rémy Dayre, and Patrice Brot. “From theory to flight tests: Airbus Flight Control System TRL5 achievements”. In: *Proc. 19th IFAC World Congress, IFAC Proceedings Volumes*. Vol. 47. 3. Cape Town, South Africa: Elsevier, 2014, pp. 10562–10567 (cit. on p. 105).
- [Gil51] J Gil-Pelaez. “Note on the inversion theorem”. In: *Biometrika* 38.3-4 (1951), pp. 481–482 (cit. on p. 109).

- 
- [Gir+13] Fouad Giri et al. “Frequency identification of nonparametric Wiener systems containing backlash nonlinearities”. In: *Automatica* 49.1 (2013), pp. 124–137 (cit. on p. 57).
- [GK08] Paul Gold and Moti Karpel. “Reduced-size aeroservoelastic modeling and limit-cycle-oscillation simulations with structurally nonlinear actuators”. In: *Journal of Aircraft* 45.2 (2008), pp. 471–477 (cit. on p. 20).
- [GMM08] James T Gordon, Edward E Meyer, and Robert L Minogue. “Nonlinear stability analysis of control surface flutter with freeplay effects”. In: *Journal of Aircraft* 45.6 (2008), pp. 1904–1916 (cit. on p. 20).
- [Gou10] Philippe Goupil. “Oscillatory failure case detection in the A380 electrical flight control system by analytical redundancy”. In: *Control Engineering Practice* 18.9 (2010), pp. 1110–1119 (cit. on p. 25).
- [Gou11] Philippe Goupil. “AIRBUS state of the art and practices on FDI and FTC in flight control system”. In: *Control Engineering Practice* 19.6 (2011), pp. 524–539 (cit. on pp. 10, 12).
- [GP08] Włodzimierz Greblicki and Mirosław Pawlak. *Nonparametric system identification*. Vol. 1. Cambridge University Press Cambridge, 2008 (cit. on p. 57).
- [Gre92] Włodzimierz Greblicki. “Nonparametric identification of Wiener systems”. In: *IEEE Trans. Inf. Theory* 38.5 (1992), pp. 1487–1493 (cit. on p. 57).
- [GS01] Georgios B Giannakis and Erchin Serpedin. “A bibliography on nonlinear system identification”. In: *Signal Process.* 81 (2001), pp. 533–580 (cit. on p. 57).
- [GUT16] Philippe Goupil, Simone Urbano, and Jean-Yves Tourneret. “A Data-Driven Approach to Detect Faults in the Airbus Flight Control System”. In: *Proc. 20th IFAC Symposium on Automatic Control in Aerospace, IFAC-PapersOnLine*. Vol. 49. 17. Sherbrooke, Canada: Elsevier, 2016, pp. 52–57 (cit. on p. 25).
- [int96] SAE international. *Certification considerations for highly-integrated or complex aircraft systems*. ARP4754, SAE. 1996 (cit. on p. 10).
- [JMS96] M Chris Jones, James S Marron, and Simon J Sheather. “A brief survey of bandwidth selection for density estimation”. In: *Journal of the American statistical association* 91.433 (1996), pp. 401–407 (cit. on p. 56).
- [Kay93] Steven M Kay. *Fundamentals of Statistical Signal Processing, Volume I: Estimation Theory*. Englewood Cliffs (NJ): Prentice Hall, 1993 (cit. on pp. 38, 75, 77, 79, 80).
- [Kay98] Steven M Kay. *Fundamentals of Statistical Signal Processing, Volume II: Detection Theory*. Englewood Cliffs (NJ): Prentice Hall, 1998 (cit. on pp. 25, 29, 30, 32–35, 38, 43, 44).

- [Kba+17] Nabil Kbayer et al. “On Lower Bounds for Non-Standard Deterministic Estimation”. In: *IEEE Trans. Signal Process.* 65.6 (2017), pp. 1538–1553 (cit. on p. 77).
- [KDP06] Jason C Kiiskila, Matthew R Duncan, and Dale M Pitt. “Investigation of the Dynamic Characterization of Aircraft Control Surface Free Play”. In: *Proc. of the 24th International Modal Analysis Conference*. Saint Louis, Missouri, 2006 (cit. on p. 26).
- [Kho14] Denis B Kholodar. “Nature of freeplay-induced aeroelastic oscillations”. In: *Journal of Aircraft* 51.2 (2014), pp. 571–583 (cit. on p. 20).
- [Lav+14] Loic Lavigne et al. “New sequential probability ratio test: Validation on A380 flight data”. In: *Control Engineering Practice* 22 (2014), pp. 1–9 (cit. on p. 51).
- [Lev08] Bernard C Levy. *Principles of signal detection and parameter estimation*. Springer Science & Business Media, 2008 (cit. on pp. 30, 51).
- [Lev44] Kenneth Levenberg. “A method for the solution of certain non-linear problems in least squares”. In: *Quarterly of applied mathematics* 2.2 (1944), pp. 164–168 (cit. on p. 64).
- [Liv17] Eli Livne. “Aircraft Active Flutter Suppression State of the Art and Technology Maturation Needs”. In: *Proc. 58th AIAA/ASCE/AHS/ASC Structures, Structural Dynamics, and Materials Conference, AIAA SciTech Forum*. Grapevine, Texas: AIAA, 2017 (cit. on p. 22).
- [Loz08] Félix A Lozano. “Aeroelasticidad de una aeronave en presencia de no linealidades estructurales concentradas”. PhD thesis. Universidad Politécnica de Madrid, 2008 (cit. on p. 15).
- [Lub08] Wolfgang G Luber. “Limit Cycle Oscillation on Control Surfaces Due to Freeplay”. In: *Nato report RTO-MP-AVT-152*. (2008) (cit. on pp. 15, 26).
- [Man95] John C Mankins. “Technology readiness levels”. In: *White Paper, April* (1995). URL: <http://snebulos.mit.edu/projects/reference/NASA-Generic/TechnologyReadinessLevels.pdf> (cit. on p. 105).
- [Mar63] Donald W Marquardt. “An algorithm for least-squares estimation of nonlinear parameters”. In: *Journal of the society for Industrial and Applied Mathematics* 11.2 (1963), pp. 431–441 (cit. on p. 64).
- [MDM17] Andrea Mannarino, Earl H Dowell, and Paolo Mantegazza. “An adaptive controller for nonlinear flutter suppression and free-play compensation”. In: *Journal of Vibration and Control* 23.14 (2017), pp. 2269–2290 (cit. on p. 22).
- [MJ15] Pierre Moulin and Patrick Johnstone. “Strong large deviations for Rao test score and GLRT in exponential families”. In: *Proc. IEEE Int. Symp. Inform. Theory*. Hong-Kong, China, June 2015, pp. 779–783 (cit. on pp. 30, 50).

- [Mor07] Alvaro V Moreno. *Mechanism for eliminating limit cycle oscillations on servocontrolled aerodynamic control surfaces*. US Patent 7,175,132. Feb. 2007 (cit. on p. 22).
- [Mor78] Jorge J Moré. “The Levenberg-Marquardt algorithm: implementation and theory”. In: *Numerical analysis*. Springer, 1978, pp. 105–116 (cit. on p. 64).
- [MS00] John V Mathews and Giovanni L Sicuranza. *Polynomial Signal Processing*. New York: Wiley, 2000 (cit. on p. 57).
- [Mui09] Robb J Muirhead. *Aspects of Multivariate Statistical Theory*. Vol. 197. New-York: John Wiley & Sons, 2009 (cit. on p. 43).
- [Nel01] Oliver Nelles. *Nonlinear System Identification*. New York:Springer-Verlag, 2001 (cit. on p. 57).
- [Nob13] Matthew R Noble. “Nonlinear Aeroelastic Behavior of Tail/Rudder Systems with Freeplay and Actuator Failure”. PhD thesis. University of Washington, 2013 (cit. on p. 20).
- [Ott+93] Bjorn Ottersten et al. “Exact and large sample maximum likelihood techniques for parameter estimation and detection in array processing”. In: *Radar Array Processing, S. Haykin, J. Litva, and T. J. Shepherd, Eds., chapter 4* (1993), pp. 99–151 (cit. on pp. 75, 79, 80).
- [PB14] Dale M Pitt and Prasun Bansal. “Uncertainties in control surface free-play and structural properties and their effect on flutter and LCO”. In: *55th AIAA/ASMe/ASCE/AHS/SC Structures, Structural Dynamics, and Materials Conference (AIAA Scitech Forum)*. National Harbor, Maryland, 2014 (cit. on pp. 14, 20).
- [PHW07] Miroslaw Pawlak, Zygmunt Hasiewicz, and Pawel Wachel. “On Nonparametric Identification of Wiener Systems”. In: *IEEE Trans. Signal Process.* 55.2 (Feb. 2007), pp. 482–492 (cit. on pp. 53, 57–60, 62, 64, 72, 75, 76, 79, 80, 83, 96, 103).
- [PK11] Dale M Pitt and Jason C Kiiskila. *System for and method of monitoring free play of aircraft control surfaces*. US patent 7,933,691. Apr. 2011 (cit. on pp. 22, 26, 104).
- [PSZ96] S. Puntanen, G. P. H. Styan, and F. Zhang. “An equivalence relation for two symmetric idempotent matrices”. In: *Econometric Theory* 12.3 (1996), pp. 590–592 (cit. on p. 110).
- [RB74] David C Rife and Robert R Boorstyn. “Single tone parameter estimation from discrete-time observations”. In: *IEEE Trans. Inf. Theory* 20.5 (1974), pp. 591–598 (cit. on p. 30).
- [Ren+06] Alexandre Renaux et al. “On the high-SNR conditional maximum-likelihood estimator full statistical characterization”. In: *IEEE Trans. Signal Process.* 54.12 (2006), pp. 4840–4843 (cit. on pp. 30, 40, 76, 80, 107).
- [Ric05] Christ D Richmond. “Capon algorithm mean-squared error threshold SNR prediction and probability of resolution”. In: *IEEE Trans. Signal Process.* 53.8 (2005), pp. 2748–2764 (cit. on p. 30).

- [RPD09] Jeffrey S Racine, Christopher F Parmeter, and Pang Du. “Constrained nonparametric kernel regression: Estimation and inference”. In: *Working paper* (2009). URL: <http://www.eco.uc3m.es/temp/Racine.pdf> (cit. on pp. 69, 70).
- [SAS17] Airbus SAS. “Troubleshooting Airframe Vibrations”. In: *Safety First, The Airbus safety magazine* 24 (2017), pp. 26–32 (cit. on p. 1).
- [Sch+18] Christian Schallert et al. “Automated Measurement of Backlash and Stiffness in Electro-Mechanical Flight Control Actuation”. In: *Proc. 8th International Conference on Recent Advances in Aerospace Actuation Systems and Components (R3ASC)*. School of Mechanical Engineering of the Institut National des Sciences Appliquées and the Institut Clément Ader laboratory. Toulouse, France, 2018 (cit. on p. 22).
- [Sch91] Louis L Scharf. *Statistical Signal Processing*. Vol. 98. Addison-Wesley Reading, MA, 1991 (cit. on p. 30).
- [Sed+00] Ahmad Sedaghat et al. “Limit cycle oscillation prediction for aeroelastic systems with continuous non-linearities”. In: *Proc. 41st Structures, Structural Dynamics, and Materials Conference and Exhibit*. Atlanta, Georgia, 2000, p. 1397 (cit. on p. 22).
- [SF94] Louis L Scharf and Benjamin Friedlander. “Matched subspace detectors”. In: *IEEE Trans. Signal Process.* 42.8 (1994), pp. 2146–2157 (cit. on p. 30).
- [Sil18] Bernard W Silverman. *Density estimation for statistics and data analysis*. Routledge, 2018 (cit. on p. 56).
- [Sim11] Pascal Simon. “Détection robuste et précoce des pannes oscillatoires dans les systèmes de commandes de vol”. PhD thesis. Bordeaux 1, 2011 (cit. on p. 25).
- [SKA02] SA Safi, Donald W Kelly, and RD Archer. “Interaction between wear processes and limit cycle oscillations of a control surface with free-play non-linearity”. In: *Proc. of the Institution of Mechanical Engineers, Part G: Journal of Aerospace Engineering* 216.3 (2002), pp. 143–153 (cit. on pp. 20, 87).
- [SN90a] Petre Stoica and Arye Nehorai. “Mode, maximum likelihood and Cramer-Rao bound: Conditional and unconditional results”. In: *Proc. ICASSP-90*. Albuquerque, NM, USA, Apr. 1990, pp. 2715–2718 (cit. on p. 30).
- [SN90b] Petre Stoica and Arye Nehorai. “Performance study of conditional and unconditional direction-of-arrival estimation”. In: *IEEE Trans. Acoust., Speech, Signal Process.* 38.10 (1990), pp. 1783–1795 (cit. on pp. 30, 38, 75, 79, 80).

- [Sut12] Alan N Sutherland. “Aeroservoelastic analysis, design and wind tunnel testing of a three degree-of-freedom binary flutter model”. MA thesis. University of the Witwatersrand, 2012 (cit. on p. 20).
- [TD11] Deman Tang and Earl H Dowell. “Aeroelastic response induced by free play, Part 1: theory”. In: *AIAA journal* 49.11 (2011), pp. 2532–2542 (cit. on p. 20).
- [TLS04] Pascal Traverse, Isabelle Lacaze, and Jean Souyris. “Airbus fly-by-wire: A total approach to dependability”. In: *Building the Information Society*. Springer, 2004, pp. 191–212 (cit. on p. 11).
- [TS88] Jenho Tsao and Bernard D Steinberg. “Reduction of sidelobe and speckle artifacts in microwave imaging: the CLEAN technique”. In: *IEEE Transactions on Antennas and Propagation* 36.4 (1988), pp. 543–556 (cit. on p. 37).
- [TT10] Koby Todros and Joseph Tabrikian. “General Classes of Performance Lower Bounds for Parameter Estimation-Part I: Non-Bayesian Bounds for Unbiased Estimators”. In: *IEEE Trans. Inf. Theory* 56.10 (2010), pp. 5064–5082 (cit. on p. 77).
- [TVD02] Steve T Trickey, Lawrence N Virgin, and Earl H Dowell. “The stability of limit-cycle oscillations in a nonlinear aeroelastic system”. In: *Proc. of the Royal Society of London A: Mathematical, Physical and Engineering Sciences*. Vol. 458. 2025. The Royal Society. 2002, pp. 2203–2226 (cit. on p. 20).
- [Urb+17a] Simone Urbano et al. “A Data-Driven Approach For Actuator Servo Loop Failure Detection”. In: *Proc. 20th IFAC World Congress, IFAC-PapersOnLine*. Vol. 50. 1. Toulouse, France: Elsevier, 2017, pp. 13544–13549 (cit. on p. 25).
- [Urb+17b] Simone Urbano et al. *Procédé et dispositif de détection et de diagnostic de vibrations d’un aéronef liées à un phénomène d’usure de pièces mécaniques dans une gouverne*. Application No 1761214, submitted to the French Patent Office (INPI). 2017 (cit. on p. 2).
- [Urb+18a] Simone Urbano et al. “Aircraft Vibration Detection and Diagnosis for Predictive Maintenance using a GLR Test”. In: *Proc. IFAC Symp. on fault Detection, Supervision and Safety for Technical Processes (IFAC Safeprocess)*. Warsaw, Poland, Aug. 2018 (cit. on pp. 2, 87).
- [Urb+18b] Simone Urbano et al. “On the High-SNR Receiver Operating Characteristic of the GLRT for the Conditional Signal Model”. In: *Proc. IEEE Int. Conf. Acoust., Speech, and Signal Processing (ICASSP)*. Calgary, Canada, Apr. 2018 (cit. on pp. 2, 29).
- [Urb+19] Simone Urbano et al. “On nonparametric identification of Wiener system with deterministic inputs”. In: *Proc. IEEE Int. Conf. Acoust., Speech, and Signal Processing (ICASSP)*. Brighton, UK, May 2019 (cit. on pp. 2, 74).
- [Van68] Harry L VanTrees. *Detection, Estimation, and Modulation Theory, Part I: Detection, Estimation, and Linear Modulation Theory*. New-York: Wiley, 1968 (cit. on p. 30).

- [VAO17] Rômulo V Vera, Alexandre Alves, and Decio Oliveira. *Testing apparatus, systems and methods for statically determining free play of aircraft control surfaces*. US Patent 9,568,383. Feb. 2017 (cit. on p. 22).
- [Vas+14] Rui MG Vasconcellos et al. “Characterization of grazing bifurcation in airfoils with control surface freeplay nonlinearity”. In: *Proc. 9th International Conference on Structural Dynamics, EUROODYN*. Porto, Portugal, 2014 (cit. on p. 20).
- [VB07] Harry L VanTrees and Kristine L Bell. *Bayesian bounds for parameter estimation and nonlinear filtering/tracking*. New-York: Wiley, 2007 (cit. on pp. 30, 31).
- [Ven+16] Jagadish Venkatramani et al. “Precursors to flutter instability by an intermittency route: a model free approach”. In: *Journal of Fluids and Structures* 61 (2016), pp. 376–391 (cit. on p. 22).
- [Vis96] Augusto Visintin. “Mathematical models of hysteresis”. In: *Modelling and Optimization of Distributed Parameter Systems Applications to Engineering*. Springer, 1996, pp. 71–80 (cit. on p. 65).
- [VK23] Albert G Von Baumhauer and C Koning. “On the stability of oscillations of an airplane wing”. In: *National Advisory Committee for Aeronautics (NACA), Technical Memorandum n.223* (1923) (cit. on p. 21).
- [Wik19a] Wikipedia contributors. *Kernel density estimation — Wikipedia, The Free Encyclopedia*. [https://en.wikipedia.org/w/index.php?title=Kernel\\_density\\_estimation&oldid=893040613](https://en.wikipedia.org/w/index.php?title=Kernel_density_estimation&oldid=893040613). 2019 (cit. on p. 54).
- [Wik19b] Wikipedia contributors. *Kernel regression — Wikipedia, The Free Encyclopedia*. [https://en.wikipedia.org/w/index.php?title=Kernel\\_regression&oldid=886351895](https://en.wikipedia.org/w/index.php?title=Kernel_regression&oldid=886351895). 2019 (cit. on p. 54).
- [Wil38] Samuel S Wilks. “The large-sample distribution of the likelihood ratio for testing composite hypotheses”. In: *The Annals of Mathematical Statistics* 9.1 (1938), pp. 60–62 (cit. on pp. 30, 50).
- [WJ94] Matt P Wand and M Chris Jones. *Kernel smoothing*. Crc Press, 1994 (cit. on pp. 54, 56, 58, 64, 75, 76).
- [Wri+03] Jan R Wright et al. “On the use of control surface excitation in flutter testing”. In: *Proc. of the Institution of Mechanical Engineers, Part G: Journal of Aerospace Engineering* 217.6 (2003), pp. 317–332 (cit. on pp. 17, 18).
- [Zol+13] Ali Zolghadri et al. *Fault diagnosis and fault-tolerant control and guidance for aerospace vehicles: from theory to application*. Springer Science & Business Media, 2013 (cit. on p. 25).

- [Zol17] Ali Zolghadri. “Modern Control Theory and Real-World Aerospace Applications: I love You, Nor do I?” In: *Proc. 20th IFAC World Congress, IFAC-PapersOnLine*. Vol. 50. 1. Toulouse, France: Elsevier, 2017, pp. 6446–6451 (cit. on p. [105](#)).
- [ZW88] Ilan Ziskind and Mati Wax. “Maximum likelihood localization of multiple sources by alternating projection”. In: *IEEE Trans. Acoust., Speech, Signal Process.* 36.10 (1988), pp. 1553–1560 (cit. on pp. [48](#), [110](#), [111](#)).
- [ZZM92] Ofe Zeitouni, Jacob Ziv, and Neri Merhav. “When is the generalized likelihood ratio test optimal?” In: *IEEE Trans. Inf. Theory* 38.5 (1992), pp. 1597–1602 (cit. on p. [30](#)).

“We are not going in circles, we are going upwards. The path is a spiral;  
we have already climbed many steps. ”

—Herman Hesse, *Siddhartha*.